



UNIVERSITY OF TWENTE.

Faculty of Mechanical Engineering,
Department of Thermal and Fluid Engineering,
Engineering Fluid Dynamics research group

Wind tunnel measurements of a small scale wind turbine

I. Dickhof
S2298112
M.Sc. Thesis
9 February 2023

Chair:

prof. dr. ir. C.H. Venner

Supervisor:

dr. ir. A. Van Garrel

Internal member:

dr. ir. W.J.B. Grouve

Internal member:

dipl.-ing. L.A. Castelucci MSC

Report number:

419

Department of Engineering Fluid Dynamics
Faculty of Mechanical Engineering,
University of Twente
P.O. Box 217
7500 AE Enschede
The Netherlands

Preface

Here lies the master thesis: "Wind tunnel measurements of a small scale wind turbine." This thesis is presented as the final requirement for the master's degree in Mechanical Engineering at the University of Twente. This work expands the work of the twin brothers R.F.O. van Wijk and C.F.C. van Wijk who developed the Twente Instrumented Nacelle Turbine (TwIN Turbine) within their graduation period. I extend my gratitude to the brothers for their foundation for my project.

During my graduation period, I broadened my knowledge in data acquisition, electrical engineering, and aeroacoustics, which were elements outside my comfort zone. I also gained a deeper understanding of fluid mechanics. Despite the numerous challenges encountered in my project, I have learned many valuable lessons from these experiences.

I like to thank my supervisor, dr.ir. A. van Garrel, for guiding this project as well as ing. W. Lette for his support in the development of the wind turbine. I also would like to thank ir. L.A. Castelucci and dr.ir. M.P.J Sanders for their valuable insight given within this project. I would like to thank E.M.P Leising MSc, S. Wanrooij, M.H.G. Wilens, dr.ir. Y.H. Wijnant for their supporting roles within my assignment. Also, I like to thank S.K. Janse-Godschalk and B.A. Benders for their administrative role within my project.

Finally, I thank my friends, family, and roommates for being there for me and proofreading my thesis. I also thank you, reader, for reading my thesis.

Iljar Dickhof

Summary

In two previous master projects, a small-scale wind turbine was designed and manufactured for the practical demonstration in the master course "Wind Energy" at the University of Twente. This study aims to address the bottlenecks identified in the earlier works and evaluate the turbine's performance, based on the measurement of torque, rotational speed, and axial rotor force, under a range of wind speeds and blade pitch angles. The experiments were conducted in two semi-open jet wind tunnel test sections, with one configuration featuring a floor and ceiling and the other featuring only a floor.

The primary modifications to the small-scale wind turbine included the replacement of the current electronic load with a programmable Rigol DL3021 electronic load and the integration of a LabVIEW program to capture and process the data from the turbine and the electronic load. The turbine's aerodynamic performance is predicted using the blade element momentum method in the open-source numerical program QBlade. The performance was predicted for pitch angles ranging from -10 to 10 degrees and tip speed ratios ranging from 1 to 8.

The experimental results revealed that a ceiling in the wind tunnel test section resulted in a 15% increase in mechanical power and axial rotor force due to the partial obstruction of the wind turbine's wake. The impact of wind velocities 7.5, 8.5, and 9.5 m/s on the wind turbine's performance were evaluated. The results obtained at a wind speed of 7.5 m/s deviated from the trends obtained at a wind speed of 8.5 and 9.5 m/s which may be attributed to low Reynolds number airfoil degradation. The impact of pitch angle on the turbine's performance was evaluated, revealing a 5-degree pitch phase shift difference between the experimental results and the QBlade prediction. The phase shift difference resulted from a manufacturing error during the design phase of the wind turbine.

To further improve the design of the small-scale wind turbine, several modifications are recommended, including the replacement of the gear transmission with a planetary gearbox for better alignment, the replacement of the current data acquisition system with a plug-and-play system from National Instruments, and the replacement of the torque measurement instrument with a rotary torque sensor. Finally, future aerodynamic analysis should be conducted with the lifting line method within QBlade to predict the aerodynamic performance of the turbine more accurately.

Contents

Preface	iii
Summary	v
Abbreviations	xiii
1 Introduction	1
1.1 Problem	1
1.2 Research questions	2
1.3 Thesis structure	3
2 Aerodynamic concepts relevant to a wind turbine	5
2.1 Airfoil nomenclature	5
2.2 Literature fluid dynamics	6
2.2.1 Reynolds number	6
2.2.2 Boundary layer	6
2.2.3 Laminar and turbulent flow	7
2.2.4 Flow separation	7
2.3 Aerodynamic forces	8
2.4 Blade element momentum theory	8
2.5 Aeroacoustics wind turbine	9
2.6 Blockage effect of wind turbine wake	10
3 Experimental equipment	11
3.1 Wind tunnel	11
3.1.1 Properties wind tunnel	11
3.1.2 Pitot tube and temperature sensor	11
3.2 Design of TwIN-turbine	12
3.2.1 Aerodynamic design	12
3.2.2 Mechanical design	13
3.2.3 Electrical design	14
3.2.4 Points of improvements of TwIN turbine	16
3.3 Acoustic microphone array	16
4 Design modifications	19
4.1 Mechanical design	19
4.1.1 Brake linings	19
4.1.2 Rotor hub modification	20
4.2 Electrical design	20
4.2.1 DC electronic load	20
4.2.2 Modification Arduino perfboard	21
4.2.3 Modification Arduino code	22
4.2.4 LabVIEW program	22
4.2.5 Modification of the electronic circuit	22
5 Aerodynamic analysis	25
5.1 QBlade software	25
5.2 Previous aerodynamic research	25
5.3 Aerodynamic analysis	25
5.3.1 Airfoil characteristics	26
5.3.2 Extrapolation of experimental data	27

5.3.3	Corrections in Qblade	27
5.3.4	Settings Qblade	28
5.3.5	Varying TSR	29
5.3.6	Varying pitch angle	29
6	Preliminary testing	31
6.1	RPM calibration	31
6.2	Torque sensor calibration	32
6.3	Thrust sensor calibration	33
6.4	Generator testing	34
6.5	Noise inspector testing	36
7	Experimental work	37
7.1	Experimental setup	37
7.2	Initial findings	38
7.3	Statistical analysis	38
7.4	Results experiments	39
7.4.1	Influence of ceiling on performance	39
7.4.2	Influence of wind speed on performance	39
7.4.3	Influence of pitch angle on performance	40
7.4.4	Results smoke machine	43
7.4.5	Results microphone array	44
8	Conclusions and recommendations	47
8.1	Conclusions	47
8.2	Recommendations	48
	References	51
	Appendices	
A	Blade Element Momentum theory	55
A.1	Betz limit and one-dimensional momentum	55
A.2	Momentum theory with wake rotation	57
A.3	Blade element theory	58
A.4	Corrections in blade element momentum theory	59
B	Datasheets	61
B.1	Datasheet Brushless motor	61
B.2	Datasheet Rectifier	62
C	Arduino code	63
D	LabVIEW program	67
D.1	Interface LabVIEW program	67
D.2	LabVIEW program	68
E	SD7037 Airfoil Characteristics	73
F	Robust blade element prediction	75
F.1	Rotor Blade Design	75
F.2	Excel BEM method	76
G	Influence QBlade corrections on performance	77
H	Statistical analysis	79
H.1	Settling time	79
H.2	Measurement time	80
H.3	Error Analysis	80
I	Histograms sensor data	83
I.1	Histograms torque load cell	83
I.2	Histograms thrust load cell	84
I.3	Histograms magnetic encoder	85

J Design mistakes

87

Nomenclature

Symbol	Description	Units
α	Angle of attack	[°]
δ	Boundary layer thickness	[m]
ΔV	Voltage drop over diode	[V]
\dot{m}	Mass flow	[kg/s]
ϵ	Convergence criteria	[-]
λ	Tip speed ratio	[-]
λ_r	Local tip speed ratio	[-]
μ	Dynamic viscosity	[Ns/m ²]
ν	Kinematic viscosity	[m ² /s]
Ω	Rotational velocity of rotor	[s ⁻¹]
ω	Rotational velocity of air behind rotor	[s ⁻¹]
Φ	Local inflow angle	[°]
ρ	Air density	[kg/m ³]
θ	Blade pitch angle	[°]
θ_p	Local pitch angle or twist angle	[°]
a	Axial induction factor	[-]
a'	Tangential induction factor	[-]
A_R	Area of rotor	[m ²]
B	Number of blades	[-]
c	Chord	[m]
C_d	Drag coefficient	[-]
C_l	Lift coefficient	[-]
C_m	Pitching moment coefficient	[-]
C_P	Power coefficient	[-]
C_Q	Torque coefficient	[-]
C_T	Thrust coefficient	[-]
D	Drag force	[N]
dF_N	Incremental normal force	[N]
dF_T	Incremental tangential force	[N]

dQ	Incremental torque	$[Nm]$
f	Frequency	$[Hz]$
I_L	Current over load	$[RPM/V]$
k_{gen}	Generator constant	$[RPM/V]$
L	Lift force	$[N]$
l	Characteristic length	$[m]$
L_{sub}	Sound pressure	$[dB]$
M	Pitching moment	$[Nm]$
n_{gen}	Generator's rotational velocity	$[RPM]$
P	Power	$[W]$
Q	Torque	$[N]$
R	Radius rotor	$[m]$
r	Radial distance along rotor	$[m]$
R_{gen}	Internal resistance generator	$[\Omega]$
Re	Reynolds number	$[-]$
T	Thrust	$[N]$
U	Free stream velocity	$[m/s]$
$U_{DC,r}$	Rectified DC voltage	$[V]$
U_{rel}	Wind velocity relative to blade	$[m/s]$
v	Characteristic fluid velocity	$[m/s]$
x	Trip location	$[m]$

Abbreviations

TWIN	Twente Instrumented Nacelle
TSR	Tip Speed Ratio
MEMS	Micro Electro-Mechanical System
TDMS	Technical Data Management Streaming
DFT	Discrete Fourier Transform
FFT	Fast Fourier Transform
DC	Direct Current
AC	Alternating Current
LCD	Liquid-Crystal Display
IDE	Integrated Development Environment
USB	Universal Serial Bus
VI	Virtual Instrument
BEM	Blade Element Momentum
RANS	Reynolds-Averaged Navier-Stokes
BLDC	Brushless Direct Current
DAQ	Data Acquisition
s/b	Structural Borne
a/b	Air Borne

Introduction

1.1 Problem

Within the University of Twente, a small-scale wind turbine called the Twente Instrumented Nacelle wind turbine (TwIN) turbine was developed (Figure 1.1). The development of the initial design of the turbine and the first performance test is documented in two master thesis reports from C.F.C van Wijk [1] and R.F.O. van Wijk [2]. The main purpose of the small-scale wind turbine is to serve as a practical learning tool for the Wind Energy course. During the testing phase of the TwIN turbine, various issues were identified. The first problem was the presence of an upper and lower table during performance measurements that partially blocked the expansion of the wake stream of the wind turbine. The blockage of the wake of the stream resulted in an increase in the local air velocity at the rotor compared to an unblocked test section. It was recommended to investigate the effect of the upper and lower table on the performance of the TwIN turbine. Additionally, due to a lack of time, the effect of the blade's pitch angle on the aerodynamic performance of the TwIN turbine was not examined. It was recommended to further investigate the pitch angle's influence on the TwIN turbine's performance.



Figure 1.1: The TwIN turbine

Several malfunctions were encountered during the experimental phase of the TwIN turbine. One severe problem was the overheating of the electrical resistance for certain conditions resulting in a fire hazard. It was recommended to redesign the wind turbine's electrical system to reduce the chance of a fire hazard and improve safety. Furthermore, it was proposed to redesign certain parts of the wind turbine's mechanical system to fix the mechanical malfunctions.

The experiments were compared to numerical simulations in the open-source software QBlade. Within the report of Cedric [1], only a limited number of conditions were studied. It was suggested that future aerodynamic analysis would benefit from including additional conditions.

Various tests were previously conducted on the TwIN turbine as part of an Academic Research Skills course for premaster students. In the report from J. Olde et al. [3], the aeroacoustic effect of blades

featuring trailing edge serrations and flexible trailing edge serrations was compared to the baseline blades. It was discovered that the fixed trailing edge configuration produced a noise of 1 dB lower than the baseline blades. However, it was impossible to compare the flexible trailing edge configuration with the other two configurations due to the extra drag created by the flexible trailing edge. The extra drag eventually reduced the rotational speed, making comparison impossible. It was noted that there were other noise sources present during the aeroacoustic analysis. These additional sources interfered with the aeroacoustic investigation of the rotor. It was recommended to locate the noise sources of the TwIN turbine.

1.2 Research questions

The main question formulated within this thesis is as follows: *What is the performance and noise production of the TwIN turbine under a range of blade pitch angles and wind speeds?*

The main question is divided into the following sub-questions:

1. *What design modifications can be implemented to improve the design of the small-scale wind turbine?*
2. *What is the theoretical aerodynamic performance of the TwIN turbine under various wind tunnel speeds, blade pitch angles, and tip speed ratios?*
3. *What is the impact of the blade's pitch angle on the performance of the TwIN turbine at a range of wind speeds and rotational velocities?*
4. *What is the impact of the ceiling within the test section on the aerodynamic performance of the TwIN turbine?*
5. *What are the primary noise sources of the TwIN turbine?*

The first question is answered by identifying the initial development's bottlenecks and taking appropriate measures to address them. The most significant bottleneck was a series of malfunctions with the electronic load. To assess this issue, it was recommended that the programmable external load available at the University of Twente is utilized. Furthermore, students at the University of Twente have access to a LabVIEW license, which allows for the development of a LabVIEW program to communicate with the measurement instruments.

Question two is answered by performing an aerodynamic analysis with the blade element momentum theory within the open-source software QBlade. The aerodynamic prediction serves as validation for the experimental results.

Question three is answered by comparing the performance of the TwIN turbine with several pitch angles. The best performance is expected at a pitch angle of 0 degrees and the design conditions for the rotor blade.

Question four is answered by comparing the performance of the TwIN turbine installed in two separate test sections, one with a floor and a ceiling and the other with just a floor and no ceiling. It is expected that the turbine located in the test section with a ceiling has higher performance than the one in the test section without a ceiling. This is due to the fact that the ceiling partially blocks the flow of the wake, leading to an increase in the wind velocity that is induced at the rotor.

Question five is answered by capturing the pressure fluctuations with a microphone array along a measurement time. The noise sources can be studied with the available microphone array at the University of Twente in combination with the beam-forming algorithm. It is expected that the gears produce the most sound within the system.

1.3 Thesis structure

This thesis is structured as follows:

Chapter 2: Aerodynamic concepts

This chapter describes the aerodynamic concepts relevant to the small-scale wind turbine. Concepts like the boundary layer, separation flow, and the Reynolds number are explained, as well as the blade element momentum theory and the aeroacoustics of a wind turbine.

Chapter 3: Experimental equipment

This chapter describes the experimental equipment for the experimental phase of this thesis, including the wind tunnel, the TwIN turbine, and the acoustic microphone array.

Chapter 4: Design modifications

This chapter covers the mechanical and electrical modifications made to the wind turbine.

Chapter 5: Aerodynamic analysis

This chapter discusses the aerodynamic analysis conducted on the TwIN turbine.

Chapter 6: Preliminary testing

This chapter details the testing performed outside the wind tunnel, including the calibration of the TwIN turbine and the testing of the microphone array.

Chapter 7: Experimental work

This chapter covers the experimental work conducted inside the wind tunnel. Performance measurements of the TwIN turbine and aeroacoustic measurements are conducted.

Chapter 8: Conclusion and recommendations

The final chapter includes a discussion, conclusion, and recommendations for future experimental analysis.

Aerodynamic concepts relevant to a wind turbine

2.1 Airfoil nomenclature

This section describes the various dimensions important for the geometry of an airfoil. Figure 2.1 shows a 2D geometry of an airfoil. The line going through the middle represents the mean camber line. The line goes from the leading edge to the trailing edge of the airfoil. The chord (c) is defined as the distance between the trailing edge and the leading edge. The airfoil thickness is defined as the distance between the upper and lower surface. Lastly, the angle of attack (α) is defined as the angle between the chord line and the wind speed (U_{rel}).

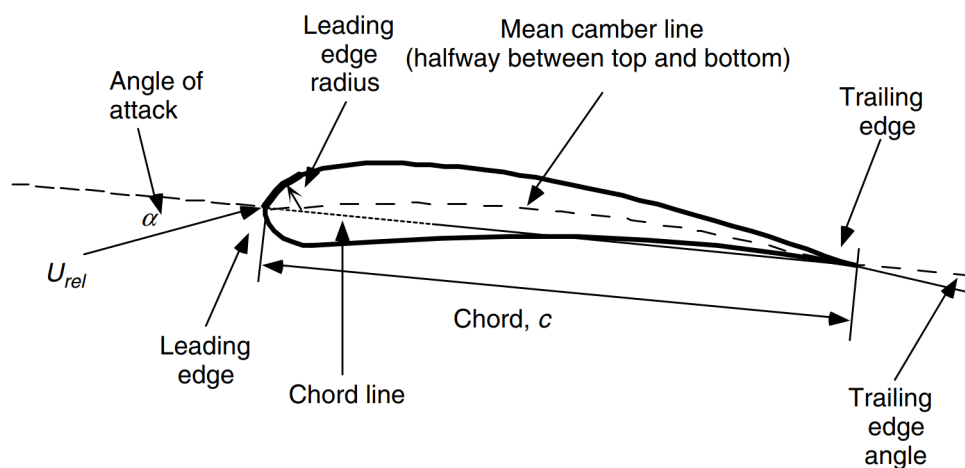


Figure 2.1: Airfoil nomenclature [4]

The length perpendicular to the cross-section of the airfoil is defined as the span. This span together with the earlier mentioned geometrical dimensions is responsible for the aerodynamic performance of a blade [4].

2.2 Literature fluid dynamics

This section describes the aerodynamic literature relevant to wind turbines. Concepts like the Reynolds number, the boundary layer, turbulent and laminar flow, and separation flow are explained in this section.

2.2.1 Reynolds number

The Reynolds number is the ratio between the inertial forces and the viscous forces within a fluid in motion. The number is vital for the behavior of fluids. Equation 2.1 shows the expression for the Reynolds number.

$$Re = \frac{\rho v l}{\mu} = \frac{v l}{\nu} \quad (2.1)$$

In which:

v = The characteristic velocity of the fluid. For an airfoil, this is the relative velocity of the fluid alongside the airfoil ($v = U_{rel}$)

l = The characteristic length. For an airfoil, this is the chord length of the airfoil ($l = c$)

ρ = The density of the fluid

μ = The dynamic viscosity of the fluid

ν = The kinematic viscosity of the fluid

The Reynolds number can be used for predicting flow patterns. This dimensionless number influences where the transition from laminar to turbulent flow occurs. Additionally, the number is used to scale similar but different-sized flow applications.

2.2.2 Boundary layer

The boundary layer represents a thin layer of fluid that flows along a surface, created by the interaction of the surface and the fluid. The layer has zero velocity at the surface and increases above the surface until the outer stream velocity is reached. The boundary layer's edge is reached when the flow particles reach a velocity of 99% of the external stream velocity. The boundary layer thickness is defined as the thickness between the surface and the boundary layer edge. Figure 2.2 shows how a boundary layer develops along a flat surface. A boundary layer along an airfoil is responsible for the characteristic lift, drag, and aerodynamic noise.

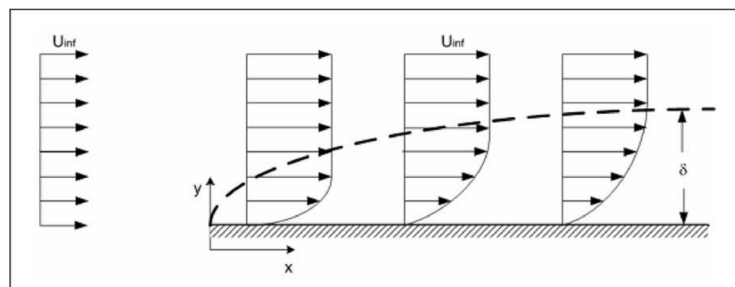


Figure 2.2: The boundary layer over a flat surface [5]

2.2.3 Laminar and turbulent flow

Two different flow regimes are present when analyzing the boundary layer. One regime is the laminar flow which is characterized as smooth and streamlined. The other regime is turbulent flow characterized as irregular and chaotic. One can look at the Reynolds number to determine if the flow is in the laminar or turbulent regime on a flat plate. This number increases as the flow moves along the surface. The flow starts as a laminar flow and transitions into turbulent flow as the Reynolds number reaches a certain number. This phenomenon is schematically displayed in figure 2.3 for flat plates.

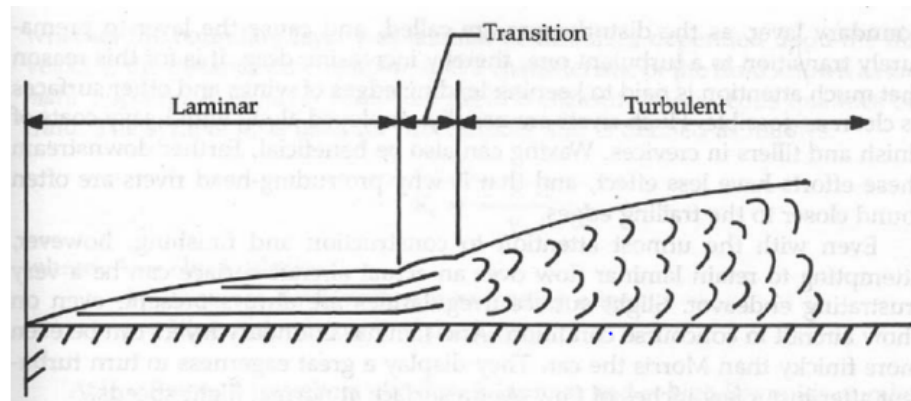


Figure 2.3: Transition over a flat surface [5]

2.2.4 Flow separation

Flow separation refers to the detachment of the boundary layer from a surface. Figure 2.4 shows the characteristics of laminar flow separation for different Reynolds regimes for an airfoil with a moderate angle of attack. Figure 2.4c illustrates the separation behavior for high Reynolds numbers. The boundary layer detaches and re-attaches close to the leading edge resulting in a separation bubble. Figure 2.4b shows the separation behavior for lower Reynolds numbers. The separation starts later on the surface and re-attaches close to the trailing edge, resulting in a big separation bubble. This Reynolds regime is characterized by unstable behavior and hysteresis effects. Figure 2.4a shows the separation behavior for even lower Reynolds numbers. The boundary layer separates not far from the trailing edge and does not reattach. Flow separation on an airfoil results in a high-pressure drag, a reduction in lift, and highly unsteady behavior.

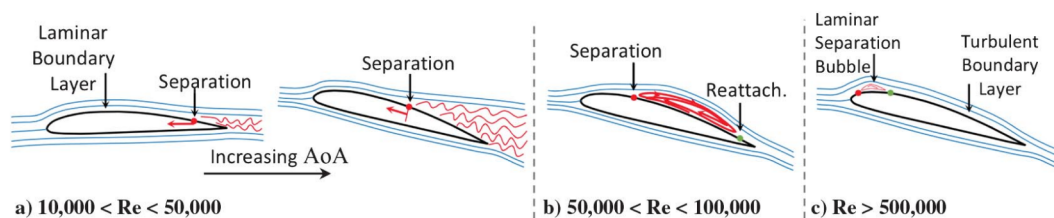


Figure 2.4: Laminar flow separation characteristics for different Reynolds numbers [6]

Turbulent flow separation occurs when the low velocity fluid elements inside the turbulent boundary layer have too little momentum to overcome the adverse pressure gradient. Turbulent flow separation normally starts near the trailing edge and moves forward with increasing angle of attack. It should be noted that a combination of both laminar and turbulent flow separation is possible.

2.3 Aerodynamic forces

An airflow over an airfoil produces forces on that surface. The forces are defined as the lift, drag, and pitch moment. Figure 2.5 illustrates these forces. The lift force (L) is perpendicular to the airflow and results from the pressure difference between the upper and lower surface. The drag force (D) is defined as the force parallel to the airflow and is a result of the same pressure difference and viscous friction forces. The pitching moment (M) is defined as the moment over the aerodynamic center of the airfoil. The location of the aerodynamic center is located at $c/4$ from the leading edge. The lift and drag force are considered to act at the aerodynamic center.

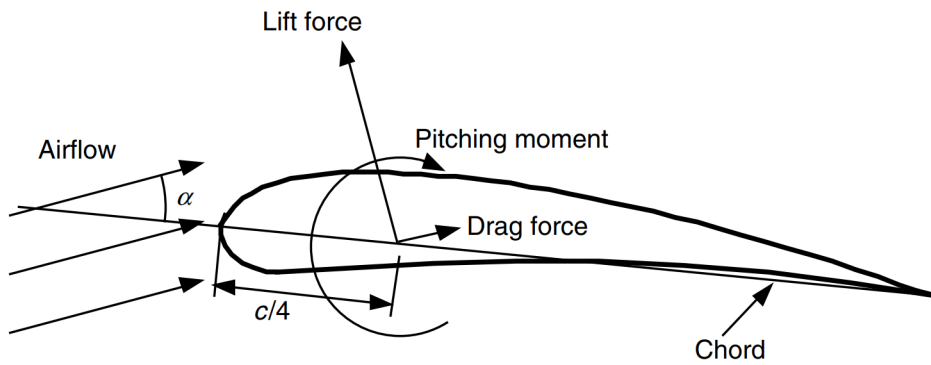


Figure 2.5: Forces on airfoil [4]

Flow problems are usually characterized by non-dimensional parameters. The main advantage of non-dimensional units is the ability to scale similar but different-sized flow applications. Here the lift, drag, and pitching moment are expressed as the lift coefficient (C_l), the drag coefficient (C_d), and the pitching moment coefficient (C_m). The coefficients are defined as follows [4]:

$$C_l = \frac{L/l_s}{\frac{1}{2}\rho U^2 c}; \quad C_d = \frac{D/l_s}{\frac{1}{2}\rho U^2 c}; \quad C_m = \frac{M/l_s}{\frac{1}{2}\rho U^2 c^2} \quad (2.2)$$

Here, l_s is the airfoil span, c is the chord, U is the free stream velocity, A is the airfoil area (chord x span), and ρ is the density of the air.

2.4 Blade element momentum theory

The behavior of wind turbines or propellers can be determined with the blade element momentum theory, which combines both the momentum theory and the blade element theory. The one-dimensional momentum analysis is presented in Appendix A.1 and again with the inclusion of wake rotation in Appendix A.2. The blade element theory is explained in appendix A.3. The aerodynamic performance is established by the combination of both described theorems. This is achieved through the numerical calculation of both the axial induction factor a and the tangential induction factor a' present in both theorems. With the induction factors, the axial velocity vector and rotational velocity at the blades is established. The velocity components are required to determine the lift and drag at each blade segment along the rotor. The resulting force from the airfoil is decomposed into an axial force [N] and an in-plane force [N]. The latter gives, multiplied with the radial position r and integrated over all blade lengths, the rotor's aerodynamic torque [Nm]. The mechanical power (P) is obtained by multiplying

the torque with the rotational speed of the rotor. The torque, thrust, and mechanical power are made non-dimensional with the following expressions [4]:

$$C_T = \frac{T}{\frac{1}{2}\rho U^2 A_R}; \quad C_Q = \frac{Q}{\frac{1}{2}\rho U^2 R A_R}; \quad C_P = \frac{P}{\frac{1}{2}\rho U^3 A_R} \quad (2.3)$$

These quantities can be expressed as a function of the tip speed ratio (λ). The tip speed ratio is the ratio between the rotational velocity of the blade's tip and the wind speed. This quantity is defined as follows:

$$\lambda = \frac{\Omega R}{U} \quad (2.4)$$

2.5 Aeroacoustics wind turbine

A wind turbine has several sound sources that contribute to the total noise production. Figure 2.6 shows the total sound pressure of all sound sources within a wind turbine; s/b indicates structural borne, and a/b indicates airborne. This figure shows that the blade aerodynamics contributes to the most noise production. Experimental research on a real-life wind turbine was already performed by Oerlemans [7]. A microphone array aimed at the wind turbine was used in that research. The pressure fluctuations captured by the microphones were post-processed with a beam-forming algorithm to create an aeroacoustic image averaged over several revolutions (figure 2.7). This figure shows that the blades produced the most noise, which corresponds with figure 2.6. It was concluded that this was due to the trailing edge noise of the blades, classified as air-foil-self-noise. The air-foil-self-noise is categorized into two groups: the Laminar-boundary-layer/vortex-shedding noise and the turbulent-boundary-layer/trailing edge noise. According to Oerlemans, vortex-shedding is primarily present for low-Reynolds number applications such as a small-scale wind turbine [8]. Another thing that stands out in figure 2.7 is the asymmetric noise production of the blades. Most noises were generated during the downward motion of the blades. Oerlemans [7] claimed this was because of convective amplification and directivity.

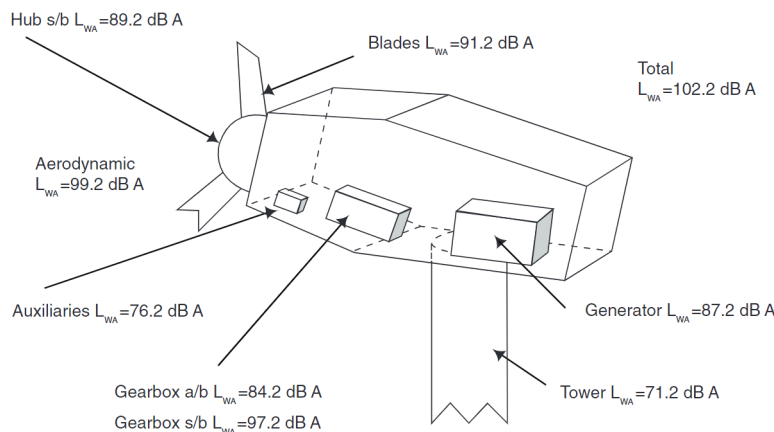


Figure 2.6: Total sound pressure of components [9]

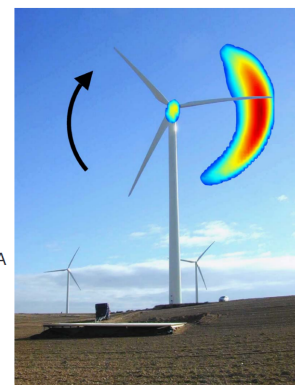


Figure 2.7: Experimental noise characterisation wind turbine [7]

2.6 Blockage effect of wind turbine wake

The open test section within the university of Twente consists of a ceiling and floor that may affect the expansion of the wake of the wind turbine. The natural expansion of the flow may be partially hindered by the presence of a ceiling and floor in the test section. Figure 2.8 demonstrates how the incoming velocity must be modified in a blocked test section to achieve equivalent wind turbine performance as in an unblocked test section. The light blue arrows demonstrate the velocity vectors for an unobstructed flow expansion, while the dark blue arrows demonstrate the velocity vectors for an obstructed flow expansion. The red dotted line represents the expansion velocity profile for an unobstructed test section, while the dark blue line shows the expansion velocity profile for an obstructed test section. The purple arrow shows the amount of thrust generated by the turbine, which is the same if the velocity in the blocked test section is corrected. It should be noted that the figure is a comparison between a fully blocked test section (walls on every side of the wind turbine) and a fully unblocked test section. The research conducted by Ryi et al. [10] has determined that a correction factor can be applied to the incoming velocity if the turbine is tested in a fully blocked test section. However, the open test section within the university of Twente has a floor and a ceiling but is open at the sides. Experimental research is required to understand the difference in the wind turbine's performance for the presence and absence of a ceiling in the test section.

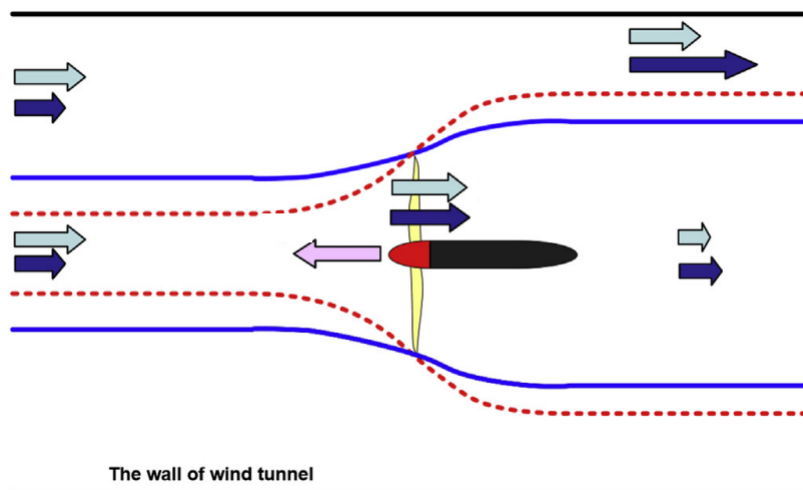


Figure 2.8: Blockage effect [10]

Experimental equipment

3.1 Wind tunnel

At the University of Twente, an aeroacoustic wind tunnel is available for aerodynamic and aeroacoustic experiments. This section explains the operating principle of the wind tunnel with its available equipment.

3.1.1 Properties wind tunnel

Figure 3.1 demonstrates a schematic view of the wind tunnel. The motion of the wind is created with a centrifugal fan driven by a 32 kW motor with a maximum rotational speed of 3000 RPM (1). A water-cooled heat exchanger maintains a constant air temperature (2). The air is then guided through an acoustic baffle section (3) to minimize the noise generated by the aerodynamic interaction of the flow and the heat exchanger. The airflow is directed through a settling chamber (5) where a honeycomb structure and various screens are used to create a more streamlined flow. The honeycomb structure, made up of a series of tubes placed in the lengthwise direction of the airflow, eliminates swirling winds within the flow. The screens eliminate high and low velocities within the flow, creating an equal velocity distribution. The resulting pressure drop from the airflow passing through the screens creates a constant air velocity within the wind tunnel. The flow is then directed through a contraction cone (7) designed to create a high velocity without introducing extra turbulence. The flow is then directed through the test section (8), located in the anechoic chamber (9). The test section consists of a table that test setups can be clamped to, and it can be rotated 360 degrees to create a variation in orientation with respect to the incoming air. The walls of the anechoic chamber are covered with sound-absorbing triangles and perforated blocks to avoid sound reflection during aeroacoustic measurements. After passing through the collector, the flow goes through the channel (10) again, creating a closed circuit. The wind within the wind tunnel has the capability to reach velocities up to 240 *km/h* [11].

3.1.2 Pitot tube and temperature sensor

The velocity of the wind is measured with the use of a pitot tube. Figure 3.2 demonstrates a schematic view of the pitot tube. This device measures the incoming wind's static and stagnation pressure. The static pressure is measured by pressure taps perpendicular to the flow velocity. The stagnation pressure is measured by the pressure tap directly at the stagnation point of the tube. The flow velocity is then determined using the Bernoulli equation. The temperature of the wind within the

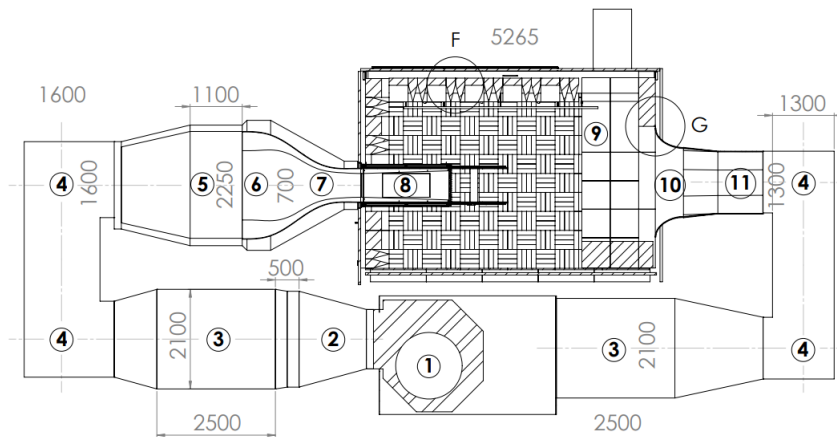


Figure 3.1: Utwente Aeroacoustic wind tunnel [11]

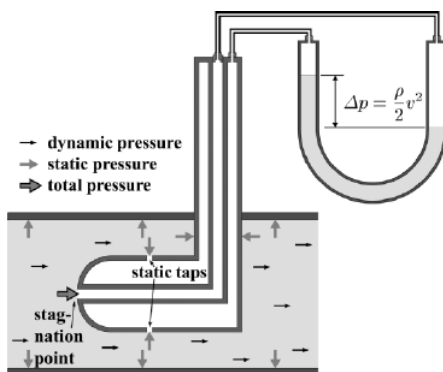


Figure 3.2: Pitot tube [12]

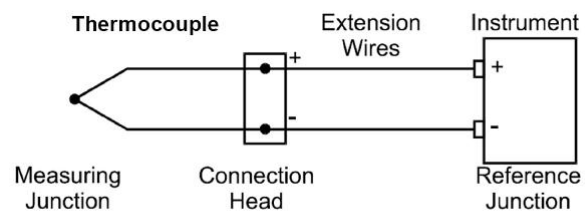


Figure 3.3: Thermocouple [13]

wind tunnel is measured with the use of a thermocouple. Figure 3.3 illustrates a schematic view of the thermocouple. It consists of two materials that are electrically connected to the measuring junction. When heat is applied to the junction, a voltage is created between the two wires called the electromotive force (or E.M.F.). This voltage is then related to the temperature.

3.2 Design of TwIN-turbine

This section discusses the TwIN-turbine from an aerodynamic, mechanical and electrical viewpoint.

3.2.1 Aerodynamic design

The aerodynamic design of the wind turbine is restricted to the turbine's rotor. The rotor includes a hub with three attached blades (figure 3.4). The blades are subdivided into thirteen elements for the aerodynamic analysis, each with the SD7037 airfoil geometry as a cross-section (figure 3.5). This airfoil is chosen as geometry because it has overall good performance for low Reynolds numbers (e.g. 50.000) for various angles of attack, which are the operation conditions of the TwIN turbine. Using the Blade Element Momentum theory, the optimal cord and twist for each section were determined. The optimization of the blade is described in detail in the MSc thesis of C.F.C. van Wijk [1].

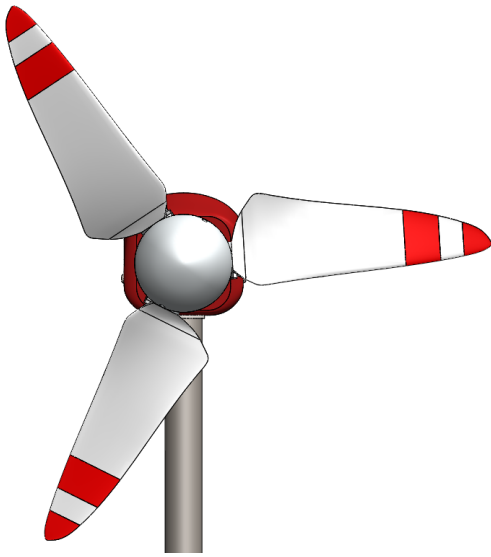


Figure 3.4: Hub with blades

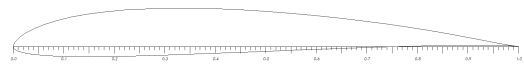


Figure 3.5: SD7037 airfoil geometry

3.2.2 Mechanical design

This section discusses the mechanical design of the TwIN turbine. Figure 3.6 shows the components of the TwIN turbine. Two rotary stroke bushes support the axle to which the rotor is attached. In between the supports, a mechanical break is present, which has the function of creating extra resistance when the rotor approaches 3000 RPM. This is a safety measure to avoid a high RPM of the rotor during operation. In addition, the gear transmission increases the rotational speed of the upper axis so that it better fits the operation conditions of the generator during operation. The performance of the TwIN turbine is found by measuring the torque, thrust, and RPM of the system using the load cells and the magnetic encoder. These components are further elaborated in section 3.2.3.

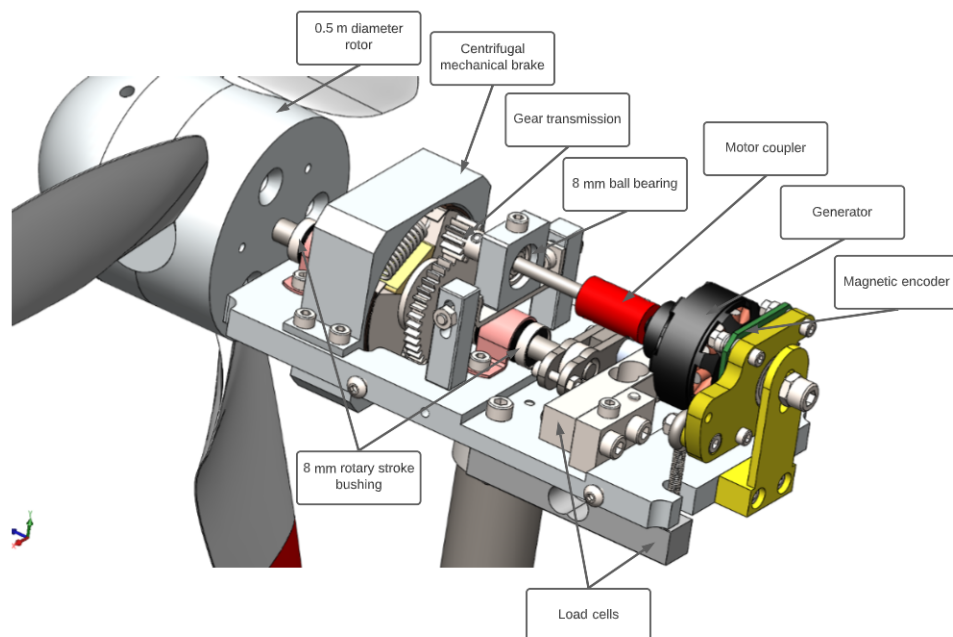


Figure 3.6: Mechanical design wind turbine

3.2.3 Electrical design

This section discusses the TwIN turbine's electrical design. First, the electrical circuit is presented then the different sensors and equipment within the circuit are elaborated.

Electrical circuit

Figure 3.7 demonstrates the schematic view of the electrical circuit. The figure shows that the load cells, magnetic encoder, and current sensor are connected to the Arduino Nano. The Arduino contains a code that processes the incoming data to usable measurement quantities. The code can be modified with the open-source IDE software. The Arduino itself is connected to a computer for the power supply. The data itself is displayed on the connected LCD. Furthermore, figure 3.7 shows that the generator is connected to a 3-phase rectifier which transforms the AC voltage into a DC voltage. The DC voltage is then directed through an electrical load where electrical resistance can be modified with a potentiometer. The adjustment of the electrical resistance controls the rotor's rotational speed.

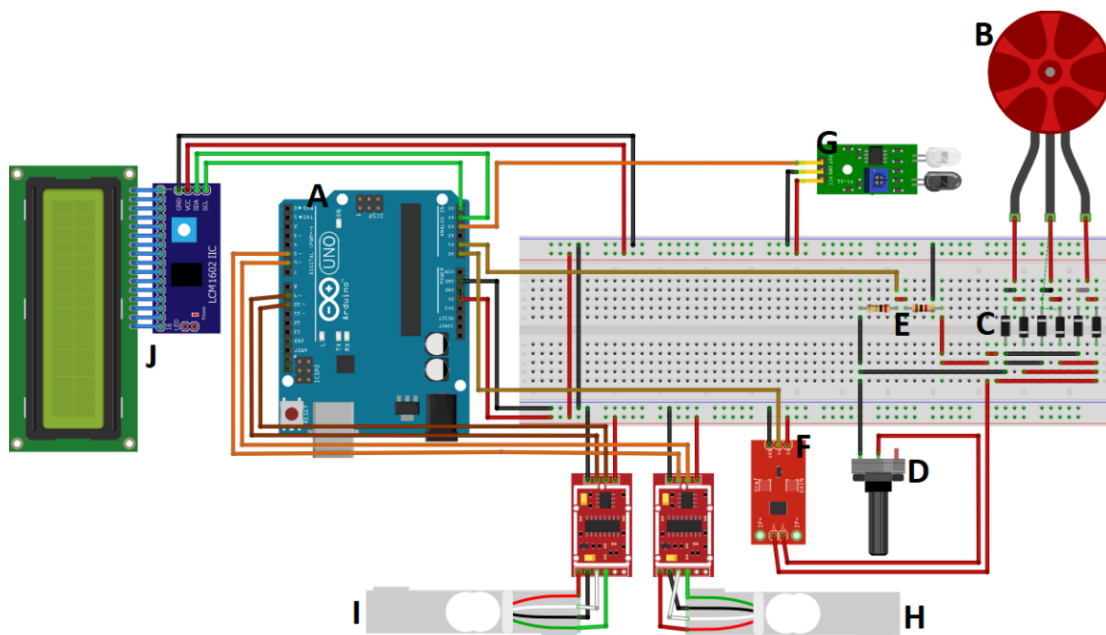


Figure 3.7: Electrical design in which A. Arduino Nano micro-controller; B. Generator; C. 3-phase rectifier; D. Potentiometer electrical load; E. Voltage divider; F. Current sensor; G. magnetic encoder; H. Thrust load cell; I. Torque load cell; J LCD with I2C module [2]

Generator

Mechanical energy is converted into electrical energy using a Brushless DC (BLDC) motor. This type of motor features magnets within the rotor and an arrangement of coils in the stator, as shown in Figure 3.8. Upon rotation of the turbine, the rotor with its magnets begins to rotate, leading to a change in the position of the permanent magnets relative to the electromagnets, resulting in a fluctuating magnetic field around the electromagnets. This fluctuating magnetic field induces an Alternating Current (AC) in the electromagnets. Appendix B.1 provides the datasheet for the motor.

The AC current is transformed into a Direct Current (DC) signal through a rectifier. Appendix B.2 presents the datasheet for the rectifier used in the circuit.

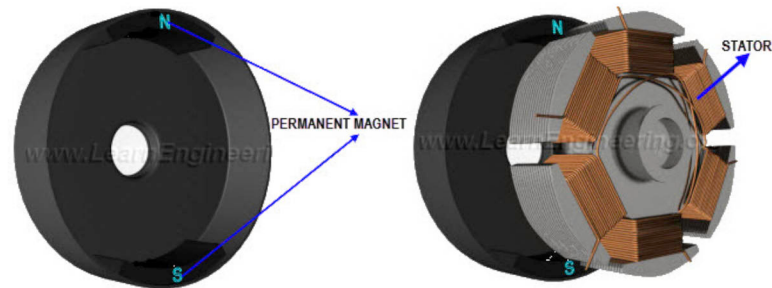


Figure 3.8: Brushless DC motor [14]

Strain gauges

The measurement of the torque and the thrust is done with the use of load cells. This device is, in essence, a cantilever beam with strain gauges attached to the upper and lower side of the beam (figure 3.9.b). The strain gauges are stressed or compressed if a force is applied to the beam, influencing their electrical resistance. The resulting voltage is then measured and related to the force. The strain gauges are placed in a Wheatstone bridge configuration 3.9.a.

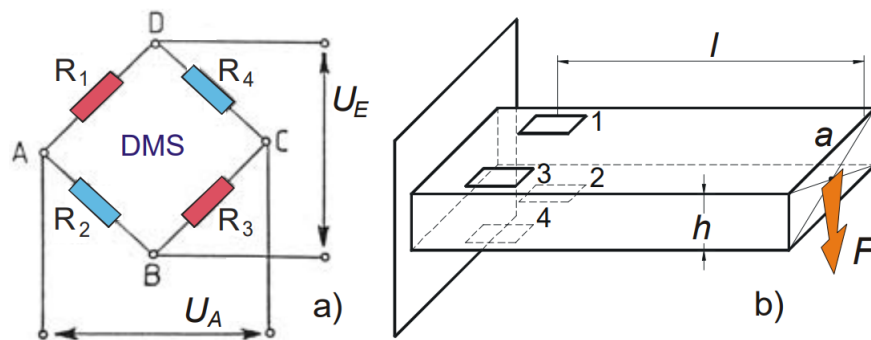


Figure 3.9: Strain gauge positioning along a cantilever beam [15]

RPM sensor

The rotation per unit is measured with the use of a magnetic encoder. The device detects the magnetic field created by a diametrical magnet attached to the generator if the generator is rotating. An analog voltage is produced, which goes through the microcontroller of the Arduino, thus processing the incoming data. The magnetic encoder is placed between the suspension plate and the generator, as shown in figure 3.10.

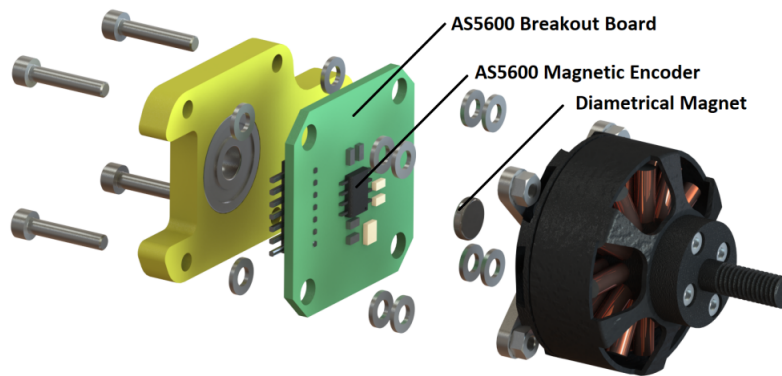


Figure 3.10: The magnetic encoder is placed between the generator and suspension plate [2]

3.2.4 Points of improvements of TwIN turbine

During the calibration (section 6), it was determined that achieving proper alignment between the generator axis and the rotor axis was challenging. To assess this issue, it may be beneficial to incorporate a planetary gearbox which has the potential to significantly reduce the misalignment between the generator axis and rotor axis. It was further discovered that the rotor design is heavy, resulting in a substantial moment of inertia that needs to be overcome during operation. Therefore, it may be beneficial to redesign the rotor to a lighter variant to improve the turbine's performance. During the experimental phase of the graduation period of Cedric [1] and Rowan [2] van Wijk, several issues were unidentified. The most significant problem encountered was that the designed load experienced overheating at low electrical resistance and high wind speed, potentially leading to a fire hazard. Additionally, adjustments to the electrical resistance were made with alligator clips. This method resulted in significant variations in electrical resistance, leading to large rotational speed fluctuations. It was also observed that the range of electrical resistance of the designed electrical load introduced limitations on the range of rotational speed that could be achieved. These issues could be resolved by integrating a programmable external electric load within the electrical circuit. Furthermore, the torque sensor malfunctioned. A suggestion was the integration of a rotary torque sensor. During a premaster project, it was also reported that the mechanical break had failed [16]. Further investigation revealed that the brake braces holding the flyweights did not follow the flyweight's contour, which may have contributed to the failure.

3.3 Acoustic microphone array

The sound sources of the TwIN turbine present during operation were localized with an acoustic microphone array with an integrated camera. Figure 3.11 presents the aeroacoustic camera. The microphone array has a diameter of 1000 mm and consists of 112 Micro Electro-mechanical system (MEMS) microphones. Figure 3.12 illustrates the simplified structure of a MEMS microphone. Here a sound or pressure variation results in a vibration of the lower plate. This vibration is then transformed into an electrical capacitance variation using the perforated fixed electrode (upper plate). The microphone array is connected to an external notebook that collects and stores incoming signals in binary TDMS files, developed by National Instruments [17]. Software present in the notebook processes the TDMS files with a Fast Fourier Transform (FFT) algorithm to ultimately calculate the Discrete Fourier Transform (DFT) of a microphone signal [18]. Subsequently, the power spectrum of the sig-

nal is computed using the Welch algorithm [19], enabling the analysis of the magnitude of sound at specific frequencies. The localization of the sound sources is achieved through the delay-and-sum algorithm [20]. This technique involves delaying the microphone signals and subsequently aligning and summing them together.



Figure 3.11: Acoustic camera - Bionic M-112 array [21]

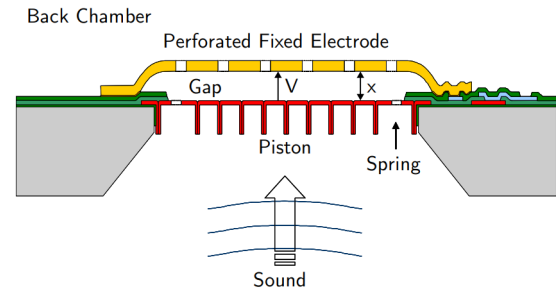


Figure 3.12: Working principle of MEMS microphone [22]

Design modifications

4.1 Mechanical design

This section describes the modifications for the mechanical design of the TwIN turbine. Two main modifications were done: The brake linings were reproduced, and the rotor hub was modified.

4.1.1 Brake linings

During the research period of Cedric and Rowan, it was found that the centrifugal brake comes in at approximately 3250 RPM. However, the rotor was designed to brake at a maximum of 3000 RPM. Furthermore, the brake malfunctioned during the premaster period. After analysis of the centrifugal brake, it became clear that the brake linings did not follow the same contour as the flyweights. It was assumed this was the cause of the malfunction. Therefore, the brake linings holding the flyweights were reproduced. The old brake linings were constructed using 0.5 mm spring steel. Spring material deforms to its original shape after rolling. An alternative material for the brake linings was sheet metal which is less prone to deformation after rolling. The brake linings were made with a thickness of 1 mm, which is 0.5 mm higher than the old brake linings. The thickness was increased to decrease the RPM at which the brake linings touched the housing. Figure 4.1 shows the old and new brake linings. Figure 4.2 demonstrates the entire assembly of the centrifugal brake with the new brake linings.



Figure 4.1: Old brake lining (upper) and new brake lining (bottom)



Figure 4.2: Centrifugal brake with new brake linings

4.1.2 Rotor hub modification

The rotor axis started slipping in the hub's radial direction during the torque calibration. Section 6.2 describes this calibration procedure. The old rotor hub (figure 4.3) was attached to the rotor axis with one stud bolt going through a tapped hole within the hub. It was found that the stud bolt unscrewed itself after a high torque was present on the rotor. A metal helicoil was inserted in the hole to create more friction on the stub bolt. Another hole was made in the side of the rotor hub to create two attachment points and decrease the force working on one stud bolt. Figure 4.4 shows the new hub design. Furthermore, it was found that the hole for the rotor axis was too short, so the hole in the hub could not align with the notch on the axis. Figure 4.5 shows the extension done of the rotor axis hole (red colored) to align the holes with the notch.

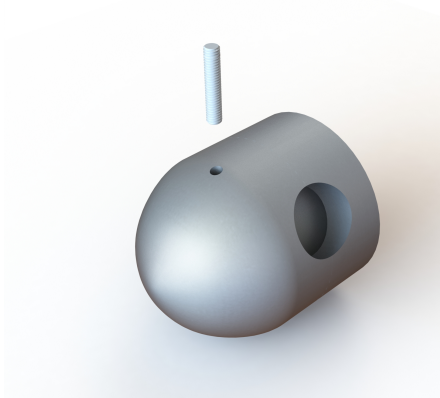


Figure 4.3: Old hub

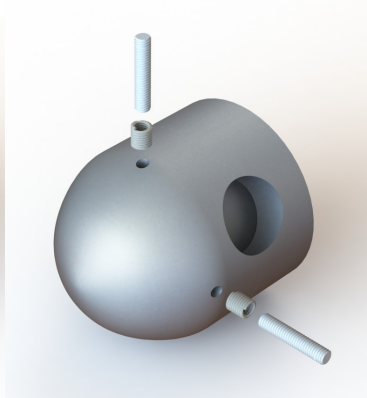


Figure 4.4: New hub

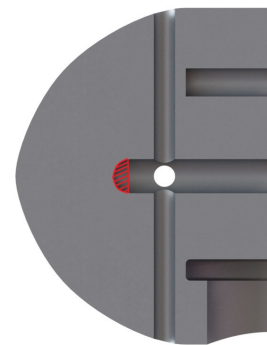


Figure 4.5: Extension

4.2 Electrical design

This section describes the modifications to the wind turbine's electrical design. The most significant change was the integration of an external programmable electronic load. This device made it possible to program and apply the amount of electrical resistance going over the electronic load. The electronic load was connected to a computer which allowed for the saving of electronic data along a predefined measurement time. A LabVIEW program has been developed to communicate with the Arduino and the electronic load.

4.2.1 DC electronic load

A DL3000 series programmable DC electronic load was available within the university of Twente [23] (figure 4.6). This device was integrated within the TwIN turbine's electrical design because the existing electrical load experienced various problems during the testing phase of the graduation period of Cedric and Rowan van Wijk [1], [2]. One of the problems was that the electrical resistance was limited to 20Ω , which meant only a small limit of TSRs and desired wind speeds could be tested. Another problem was that the electronic load overheated at a high wind speed. This happened because a large current was drawn from the generator, resulting in a large amount of energy dissipating over the resistors. The current potentiometer in the electrical circuit (figure 3.7) is replaced with the DL3000. The external load consists of 4 static modes (constant current, constant voltage, constant resistance, and constant power) and three dynamic modes (continuous, pulsed, and toggled). For the

data acquisition, it was chosen to use the constant resistance load mode that can vary the electrical resistance over the DC load.



Figure 4.6: RIGOL DL3021 - DC external load

4.2.2 Modification Arduino perfboard

The connection between the Arduino and the computer malfunctioned when the pins of the load cells and the magnetic encoder were connected to the perfboard headers. This failure may have been caused by a wire connection on the perfboard being destroyed by wear, causing a short circuit. For this reason, the old perfboard (figure 4.7) was modified into a new perfboard (figure 4.8). Figure 4.8 shows that screw terminals replace the old header connections from 4.7. These screw terminals create a tighter connection between the perfboard and the wires from the load cells and the magnetic encoder. Pin terminals were attached to the end of the wires to avoid damage. The connection between the screw terminals and the Arduino was realized with soldered connections, unlike the old Arduino perfboard, which was done with jumper wires. Soldered connections are generally considered more reliable and secure than wire connections.

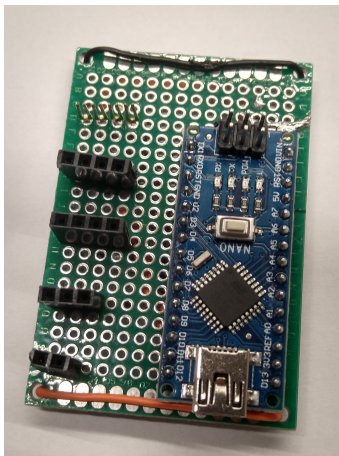


Figure 4.7: Old Arduino perfboard

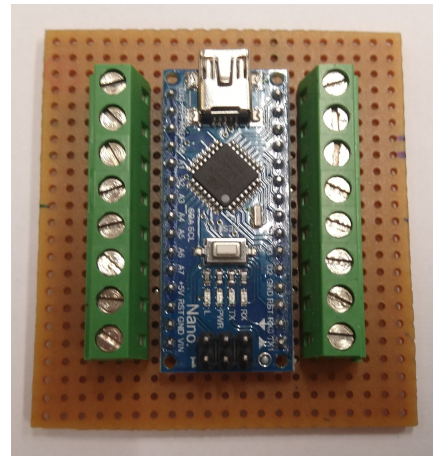


Figure 4.8: New Arduino perfboard

4.2.3 Modification Arduino code

The existing Arduino code allowed it to read data from the LCD screen within the electrical circuit. However, it is also possible to read the serial port of the Arduino from a computer by connecting the Arduino to the computer's USB port. The advantage of this connection is that the computer can save the data automatically instead of manually writing it down from the LCD. It also becomes easier to analyze the data's deviation and transient behavior. Appendix C shows the modified Arduino code to make it possible to read out the serial port from a computer.

4.2.4 LabVIEW program

The Arduino and the external electronic load communicate with the computer using a LabVIEW program. LabVIEW is a graphical programming environment developed by National Instruments. It is characterized by two environments: the user interface and the schematic view of the program. The user interface allows the user to interact with the program by pressing buttons or switches that execute operations for the connected instruments. It also enables the display of gathered data in a programmer-defined format and the definition of the file name for saved data. The schematic view of the program shows how different functions or Virtual Instruments (VIs) communicate with each other, ultimately creating the program.

Appendix D shows the developed LabVIEW program. Figure 4.9 shows the second tab of the LabVIEW interface. In the first tab, the user can define the measurement time, the sampling rate, and the file location of the created text file with the acquired data. There are buttons located at the top of the panel. When the "read" button is pressed, data is gathered for the specified measurement time and sampling rate. The interface automatically switches to the second tab of the data interface, as shown in figure 4.9. This tab displays a graph of the power as a function of the RPM and a response block with the collected data being saved in the text file. The "manual control electronic load" tab contains buttons that enable the user to turn the external electronic load on or off. In addition, the user can adjust the electrical resistance in the "adjustment" tab. The buttons in the "list control electronic load" tab control the list function in the electronic load. This function allows the user to specify the amount and duration of a specific electrical resistance applied to the load. The "text" tab provides an example of a code configuring the list function using the DL3000 programming language. The code is written to the electronic load when the "configure list" button is pressed. The "start/pause list" button can be used to start and pause the list function. This button also automatically starts the data acquisition.

Initially, the plan was to use the developed LabVIEW program to communicate with the instruments in the wind tunnel. However, due to compatibility issues between the wind tunnel program and the program of the TwIN turbine, certain VIs from the wind tunnel LabVIEW program were unable to load within the LabVIEW program for the TwIN turbine. This problem was not resolved due to time constraints and may be addressed in future development.

4.2.5 Modification of the electronic circuit

The previously mentioned modifications made it possible to eliminate elements within the electric circuit. Figure 4.10 demonstrates the new schematic circuit of the electronic circuit. The electrical system consists of the following components: The Arduino nano [A], the generator [B], the full bridge rectifier [C], the DL3000 external load [D], the magnetic encoder [E], the thrust load cell [F], and the

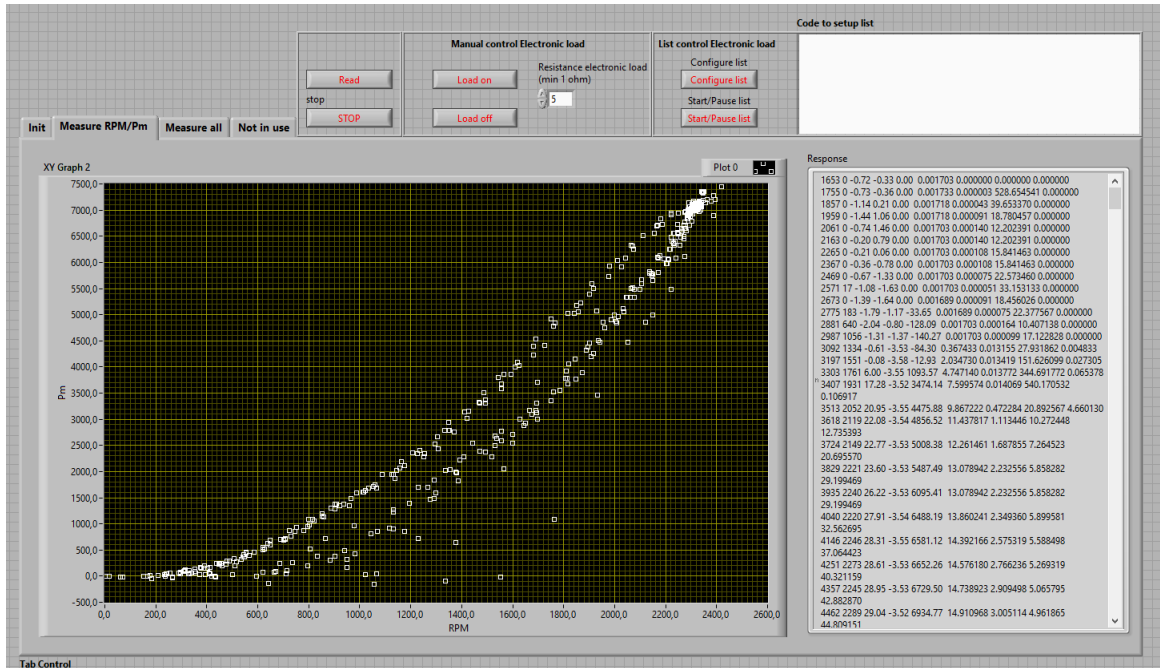


Figure 4.9: Interface data acquisition

torque load cell [G]. The Arduino and the external electronic load are connected to a computer that processes the data with the previously mentioned LabVIEW program.

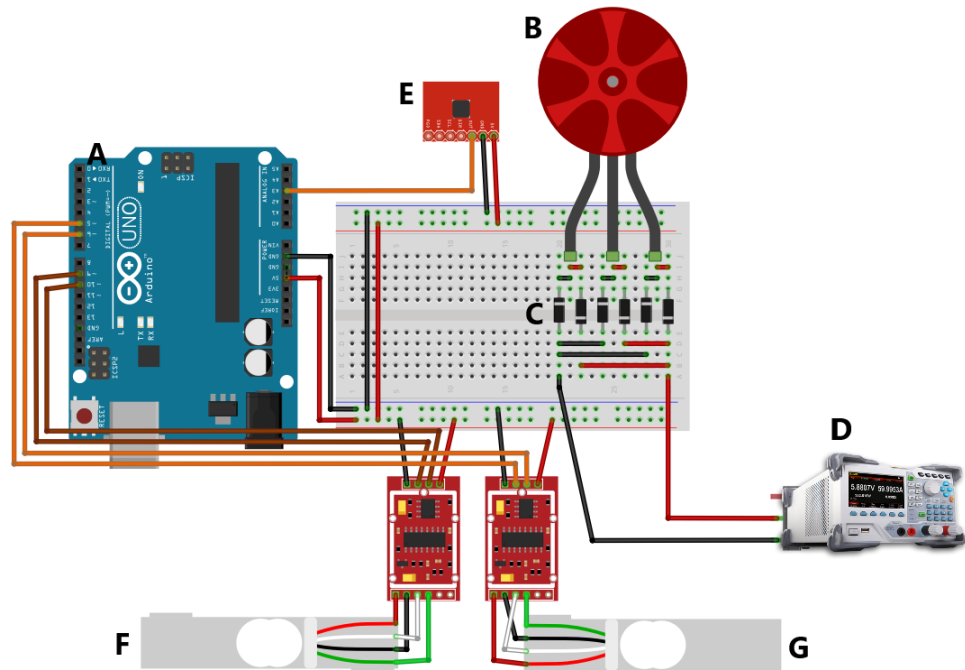


Figure 4.10: Modification electronic circuit

Aerodynamic analysis

5.1 QBlade software

The open-source software QBlade is used to design and analyze wind turbines by focusing on the turbine's aerodynamics and structural dynamics. One of the main advantages of this software is its use of BEM (Blade Element Momentum) and vortex models to generate robust predictions of the aerodynamic characteristics of a wind turbine. These techniques use less computational time than other aerodynamic analysis techniques such as RANS (Reynolds-Averaged Navier-Stokes) models. The BEM technique in particular allows for significantly faster computational times than other techniques, making it an efficient option for blade design and aerodynamic performance prediction of a turbine.

5.2 Previous aerodynamic research

The aerodynamic design of the TwIN turbine was designed by Cedric van Wijk [1] with the use of the QBlade design tool. The design tool uses BEM theory to create the ideal blade geometry for a given tip speed ratio and wind speed. The blade was divided into several elements in which the optimal chord and twist for each section were determined to achieve the best performance at the design tip speed ratio of 4. The lift and drag coefficient at every section were determined using the experimentally obtained polar [24] available for the SD7037 airfoil profile geometry in the blade. It is important to note that the aforementioned polar only provided lift and drag coefficients for a small range of angle of attack values. The lift and drag coefficient was extrapolated over the full range of 360 degrees of angles of attack by utilizing the Viterna method within the QBlade 360° module. The extrapolation method is further elaborated in section 5.3.2. Within Cedric's report, it was recommended to perform future simulations using the Montgomerie method, as the Viterna method underestimated the TSR at which stall occurs.

5.3 Aerodynamic analysis

In a previous aerodynamic analysis by Cedric [1], an investigation was performed with QBlade using BEM theory that examined the performance as the function of the TSR, the blade's pitch angle, and the wind speed. In Cedric's analysis, two of these parameters were held constant at the design conditions, while the third parameter was varied. This section explains the new aerodynamic analysis performed with QBlade that includes more tip speed ratios and pitch angles.

5.3.1 Airfoil characteristics

The lift and drag coefficient for the SD7037 airfoil as a function of the angle of attack is provided via the experimental work of Selig [24]. From this work, the lift and drag coefficients were tested for both tripped and smooth airfoils. However, it is almost impossible to predict the transition locations on the rotor blade of the TwIN turbine. Because of this reason, the airfoil characteristics of the tripped data are used. This way, trips can still be added to the blades within the experimental phase if the experimental results deviate too much from the QBlade prediction. Figure 5.1 shows the airfoil's lift over drag diagram for the SD7037 airfoil for three different Reynolds numbers. The airfoil lift over drag diagram for the untripped SD7037 airfoil is shown in appendix E.

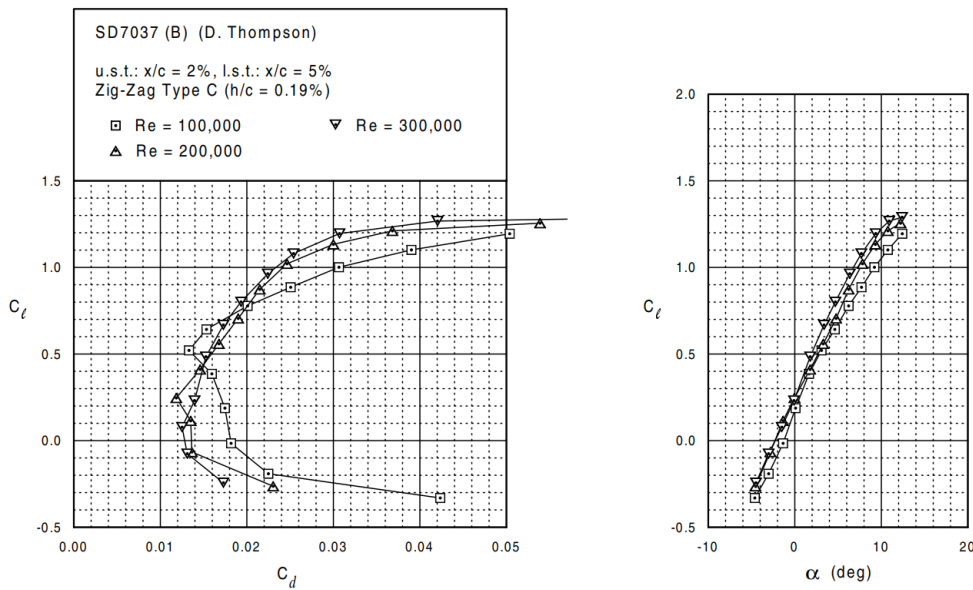


Figure 5.1: SD7037 Airfoil Characteristics [24]

A prediction of the Reynolds number along the rotor blade was made using the blade element theory (Section A.3). An Excel calculation sheet was created, using this theory. Appendix F.2 presents the calculation sheet. The geometric data of the rotor blade is illustrated in Figure F.1, within Appendix F.1. The rotor blade has been divided into 23 elements and the Reynolds number is calculated for each element. In the calculation sheet, the axial induction factor was kept at $1/3$, the tangential induction factor was kept at 0, and no corrections were applied. These settings result in a robust prediction of the Reynolds number using the blade element theory. However, in reality, the induction factors vary along the radius of the rotor blade. These factors can be calculated using QBlade's BEM-module [25]. The predictions made using QBlade are discussed in the sections 5.3.5 and 5.3.6.

Figure 5.2 shows the Reynolds number along the blade calculated with the excel calculation sheet. One can observe that the highest Reynolds number occurs at the blade's middle while decreasing at both the tip and root. In order to utilize the BEM module within QBlade, an airfoil characteristic, as shown in Figure 5.1, must be used as input. The lowest Reynolds number is 100,000, which corresponds to the middle part of the blade. This part generates the most torque and is the primary contributor to the power coefficient's computation. Therefore, the experimental airfoil lift and drag characteristics at a Reynolds number of 100,000 are used as input for QBlade. It is important to note that this implies that the lift and drag characteristics are defined as the same along the radius of the blade, which is not the case in reality. This inaccuracy is expected to have some effect on the

calculation of the power and thrust coefficient.

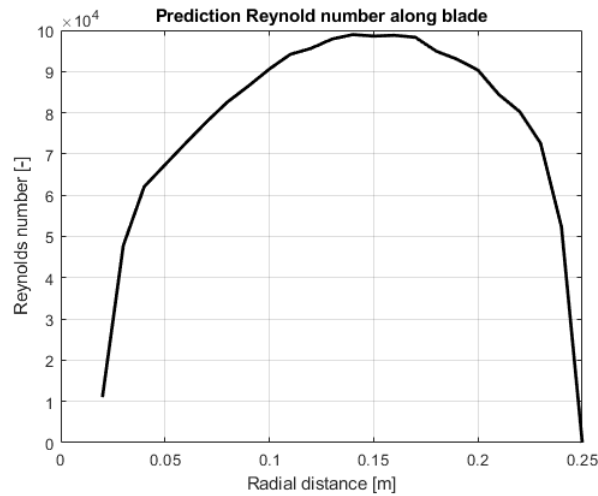


Figure 5.2: Reynolds along rotor blade

5.3.2 Extrapolation of experimental data

The lift and drag coefficients obtained from the experimental results have been provided for a limited range of angles of attack, ranging from -4 to 12 degrees. The polar is made usable for analysis within Qblade by extrapolating over the full range of 360 degrees of angles of attack values. Qblade makes use of two extrapolation methods, namely the Montgomerie extrapolation method [26] and the Viterna extrapolation method [27]. Both methods use a mathematical formulation with parameters that can be tuned to gain a plot for the drag and the lift over 360 angles of attack. Figure 5.3 shows the extrapolation executed with the Montgomerie method. It is essential to consider that the lift and drag coefficients within the extrapolated area are of low accuracy, regardless of the extrapolation method used.

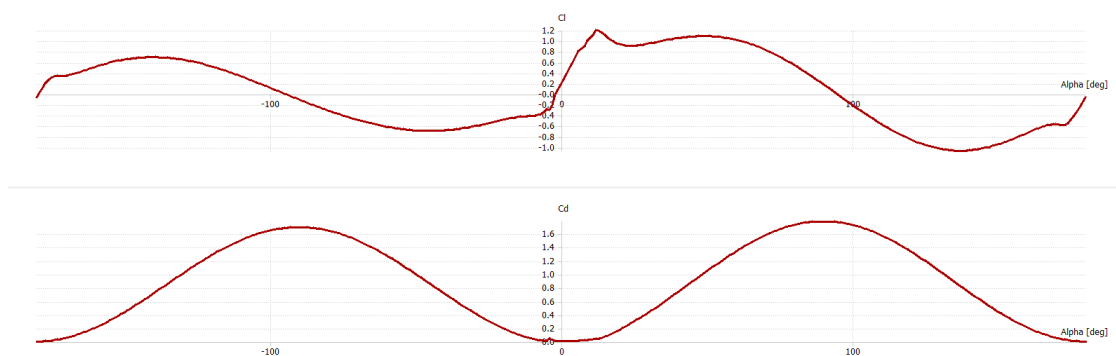


Figure 5.3: Extrapolation of Montgomerie method

5.3.3 Corrections in Qblade

Classical BEM theory uses 2-dimensional airfoil data to describe a 3-dimensional problem. This simplification leads to some 3-dimensional phenomena that are not described using classical BEM theory. In Qblade, one can use corrections to account for the 3-dimensional effects. The corrections

are explained in this section. Appendix A.4 shows the expressions for the correction factors.

Tip- and root-losses

The blade's finiteness at the tip and root of the blades leads to vortices due to the pressure difference of the blade. The vortices being shed result in less energy extraction from the wind than is determined with the uncorrected BEM theory. To correct this issue in simulation, the Prandtl tip loss factor [28] can be applied. Prandtl originally introduced this factor and suggested that a series of solid disks can model the wake's helicoidal vortex sheet. This model was expanded by Shen [29], who found that the Prandtl correction exaggerates the tip's loads.

3D corrections

A rotating blade's lift coefficient is higher than a stationary rotor due to the effect of pressure forces working on the boundary layer. The radial pressure gradient accelerates the boundary layer radially. This radial flow generates a Coriolis force that acts favorably on both sides of the profiles. The presence of the Coriolis force results in a delay in the stall compared to a stationary rotor. The two-dimensional SD 7027 profile data is corrected using a semi-empirical formula developed by Snel et al. [30].

Reynolds number drag correction

A constant Reynolds number is used to calculate the turbine's performance. In reality, the lift and drag change as the turbine undergoes different conditions, thus different Reynolds numbers. The drag coefficient is corrected by a formula proposed by Hernandez and Crespo [31]. This formula corrects the drag by inversely scaling the drag coefficient with the Reynolds number.

Foil interpolation

The foil interpolation correction is only used when different airfoils are present within the blade. Because the blade only has one airfoil, this correction is not explained further. It is referred to the Qblade guidelines [25] for a brief explanation.

Influence corrections

Appendix G describes the analysis performed to analyze the influence of the corrections on the turbine's aerodynamic performance prediction.

5.3.4 Settings Qblade

Figure 5.4 shows the settings defined for the rotor simulation. The corrections outlined in Section 5.3.3 were implemented. In addition, it was observed that a lower number of elements resulted in a better convergence of the results. As such, the number of elements was set to 50, as a higher number did not significantly impact convergence but significantly increased computational time. The elements were spaced in a sinusoidal manner, with more elements placed at the tips and root of the blade due to the presence of steeper gradients in these regions. The relaxation factor was set to 0.1, as the simulation had difficulty converging at higher values, likely due to the applied corrections. The convergence criterion was set to $\epsilon = 10^{-4}$, and the number of iterations was constrained to 10,000.

Corrections	Variables
<input type="checkbox"/> Prandtl Tip Loss	50 Discretize Blade into N Elements
<input checked="" type="checkbox"/> New Tip Loss	0.0001 Max Epsilon for Convergence
<input type="checkbox"/> Prandtl Root Loss	10000 Max Number of Iterations
<input checked="" type="checkbox"/> New Root Loss	0.1 Relax. Factor
<input checked="" type="checkbox"/> 3D Correction	1.225 Rho
<input checked="" type="checkbox"/> Reynolds Drag Correction	0.00001647 Viscosity
<input type="checkbox"/> Foil Interpolation	

Figure 5.4: Settings Qblade

5.3.5 Varying TSR

This section explains how the TSR affects the thrust and power of a turbine. The influence of the TSR on pitch angles of -5, -2.5, 0, 2.5, and 5 degrees was examined. The figures 5.5 and 5.6 show these results. Figure 5.5 shows that an increase in pitch angle results in a lower overall thrust. The difference in thrust increases with higher tip speed ratios. Figure 5.6 illustrates that the highest power coefficient is obtained at a pitch of 0 degrees and a TSR of approximately 4.5. It should be noted that the results obtained in the low TSR regime are greatly dependent on the QBlade's 360 degrees extrapolation module and, thus, not accurate.

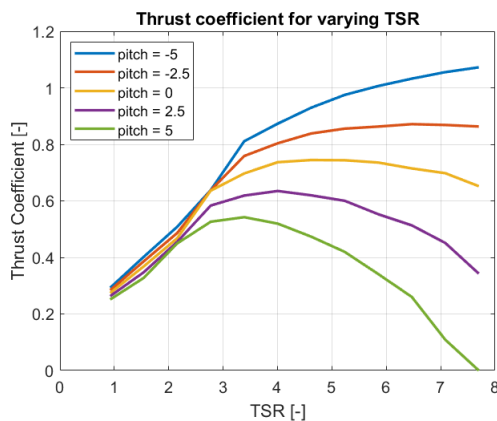


Figure 5.5: Thrust coefficient as function of TSR

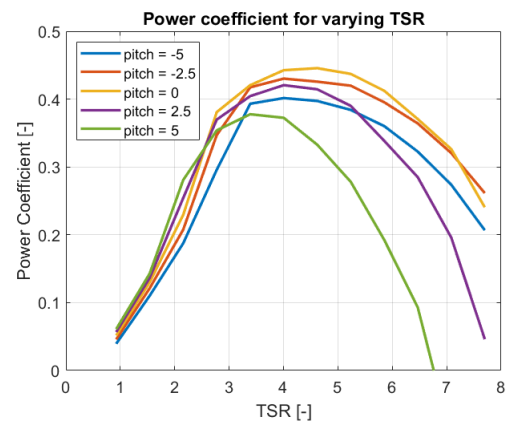


Figure 5.6: Power coefficient as function of TSR

5.3.6 Varying pitch angle

This section describes the pitch angle's influence on the thrust and power of the TwIN turbine. The effect of the pitch angle on four different tip speed ratios, specifically 3, 4, 5, and 6, is analyzed. Figures 5.7 and 5.8 displays the result. It should be noted that positive pitch angles turn the blade's leading edge more into the wind.

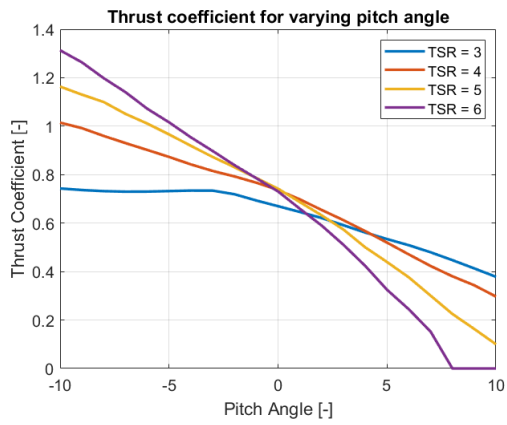


Figure 5.7: Thrust coefficient as function of pitch angle

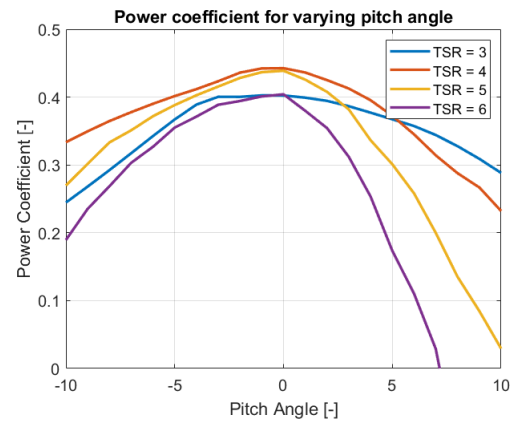


Figure 5.8: Power coefficient as function of pitch angle


Preliminary testing

6.1 RPM calibration

The magnetic encoder, located between the generator and the suspension plate, measures the RPM of the generator. The Arduino microcontroller then processes the encoder's analog data to determine the rotor's rotational speed. The Testo 470 RPM counter (figure 6.1) was used to verify whether the system accurately measures the rotational speed with the magnetic encoder and the Arduino. The Testo 470 uses a laser that detects the times a reflective tape passes by the laser within an instant. The LCD then displays the average RPM and the maximum and minimum RPM within a measurement time. A drill was attached to the rotor's axle, in which the drill's torque was gradually increased. For each torque, the RPM measured by the encoder is compared to the RPM measured by the Testo 470. During the data acquisition, the measurement time for both the Testo 470 and the Arduino were set to 20 seconds. The sampling frequency of the Arduino was set to 10 Hertz. The RPM for each measurement acquired by the Arduino was found by taking the average over all data points.

Table 6.1 shows the comparison of the RPM found by the Testo 470 (first column) and the RPM found by the magnetic encoder and the Arduino (second column). One can observe that the absolute value of the maximum RPM found by the Arduino was significantly higher than the absolute value of the minimum RPM found. This difference is caused by a slight misalignment of the diametric magnet with respect to the magnetic encoder. The misalignment resulted in the generation of data points that were too high compared to the statistically expected data distribution. These outliers were distinguished easily from the distribution and were removed. The mean of the remaining data points for each measurement was then recalculated (third column).

Table 6.1 also shows that the corrected RPM found by the magnetic encoder is closer to the RPM found by the Testo 470 than the uncorrected RPM found by the magnetic encoder. Removing the outliers caused the average RPM of the data to decrease, as seen in the table. Removing the outliers reduces the average RPM because they are too high compared to the expected RPM. Furthermore, table 6.1 shows that a higher applied torque from the drill led to higher fluctuations of the RPM. The higher fluctuations for higher torques are evident both from the data from the magnetic encoder and the Testo 470. The distribution of the data was considered acceptable.



RPM testo 470	RPM magnetic encoder	RPM magnetic encoder (corrected)
197 ⁺² ₋₁	209 ⁺³³ ₋₃	199 ⁺⁶ ₋₃
287 ⁺² ₋₂	301 ⁺⁶² ₋₃	285 ⁺⁷ ₋₃
452 ⁺⁵ ₋₄	459 ⁺⁵⁷ ₋₄	456 ⁺⁹ ₋₄
612 ⁺⁷ ₋₆	620 ⁺¹⁰² ₋₁₀	613 ⁺²³ ₋₁₀
811 ⁺⁷ ₋₁₀	822 ⁺¹³⁶ ₋₁₄	815 ⁺²⁹ ₋₁₄
1149 ⁺¹⁶ ₋₁₃	1162 ⁺¹⁷³ ₋₁₉	1153 ⁺³² ₋₁₉
1604 ⁺²⁰ ₋₂₂	1613 ⁺²³¹ ₋₂₈	1607 ⁺³⁷ ₋₂₈
2018 ⁺²⁷ ₋₃₄	2030 ⁺²⁰⁸ ₋₃₉	2024 ⁺⁵³ ₋₃₉

Figure 6.1 & Table 6.1: Testo 470 [32] with average measurement data

6.2 Torque sensor calibration

The load cell measuring the torque was calibrated using the dead weight method. An external metal piece of equipment was attached to the hub. The hub was then attached to the rotor axle. A torque was created on the rotor by hanging weights on the arm at a predefined distance from the center of the rotor. The gear transmission then transferred the torque from the rotor to the generator. The generator was fixed to the arm attached to the load cell with a piece of tape to prevent free rotation. The torque was then measured by the load cell, the Arduino, and the LabVIEW program. The experimental setup is shown in the figures 6.2 and 6.3.



Figure 6.2: Torque calibration front view



Figure 6.3: torque calibration side view

The Arduino processes the data such that the torque is given with only two decimals. When using the SI system, the torque is given in Nm. Previous experiments [1], [2], [16] showed that at wind speeds around 10 m/s, torques were measured in between 0.10 and 0.30 Nm. If torques were present around 0.105 Nm, the Arduino would process the signal such that the value jumped to 0.10 or 0.11, leading to large rounding errors. An easy way to reduce the rounding error for low values is to measure the values in Ncm instead of Nm. With this adjustment, three sets of six different measurements were performed. Each measurement had a sample time of 20 seconds and a sampling frequency of 10 Hertz. The data were then averaged over all data points for each measurement. Table 6.2 shows the result for three sets.

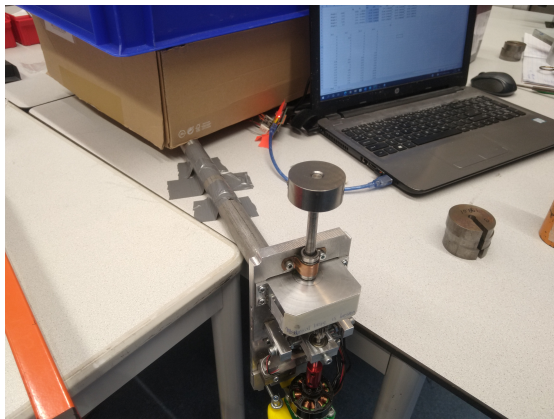
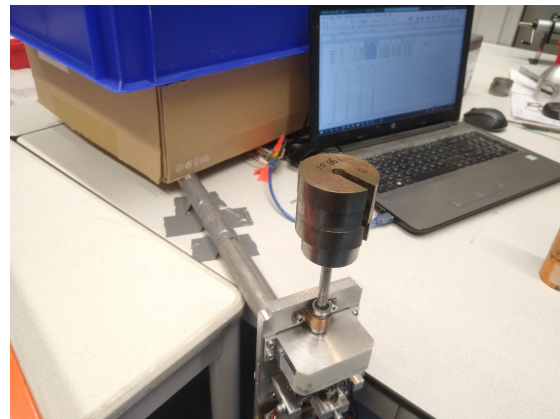
Table 6.2: Torque calibration

Torque applied (<i>Ncm</i>)	Set 1 (<i>Ncm</i>)	Set 2 (<i>Ncm</i>)	Set 3 (<i>Ncm</i>)	max. error (%)
12.36	12.63 ^{+0.16} _{-0.13}	12.56 ^{+0.14} _{-0.12}	12.21 ^{+0.14} _{-0.13}	2.1
27.78	28.41 ^{+0.16} _{-0.15}	28.32 ^{+0.11} _{-0.13}	28.51 ^{+0.18} _{-0.17}	2.6
54.48	55.16 ^{+0.12} _{-0.17}	55.87 ^{+0.18} _{-0.14}	55.97 ^{+0.16} _{-0.12}	2.7
82.20	83.64 ^{+0.24} _{-0.24}	83.26 ^{+0.13} _{-0.17}	83.07 ^{+0.21} _{-0.19}	1.7
109.89	112.61 ^{+0.16} _{-0.22}	111.48 ^{+0.25} _{-0.28}	112.24 ^{+0.25} _{-0.15}	2.5
137.74	140.21 ^{+1.13} _{-1.22}	141.02 ^{+1.11} _{-1.53}	142.32 ^{+0.45} _{-0.76}	3.3

The first thing observed is the high deviation for the last measurement. The main reason for this was that if a lot of weight were attached to the arm, the tape-fixated generator would slowly slip from the arm attached to the load cell. This phenomenon decreased the total torque as the arm with attached weights became shorter. The results also show that the maximum error remained between 1.7 and 3.3 %. This error was considered acceptable. One should note that the relative error of the last measurement is probably higher as the torque was decreased through the slipping of the tape-fixated generator. Furthermore, it is observed that the absolute error increased with increasing torque. Because the applied weights were not precisely at a distance of 0.14 *m*, the absolute error increased if one added more weight.

6.3 Thrust sensor calibration

The load cell measuring thrust was calibrated by clamping the turbine horizontally and applying weights axially to the rotor shaft on a fixed metal platform. The load cell measuring the thrust then absorbs the downward force. The calibration was done by comparing the data from the Arduino to the known downward force. The figures 6.4 and 6.5 show the setup for the calibration.

**Figure 6.4:** Thrust calibration no weights**Figure 6.5:** Thrust calibration with weights

Three sets of five measurements with different weights were performed for the thrust calibration. After the first five measurements, one additional measurement was performed to measure the thrust value with no weights placed on the shaft. This was done to check whether the measured value differed from the initialization value. Each measurement had a sample time of 20 seconds and a sampling frequency of 10 Hertz. The thrust was then determined by taking the average over all data points for each measurement. Table 6.3 shows the results for the thrust calibration.

Table 6.3: Thrust calibration

Force applied (N)	Set 1 (N)	Set 2 (N)	Set 3 (N)	max. error (%)
5.90	5.91 ^{+0.01} _{-0.02}	5.81 ^{+0.01} _{-0.01}	5.93 ^{+0.01} _{-0.01}	1.5
10.90	10.96 ^{+0.02} _{-0.02}	10.82 ^{+0.02} _{-0.03}	10.95 ^{+0.01} _{-0.02}	0.7
15.90	15.97 ^{+0.03} _{-0.02}	15.91 ^{+0.02} _{-0.01}	16.01 ^{+0.01} _{-0.01}	0.7
19.92	20.14 ^{+0.02} _{-0.02}	20.08 ^{+0.03} _{-0.02}	20.16 ^{+0.02} _{-0.03}	1.2
24.83	25.07 ^{+0.04} _{-0.02}	25.10 ^{+0.03} _{-0.03}	25.15 ^{+0.04} _{-0.03}	1.3
0	0.10 ^{+0.01} _{-0.01}	0.04 ^{+0.01} _{-0.01}	0.11 ^{+0.01} _{-0.01}	-

Table 6.3 shows that the maximum relative error was present for the lower and higher load. All measurements contained a relative error between 0.7 and 1.5 %. These errors were considered acceptable. Furthermore, it is observed that the last measurement of the three sets displays thrust values not equal to the initial value measured by the load cell (= 0.00). The non-zero value may be present because the system creates an additional axial force on the rotor shaft in the opposite direction of the force applied. The absolute error due to this phenomenon is relatively low and is neglected. It is also observed that the deviation is low for all measurements.

6.4 Generator testing

The expected electrical performance of the BLDC motor in combination with the 3-phase rectifier and the external load was compared to the experimental electrical performance. The expected rectified DC voltage is required to determine the expected current and power. The rectified DC voltage going over the external load is calculated with the use of equation 6.1 [33].

$$U_{DC,r} = \frac{3}{\pi} \cdot \left(\frac{\pi}{3} \cdot \frac{n_{gen}}{k_{gen}} - R_{gen} \cdot I_L \right) - 2 \cdot \Delta V \quad (6.1)$$

Equation 6.1 shows three different terms; the first term indicates the maximum power generated from the generator without losses, the second term represents the losses due to the internal resistance of the generator and the third term represents the losses in the rectifier because of the needed forward voltage of the diodes. The generator constant (k_{gen}) determines the electrical power that is extracted from the generator. The datasheet for the used X3508-390KV motor gives the generator constant and the internal resistance (R_{gen}). These are given as follows [34]:

$$k_{gen} = 390 \text{ RPM/V} \quad R_{gen} = 0.19 \Omega$$

The last term in equation 6.1 is present because the rectifier causes a voltage drop as the diodes require a forward voltage to open. This voltage drop changes slightly as the current varies but typically lies around 0.7 Volts [35].

The experimental current and power were determined by attaching a 3000 RPM no-load drill to the axle of the turbine. Raw data was then collected while the load of the drill was gradually increased. Data was gathered for four different electrical resistances of the connected external electronic load. The figures 6.6 and 6.7 show the comparison of the experimental current and power measured by the external load and the theoretical current and power drawn from the generator.

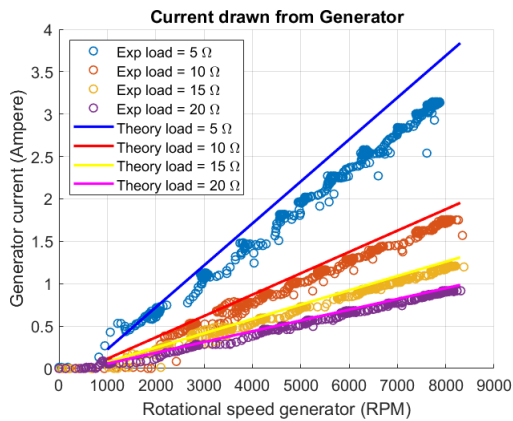


Figure 6.6: Current drawn from the generator for initial generator properties

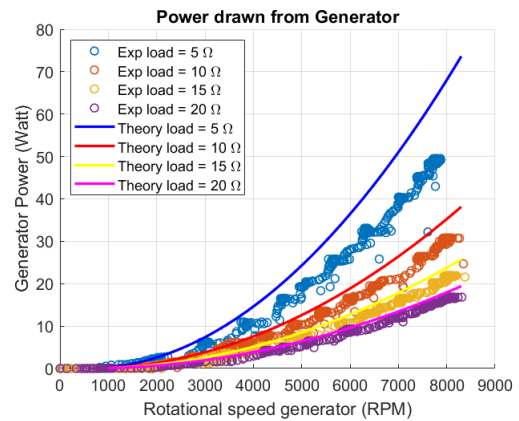


Figure 6.7: Power drawn from the generator for initial generator properties

Figures 6.6 and 6.7 show that the theoretical current and power do not match the experimental data. It is expected that this was because a higher internal electrical resistance is present within the generator than found in the datasheet. Both the generator constant and internal electrical resistance were adjusted such that the theoretical current and power drawn from the generator correspond with the experimental data. The generator constant and internal resistance were adjusted as follows:

$$k_{gen} = 395 \text{ RPM/V}$$

$$R_{gen} = 0.9 \Omega$$

The theoretical current and power with these generator properties were compared with the experimental data. The figures 6.8 and 6.9 show this comparison. The adjusted generator properties are roughly similar to those found in the report from Rowan van Wijk [2]. Since the generator properties are identical, it is assumed that the generator is adequate for the experimental phase of this thesis.

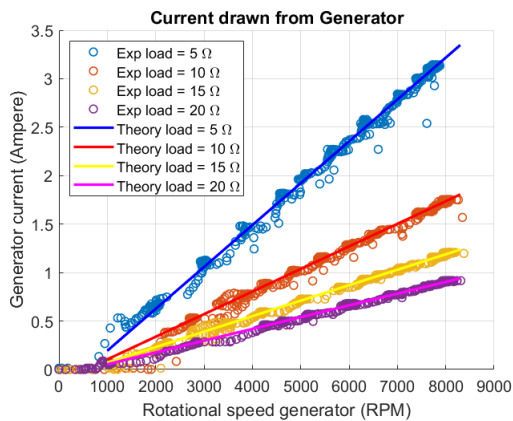


Figure 6.8: Current drawn from the generator for corrected generator properties

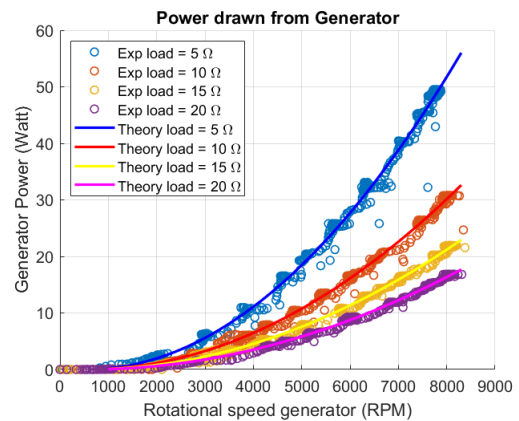


Figure 6.9: Power drawn from the generator for corrected generator properties

6.5 Noise inspector testing

The acoustic microphone array was connected to an external notebook that processes the signals coming from the microphones. The performance of the beamforming algorithm on the notebook was tested by moving an operation drill from one side to the other side of the microphone array during the data acquisition. The drill was kept at a distance of approximately one meter perpendicular to the microphone array. During this data acquisition, a sonogram was created showing the power spectrum at specific intervals. As the drill was kept at a constant speed, the Fourier spectrum was not altered significantly over the measured time. The only thing that changed during the data acquisition was the place of the sound source. During the data acquisition, a video was made synchronized with the beamforming algorithm. Figures 6.10 and 6.11 show two frames extracted from the video. It can be seen that the beams correspond with the sound source displayed in the video.

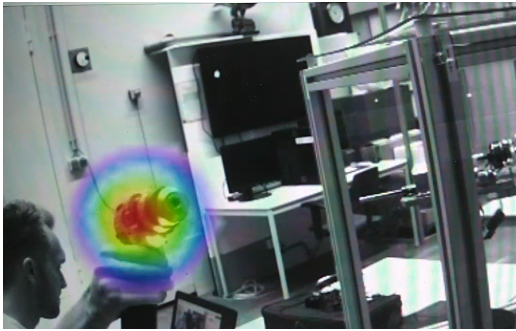


Figure 6.10: Beam 1 of drill

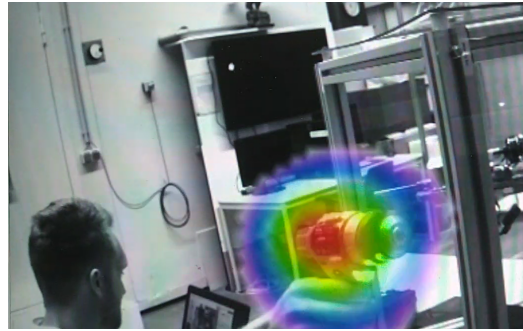


Figure 6.11: Beam 2 of drill

An extensive calibration of the microphones is outside the scope of this thesis. However, it is checked whether the microphones sufficiently measure the frequencies from a sound source. This was done by emitting tones at certain frequencies from a speaker. All microphones then captured the tones in the microphone array. It was found that the tones were captured with high accuracy in the power spectrum.

Experimental work

7.1 Experimental setup

Two configurations were tested during the wind tunnel time: one with a floor and a ceiling in the test section and one with a floor and without a ceiling. Figure 7.1 shows the experimental setup for both configurations. The primary purpose of testing both configurations was to evaluate the impact of the ceiling on the wind turbine's performance. As was explained in section 2.6, the presence of a ceiling may increase the amount of torque and thrust generated on the turbine compared to the test configuration without a ceiling. Another reason for removing the ceiling was to obtain higher-quality sound measurements using an acoustic camera, as fewer reflective surfaces would minimize the interference of reflecting sound waves. The turbine was fixated on the lower table. The electrical system, connected to the turbine, was located beneath the table. Additionally, a webcam was positioned in front of the display of the electrical load. A live feed was generated of this display to ensure proper functioning during operation. The turbine was controlled outside the wind tunnel using the LabVIEW program. The microphone array for the acoustic measurements was placed at a distance of approximately one meter to ensure it was a far-field measurement.

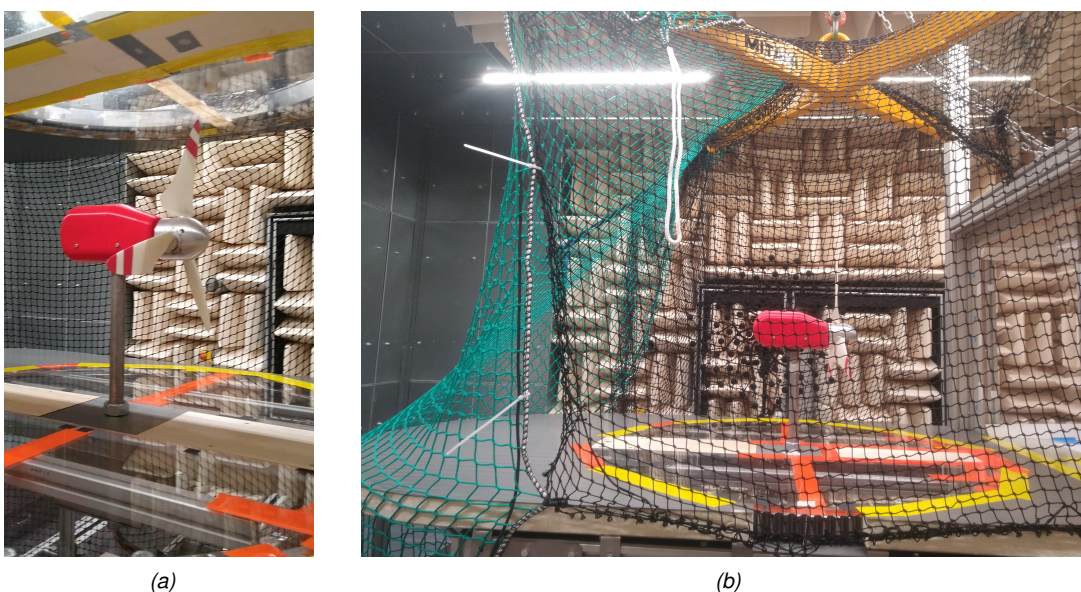


Figure 7.1: Experimental setup with the ceiling (a) and without the ceiling (b)

7.2 Initial findings

This section describes the initial findings of the first measurements of the TwIN-turbine. These findings were as follows:

1. Upon initial measurements, a significant degree of variability was observed in the torque, the thrust, and/or the RPM. The high variation was because certain configurations of the mechanical design were sensitive to high vibration. The placement and orientation of the sensors were slightly adjusted and retested until the variability in the data was minimal. However, this process proved to be time-consuming and resulted in a significant loss of valuable wind tunnel time. Furthermore, the adjustments made to the mechanical design required a new system calibration, resulting in additional time consumption. Mainly the torque sensor required extensive recalibration to ensure proper functioning.
2. The mechanical brake activated at a lower RPM than intended. The brake engaged at approximately 2300 revolutions per minute (RPM) rather than the design target of 3000 RPM. Further investigation revealed that the primary cause of this difference was the increased thickness of the brake linings as described in section 4.1.1. However, the RPM would remain within acceptable parameters even with the thicker linings as long as the wind speed did not exceed 10 meters per second. Maintaining the thicker brake linings increased the system's safety, as the RPM was limited to 2300.
3. Data collection for low Tip Speed Ratios (TSRs) was not feasible as the rotation of the turbine abruptly decreased rapidly upon reaching a TSR of around 3.5. Sometimes the turbine even stopped rotating altogether. It is believed that this can be attributed to separation flow that is created on the blade. When the rotation is decreased, the relative angle of attack at the blade increases. High angles of attack typically indicate the presence of separated flow. Additionally, hysteresis was observed during the measurement. The results would change depending on the history of the measurements done. It was chosen to start with a higher RPM and decrease it systematically until separation flow occurs.

7.3 Statistical analysis

The developed LabVIEW program, as described in section 4.2.4, made it possible to automate the data acquisition along a turbine's characteristic power and thrust curve. Statistical analysis was conducted to determine the optimal settings for the program. Appendix H shows the full statistical analysis. The analysis revealed that the settling time could be established at 5 seconds and the total measurement time at 25 seconds. Additionally, it was found that the thrust measurement's systematic error was notably higher than the systematic error of the torque measurement. This difference may be caused by a lower level of pretension in the thrust sensor than in the torque sensor. The turbine was reinitialized at rest, which means the initial deformation of the load cells would change every time the turbine was started up again. Furthermore, it should be noted that the size of the error would change every time the system was reassembled, which was done multiple times during the experiments.

7.4 Results experiments

This section presents the outcomes of the experimental study. The impact of the ceiling on the turbine's performance is discussed first. Subsequently, the effects of wind speed on the performance are examined. Then, the impact of the blade's pitch angle on the turbine's performance is described. Finally, the results obtained from the microphone array are presented.

7.4.1 Influence of ceiling on performance

This subsection describes the impact of the ceiling on the turbine's performance. As outlined in section 2.6, the presence of a ceiling does cause a certain degree of obstruction in the wake of the TwIN turbine. The impact of the ceiling on the turbine's performance is tested by performing experiments with the presence and absence of the ceiling. Figure 7.1 shows the experimental setup of both configurations. The wind velocity was maintained at 8.5 m/s, and the test was repeated three times to account for the systematic error present in the measurement system. Figure 7.2 presents the thrust coefficient as a function of the TSR for both configurations, and figure 7.3 presents the power coefficient as a function of the TSR for both configurations. Figure 7.2 illustrates that the thrust coefficient for the test section with a ceiling is approximately 15% higher than the test section without a ceiling. The same behavior for the power coefficient can be observed in figure 7.3. A clear distinction can be made despite the size of the systematic error. For future experiments, it would be intriguing to compare the turbine's performance in an experimental setup with and without a floor, to understand the blockage effect of the floor. It should be noted that the QBlade prediction within the graphs corresponds with the numerical results obtained at a pitch angle of -5 degrees. The reason for this is that a manufacturing error is present within the indication of the 0-degree pitch angle orientation of the blade. This is further elaborated in section 7.4.3. It is crucial to understand that the experiments were actually conducted with one of the blades having a pitch angle of -5 degrees rather than the intended angle of 0 degrees.

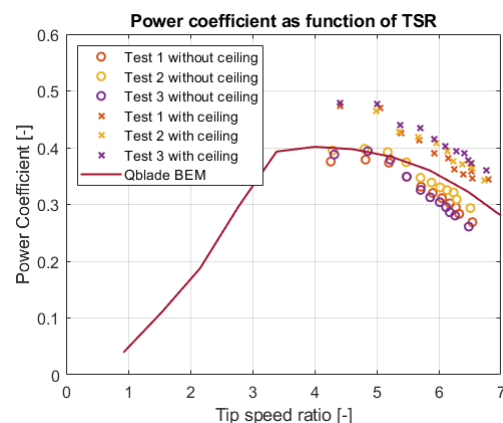
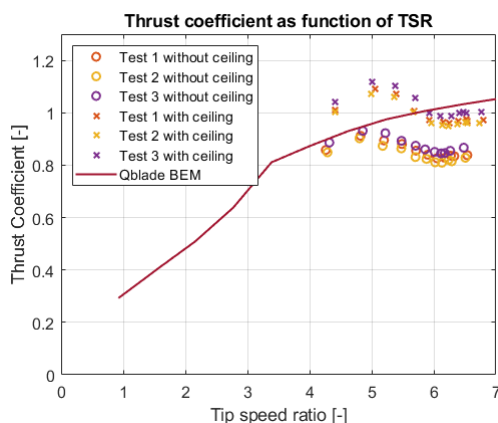


Figure 7.2: Thrust coefficient with and without ceiling

Figure 7.3: Power coefficient with and without ceiling

7.4.2 Influence of wind speed on performance

This subsection explains the wind speed's impact on the TwIN turbine's performance. The experiments were performed for the configuration without a ceiling. Three different wind speeds were tested at 7.5 m/s, 8.5 m/s, and 9.5 m/s. Three separate tests were conducted and averaged for each

wind speed. It was assumed that any systematic error present was random and uncorrelated. The measurements were averaged, which may have reduced the error. However, the systematic error may depend on an unknown quantity. The quantification of the systematic error can be a subject for future research.

Figures 7.4 and 7.5 show the characteristic thrust and power coefficient as a function of the TSR per wind speed. The figures show that the wind velocities of 8.5 and 9.5 m/s follow the same trend, while the wind speed at 7.5 m/s does not. This phenomenon can be attributed to the lower Reynolds number for the blade cross sections. The largest discrepancy can be observed at a TSR of 5. This TSR and a wind speed of 7.5 m/s corresponds to a Reynolds number of approximately 75,000 for the middle part of the blade. Appendix E indicates that the typical airfoil performance at this Reynolds number may be severely impacted, as it falls between the empirical characteristics observed at a Reynolds number of 100,000 (moderately impacted) and 60,000 (significantly impacted). A critical Reynolds may have been passed where the effects of viscosity deteriorated the performance of the airfoil critically. The results show that the wind velocities of 8.5 and 9.5 m/s display a similar trend and have a nearly identical offset. An increase in velocity results in an increase in the Reynolds number. However, the measured values' precision is insufficient to make a correct distinction between the two wind velocities. Additionally, it can be observed that the characteristic thrust and power coefficient are lower than the prediction made by QBlade, except for the power coefficient at a TSR of approximately 4.5. The lower experimental characteristic power and thrust coefficient can be attributed to losses within the system that are not accounted for in the QBlade prediction. On the other hand, the higher experimental characteristic power coefficient around a TSR of 4.5 is surprising. One potential explanation for the excessive power is the presence of the lower floor in the test section which may still block part of the turbine's wake. This obstruction would result in a higher velocity at the blade than predicted by QBlade. It should be noted again that the QBlade prediction within the graphs corresponds with the numerical results obtained at a pitch angle of -5 degrees. It is essential to consider that the experiments were actually performed with one of the blades having a pitch angle of -5 degrees rather than the intended angle of 0 degrees.

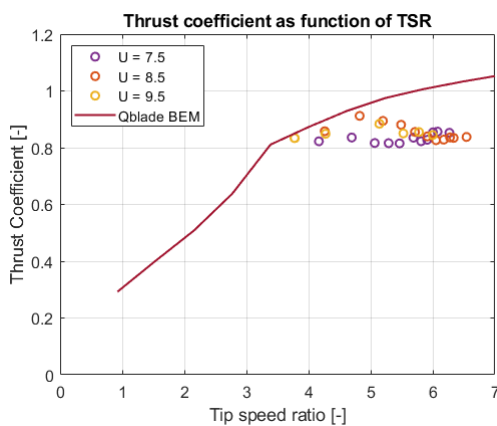


Figure 7.4: Thrust coefficient for various wind speeds

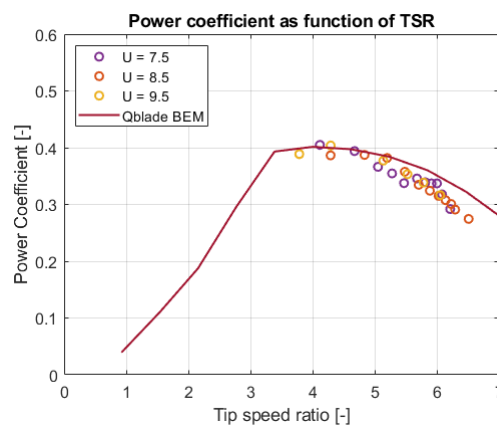


Figure 7.5: Power coefficient for various wind speeds

7.4.3 Influence of pitch angle on performance

This subsection describes the impact of the pitch angle on the TwIN turbine's performance. For this experiment, the pitch angle was adjusted while maintaining a wind speed of 8.5 m/s. The thrust

coefficient as a function of the TSR for various pitch angles is illustrated in figure 7.6, and the power coefficient as a function of the TSR for different pitch angles is shown in figure 7.7. The results can also be presented as a function of the pitch angle for different TSRs. For this, the trends of the thrust coefficient are interpolated with fourth-order polynomials. The power coefficient trends are interpolated with a third-order polynomial, except for a pitch of 0 degrees which is fitted with a fourth-order polynomial. The characteristic power coefficient at a pitch of zero is interpolated with a higher-order polynomial because two points are present that deviate from the characteristic power coefficient curves compared to the other pitch angles. The polynomials are indicated with colored dotted lines in which the color corresponds with the color from the pitch angle. The intersection points of a TSR of 4, 5, and 6 with the polynomials define the data points for the power and thrust coefficient as a function of the pitch angle.

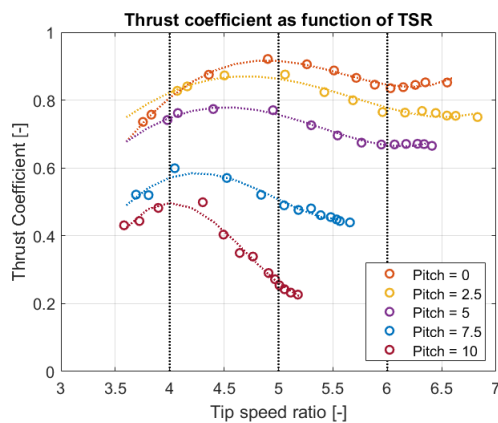


Figure 7.6: Thrust coefficient for various pitch angles, interpolated with polynomials (dotted lines)

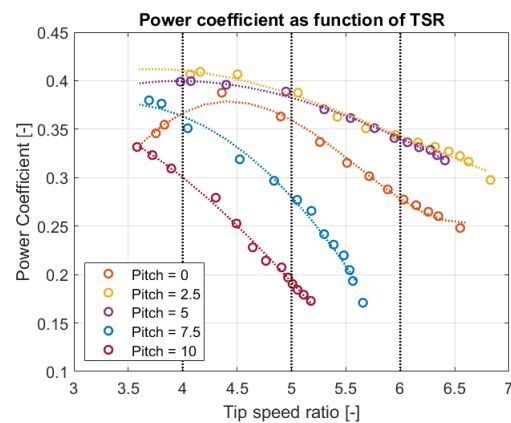


Figure 7.7: Power coefficient for various pitch angles, interpolated with polynomials (dotted lines)

The figures 7.8 and 7.9 present the thrust and power coefficients as a function of the pitch angle for various TSRs. The predictions made by the QBlade software for the different TSRs are also included in the figures. It is noted that the maximum power occurs at a pitch angle between 2.5 and 5 degrees, which contradicts the aerodynamic predictions made in Chapter 5.3.6.

Further investigation revealed that the indication of the pitch angle of 0 degrees on the attached protractor on the hub was wrongly indicated for one of the blades, probably due to a manufacturing error during the design phase of the wind turbine. The indication of the zero pitch angle should have been at an angle of 40 degrees relative to the flat side of the hub but was actually indicated at 35 degrees. This error was discovered after the experiments in the wind tunnel were conducted, meaning that one of the blades had a pitch phase difference of 5 degrees compared to the other two blades during the tests. Appendix J shows the error of the zero pitch angle indication with the protractor.

Figures 7.10 and 7.11 present the results when a pitch phase shift of -5 degrees is applied to the experimental data. The application of this phase shift to the experimental data reveals that the experimental results have the same trend as the QBlade predictions, with primarily an offset difference. The experimental power coefficient is lower than the QBlade prediction, as expected, due to the absence of losses that are not included in the QBlade prediction. The experimental thrust coefficient shows some values higher than the QBlade prediction, which is believed to be due to the floor within the test section obstructing part of the wake of the turbine.

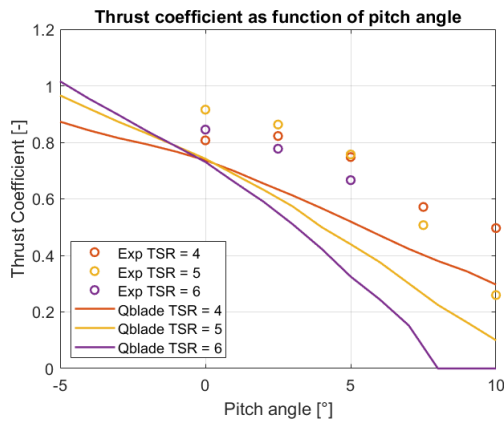


Figure 7.8: Thrust coefficient for various TSR

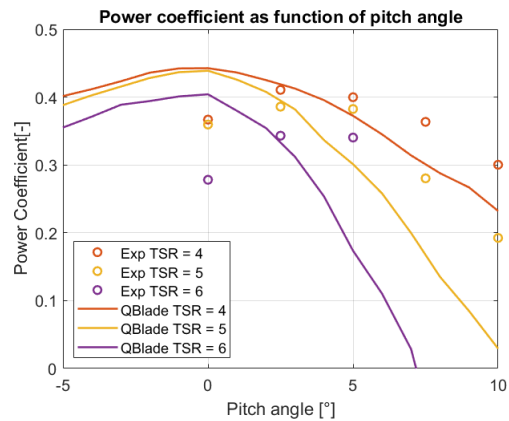


Figure 7.9: Power coefficient for various TSR

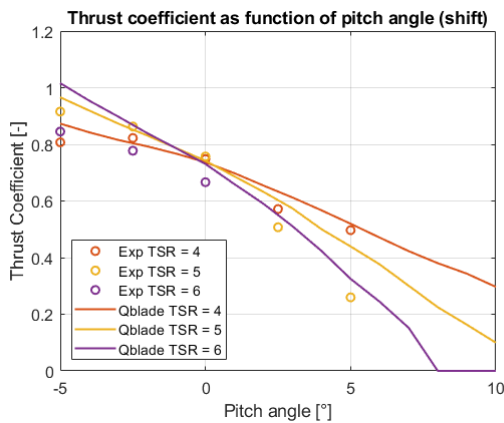


Figure 7.10: Thrust coefficient for various TSR (shifted)

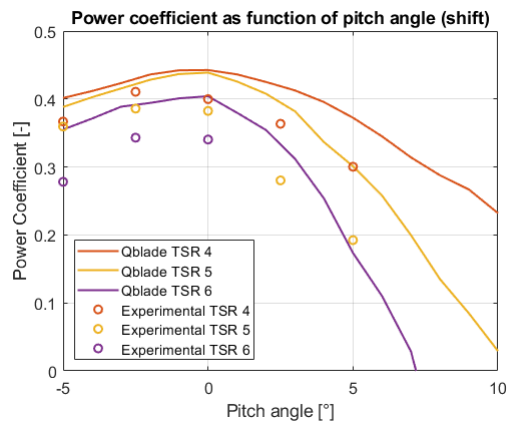


Figure 7.11: Power coefficient for various TSR (shifted)

Figures 7.12 and 7.13 present the pitch-shifted experimental results as a function of the TSR. These results are compared to the numerical predictions obtained in section 5.3.5. The dotted line represents the numerical predictions and is depicted in the same color as the experimental data obtained at that specific pitch angle.

From figure 7.12 it is observed that the thrust coefficient trends from the experimental results slightly differ from those predicted by QBlade. The difference between the experimental and numerical results seems to differ more when the RPM of the turbine increases. It is expected that this is because of the wrong zero pitch angle indication of the protractor of blade three.

Figure 7.13 shows the power coefficient as a function of the tip speed ratio. The experimental power coefficients show a similar trend as the numerical QBlade predictions, with only an offset difference. The offset is consistent for all measurements except for the measurement obtained at a pitch of 2.5 degrees. A high systematic and standard error was observed in this measurement, which may have occurred through a reassembly of the turbine. As such, the measurement at a pitch of 2.5 degrees may not be entirely reliable. The offset difference between the experimental and numerical predictions within the other measurements may be due to losses not accounted for in the QBlade model. One of these losses is the created misalignment of the rotor due to one of the blades having

a 5-degree phase difference in comparison to the other two blades.

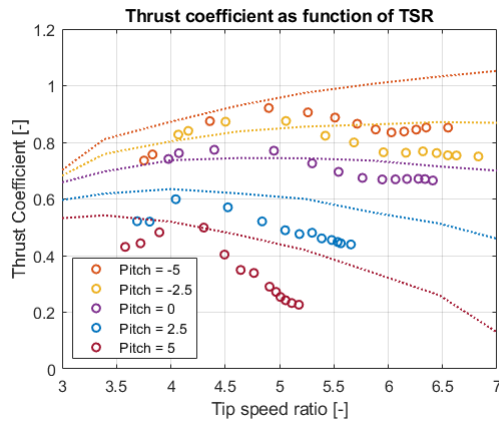


Figure 7.12: Thrust coefficient for various TSR (shifted), compared to QBlade predictions (dotted lines)

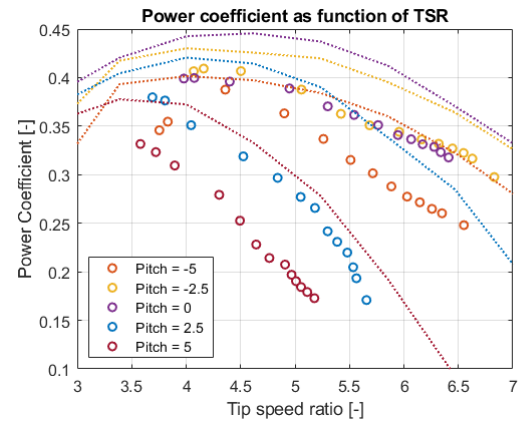


Figure 7.13: Power coefficient for various TSR (shifted), compared to QBlade predictions (dotted lines)

7.4.4 Results smoke machine

The creation of vortices at the blade's tip was analyzed by inserting smoke in the incoming flow from the wind tunnel. A camera was used to make a slow-motion video of the vortex creation. Figure 7.14 shows a frame from that video where it can be clearly seen vortices were created at the blade's tip. The vortices extended far into the wake of the wind turbine. Vortex creation decreases the performance of a turbine, as described in section 5.3.3. It may be beneficial to analyze the blades using an alternative tool within QBlade, such as the lifting line method. The lifting line method assumes that a series of vortices along the span can predict the aerodynamic forces on the blade [36]. This method provides a more precise correction of the reduction in performance due to vortex creation compared to the BEM method.



Figure 7.14: Tip vortex creating observed from smoke inserted into wind

7.4.5 Results microphone array

This subsection presents the results obtained from the microphone array. The measurements were conducted for a wind speed of 8.5 m/s and a rotational speed of 2200 RPM for the rotor. These measurements were conducted only for the open configuration setup because the ceiling was expected to generate unwanted sound reflection. It was observed that the power spectrum did not vary significantly over time, making it possible to analyze the power spectrum of a single microphone at an arbitrary time instant. The power spectrum of one microphone is shown in Figure 7.15. Three prominent peaks are visible within this graph.

Section A of the power spectrum illustrates the highest peak, located at the lower frequencies. A beam pattern at these frequencies was generated using the beamforming algorithm. The acoustic image for the lower frequencies is shown in figure 7.16. Design imperfections in the gear transmission primarily generate this noise. These imperfections tend to increase in size as the turbine is utilized more frequently, thus amplifying the noise.

Section B of the power spectrum shows the peak in the power spectrum that corresponds to the noise produced by the generator. Figure 7.17 shows the corresponding acoustic image coming from the generator.

Section C of the power spectrum may indicate aerodynamic noise at high frequencies. Figure 7.18 shows the acoustic image of the aerodynamic noise. Various aerodynamic phenomena may generate aerodynamic noise. Two peaks of equal amplitude can be observed. The peak located in the middle of the figure may be caused by the aerodynamic self-noise at the trailing edge of the blades, which corresponds with the empirical results from Oerlemans [7] described in section 2.5. The peak located at the lower point may be a result of the same noise coming from the trailing edge of the blades, only now reflected via the table. The interaction between the shear layer and the blades or the flow between the tower and the blades may also cause this noise.

It can be concluded that the gears and the generator generate most of the noise. Aerodynamic noise produced by the turbine is analyzed for higher frequencies. Aerodynamic noise at lower frequencies may be present but is completely overshadowed by the noise of the gears and the generator. For detailed aeroacoustic measurements, it is necessary to reduce the noise generated by the gears and generator to analyze the aerodynamic noise at lower frequencies. It may also be necessary to remove the lower table to eliminate sound reflection.

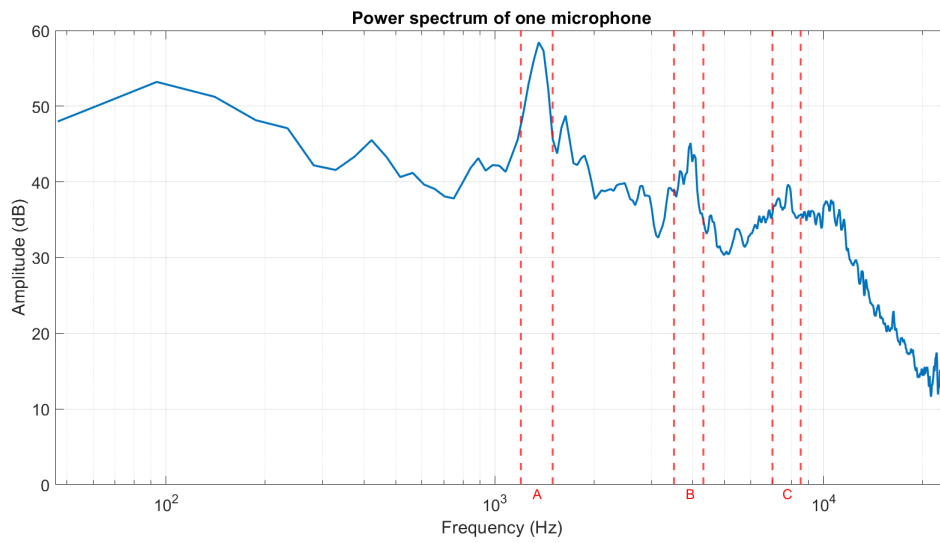


Figure 7.15: Power spectrum of one microphone

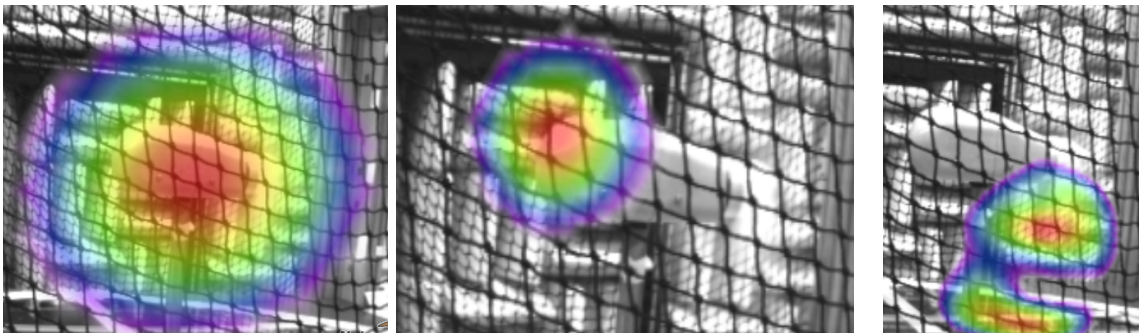


Figure 7.16: Noise of gears
(A)

Figure 7.17: Noise of generator
(B)

Figure 7.18: Aerodynamic noise
(C)

Conclusions and recommendations

8.1 Conclusions

In this thesis, the TwIN turbine's design was modified and evaluated for its performance under various conditions within the university's wind tunnel. The electrical design was modified by substituting the existing electrical load with a programmable external electronic load. The electronic load was connected to a computer and controlled by a LabVIEW program. The Arduino was connected to the computer, allowing the simultaneous collection and storage of data from the Arduino and the electronic load. The TwIN turbine performed well in the wind tunnel, although the Arduino, used as a data acquisition system for the torque, thrust, and rotational speed, was identified as the biggest bottleneck in the design. The Arduino functioned adequately, but only for a low sample rating. Additionally, a significant amount of time was spent adjusting the mechanical system to minimize deviations in the measurements taken by the torque load cell, thrust load cell, and magnetic encoder.

The impact of the ceiling in the test section on the performance of the TwIN turbine was evaluated by comparing the performance with and without a ceiling. Results showed that a ceiling increased the power and thrust of the TwIN turbine by approximately 15 %. For future research, it may be beneficial to compare the turbine's performance within a test section with only a floor and a free jet test section.

The impact of the wind velocity on the performance was evaluated by comparing three different wind velocities (7.5, 8.5, and 9.5 m/s). Higher velocities could not be reached due to the rotational speed limit of the centrifugal break. Results showed a high deviation and systematic error of the thrust and torque for a wind speed of 7.5 m/s. This deviation was possibly due to the low Reynolds number airfoil degradation. No significant differences were observed between 8.5 and 9.5 m/s wind velocities. The difference between the velocities was too small to make a clear distinction.

The impact of the pitch angle was evaluated by comparing five different pitch angles (0, 2.5, 5, 7.5, and 10 degrees). Results revealed a pitch phase difference of 5 degrees between the experimental results and the QBlade prediction. This phase shift was attributed to a manufacturing mistake during the development phase of the turbine. Further research may include an aerodynamic analysis using the lifting line module within QBlade to improve aerodynamic performance prediction.

The aeroacoustic performance of the TwIN turbine was evaluated by performing an aeroacoustic analysis. A microphone array was used to measure the sound pressure along the time. The sound sources were localized with a beam-forming algorithm. The results showed that the gears and the

generator produced the most noise within the turbine. These sound sources were present at the lower frequencies of the power spectrum and overshadowed any aerodynamic sound sources present at these frequencies. Aerodynamic noise was identified at higher frequencies, but no clear aerodynamic phenomena could be linked to the results found. For a comprehensive aeroacoustic analysis, it is necessary to reduce the noise generated by the gears and the generator to analyze the aerodynamic noise at lower frequencies. Furthermore, removing the floor within the test section may be necessary to eliminate reflection. Also, increasing the distance between the rotor and the tower may be advantageous to eliminate the possibility of sound production due to flow interaction between the tower and the turbine's rotor.

8.2 Recommendations

The design of the TwIN turbine was developed on a limited budget. However, should additional funding become available, it is recommended to manufacture a completely new design of a small-scale wind turbine. The main limitations of the current design identified in this report can be used as a starting point for future development. The following recommendations are proposed for developing a higher-quality small-scale wind turbine.

Mechanical design

To improve the mechanical design, the integration of a Maxon planetary gearbox is recommended. This type of gearbox, also known as an epicyclic gearbox, consists of multiple gears arranged such that the input and output shafts are aligned. This improved alignment would increase the turbine's performance and decrease wear on the gears. Additionally, planetary gearboxes have a certain degree of self-alignment, making them less sensitive to installation errors. A better alignment also produces less sound from the gears, making the turbine more suitable for aeroacoustic measurements.

Electrical design

The electrical design of the turbine can be improved by replacing the Arduino with a plug-and-play data acquisition (DAQ) system from National Instruments. The DAQ system is more powerful and capable of high-resolution and high-accuracy measurements. The DAQ system is also compatible with the already-developed LabVIEW program. Furthermore, significant time was lost in tuning the mechanical system to avoid high oscillations of the sensors and a high system error. These errors can be reduced by integrating a rotary torque sensor, which eliminates a lot of intermediate couples between the rotor and the sensor. Another option is to incorporate a larger generator with a lower generator constant, allowing the rotor to be directly attached to the generator without a gear transmission. This would result in less energy loss and better alignment between parts.

LabVIEW program

The LabVIEW program can be further developed by fixing the compatibility issues with the wind tunnel LabVIEW program. The integration of the wind tunnel program makes it possible to gather data from the wind tunnel, the turbine, and the electronic load simultaneously. A characteristic power and thrust coefficient curve can be added to the display of the gathered data, making it easy to check whether the data follows the expected trend. If a new wind turbine is developed, this LabVIEW program can be used as starting point for communicating with the different measurement devices. Additionally, one can program the electronic load to control the rotation of the turbine by voltage instead of resistance or control the amount of current drawn from the generator.

Aerodynamic analysis

The blade element momentum module in QBlade was used to predict the TwIN turbine's performance. However, the lifting line module within QBlade can be used for a more accurate prediction. This theory considers three-dimensional effects that are not accounted for within the blade element momentum theory. It is recommended to conduct the aerodynamic performance prediction using the lifting line module within QBlade and compare it with the existing BEM results.

Future experiments with TwIN turbine

It is recommended to attach new protractors on the hub to give a correct indication of a zero pitch angle. Furthermore, it is recommended that, if experiments are performed with the TwIN turbine again, a logarithmic scaling for the electrical resistances in LabVIEW is used. A logarithmic scaling results in more points gathered at low electrical resistances than at high electrical resistances. This will result in a more evenly distributed data set along the characteristic power and thrust curve of the TwIN turbine, with more points for the low TSR regime than for the high TSR regime. Furthermore, for the purpose of conducting an aeroacoustic analysis, it may be necessary to first evaluate the power spectrum for a non-rotating small-scale wind turbine within the wind tunnel and compare it to a rotating turbine within the wind tunnel. This comparison will enable a clear distinction between the wind tunnel's sound generation and the sound generated by the TwIN turbine. The beam-forming algorithm can be applied to the frequencies where the power spectrums differentiates from each other.

Bibliography

- [1] C. F. C. van Wijk, "Design of a small-scale wind turbine rotor and hub for wind tunnel testing," Master's thesis, University of Twente, 2020. [Online]. Available: <http://essay.utwente.nl/81624/>
- [2] R. F. O. van Wijk, "Design of a small wind turbine nacelle and tower for wind tunnel testing," Master's thesis, University of Twente, 2020. [Online]. Available: <http://essay.utwente.nl/81663/>
- [3] J. Olde, N. Wsterhof, and L. B. Bolivar, "Noise reduction on a small scale wind turbine using trailing edge serrations," 2022.
- [4] J. F. Manwell, J. G. MCGowan, and A. Rogers, *Wind Energy Explained, theory, design and application*. Wiley, 2009, ISBN: 978-0-470-01500-1.
- [5] K. Gemba, "Measurement of boundary layer on a flat plate," 2007. [Online]. Available: <https://web.iitd.ac.in/~pmvs/courses/me1705/boundarylayer.pdf>
- [6] J. Winslow, H. Otsuka, B. Govindarajan, and I. Chopra, *Basic Understanding of Airfoil Characteristics at Low Reynolds Numbers*, 2018. [Online]. Available: <https://doi.org/10.2514/1.C034415>
- [7] S. Oerlemansa, P. Sijtsmaa, and B. M. López, "Location and quantification of noise sources on a wind turbine," *Journal of Sound and Vibration*, vol. 299, pp. 869–883, 2006. [Online]. Available: <https://doi.org/10.1016/j.jsv.2006.07.032>
- [8] S. Oerlemans, "Wind turbine noise: primary noise sources," *Wind turbine noise*, 2011. [Online]. Available: <https://reports.nlr.nl/server/api/core/bitstreams/9de8dfe0-5ab7-4c3e-ae9-1e0dfdbce766/content>
- [9] I. Romero-Sanz and Álvaro Matesanz, "Noise management on modern wind turbines," *Wind Engineering*, vol. 32, 2008. [Online]. Available: <https://doi-org.ezproxy2.utwente.nl/10.1260/030952408784305886>
- [10] J. Ryi, W. Rhee, U. C. Hwang, and J.-S. Choi, "Blockage effect correction for a scaled wind turbine rotor by using wind tunnel test data," *Renewable Energy*, vol. 79, pp. 227–235, 2014. [Online]. Available: <http://dx.doi.org/10.1016/j.renene.2014.11.057>
- [11] L. de Santana, M. P. J. Sanders, and C. H. Venner, "The utwente aeroacoustic wind tunnel upgrade," 2018. [Online]. Available: <https://doi.org/10.2514/6.2018-3136>
- [12] S. Eckert, A. Cramer, and G. Gerbeth, "Velocity measurement techniques for liquid metal flows," 2007. [Online]. Available: https://link.springer.com/chapter/10.1007/978-1-4020-4833-3_17
- [13] instrumentationtoolbox.com, "Temperature measurements with thermocouples," <https://www.instrumentationtoolbox.com/2011/01/sensors-used-in-industrial.html>, 2022.

- [14] Engineering.org, "Brushless dc motor, how it works?" 2013. [Online]. Available: <https://www.lesics.com/brushless-dc-motor.html>
- [15] D. M. Ștefănescu, "Strain gauges and wheatstone bridges basic instrumentation and new application for electrical measurement of non-electrical quantities," 2011. [Online]. Available: <https://doi.org/10.1109/SSD.2011.5767428>
- [16] A. Hylkema, W. Eppink, and L. Castelucci, "Determining the performance of a small wind turbine using experimental methods and validation of existing results," 2022.
- [17] N. Instruments, "Ni tdms file format - what is a tdms file?" 2022. [Online]. Available: <https://www.ni.com/nl-nl/support/documentation/supplemental/06/the-ni-tdms-file-format.html>
- [18] W. T. Cochran, J. W. Cooley, D. L. Favin, H. D. Helms, R. A. Kaenel, W. W. Lang, G. C. Maling, D. E. Nelson, C. M. Rader, and P. D. Welch, "What is the fast fourier transform?" 1967. [Online]. Available: <https://ieeexplore.ieee.org/stamp/stamp.jsp?tp=&arnumber=1447887>
- [19] K. K. Parhi and M. Ayinala, "Low-complexity welch power spectral density computation," 2014. [Online]. Available: <https://ieeexplore.ieee.org/stamp/stamp.jsp?tp=&arnumber=6525419>
- [20] J. Grythe, "Beamforming algorithms - beamformers," 2014. [Online]. Available: <https://web2.norsonic.com/wp-content/uploads/2016/10/TN-beamformers.pdf>
- [21] *Datasheet Bionic M-112 Array*, CAE systems, 2017. [Online]. Available: <https://www.cae-systems.de/fileadmin/CAEpage/Datenblaetter/datasheet-acoustic-camera-bionic-m-112.pdf>
- [22] P. Malcovati and A. Baschiroto, "The evolution of integrated interfaces for mems microphones," 2018. [Online]. Available: https://www.researchgate.net/figure/Basic-structure-and-working-principle-of-a-MEMS-microphone_fig2_326006102
- [23] *User's guide DL3000 Series Programmable DC Electronic Load*, Rigol Technologies INC, 2017. [Online]. Available: https://www.batronix.com/files/Rigol/Elektronische-Lasten/DL3000/DL3000_UserGuide_EN.pdf
- [24] M. S. Selig, J. J. Guglielmo, A. P. Broeren, and P. Giguere, "Summary of low-speed airfoil data," 1995. [Online]. Available: https://m-selig.ae.illinois.edu/uiuc_lsat/Low-Speed-Airfoil-Data-V3.pdf
- [25] "Qblade guidelines," 2013. [Online]. Available: <https://doi.org/10.13140/RG.2.1.3819.8882>
- [26] B. Montgomerie, "Methods for root effects, tip effects and extending the angle of attack range to ± 180 , with application to aerodynamics for blades on wind turbines and propellers," 2005. [Online]. Available: <https://www.foi.se/rest-api/report/FOI-R--1305--SE>
- [27] L. A. Viterna and R. D. Corrigan, "Fixed pitch rotor performance of large horizontal axis wind turbines," 1982. [Online]. Available: <https://ntrs.nasa.gov/citations/19830010962>
- [28] H. Glauert, *Airplane Propellers*, 1935. [Online]. Available: http://dx.doi.org/10.1007/978-3-642-91487-4_3
- [29] W. Z. Shen, R. Mikkelsen, J. N. Sørensen, and C. Bak, *Tip loss corrections for wind turbine computations*, 2005. [Online]. Available: <https://doi.org/10.1002/we.153>

- [30] H. Snel, R. Houwink, and W. Piers, "Sectional prediction of 3d effects for separated flow on rotating blades," 1992. [Online]. Available: <https://ntrl.ntis.gov/NTRL/dashboard/searchResults/titleDetail/PB94201696.xhtml>
- [31] J. Hernández and A. Crespo, "Aerodynamic calculation of the performance of horizontal axis wind turbines and comparison with experimental results," *Wind Engineering*, 1987. [Online]. Available: <https://www.jstor.org/stable/43749310>
- [32] *Datasheet testo 470*, Testo, 2022. [Online]. Available: <https://static-int.testo.com/media/7b/6f/0c87d1dc9f9a/testo-470-Data-sheet.pdf>
- [33] U. Kafader, "maxon motors as generators," 2022. [Online]. Available: <https://support.maxongroup.com/hc/en-us/articles/360004496254-maxon-Motors-as-Generators>
- [34] *Multi Axis Disc Motor X 3508 390KV High Efficiency Multiaxis Motor for TF680*, Thanksbuyer, 2022. [Online]. Available: <https://www.thanksbuyer.com/multi-axis-disc-motor-x-3508-390kv-high-efficiency-multiaxis-motor-for-tf680-31629>
- [35] *Dataheet SQL100A full bridge rectifier*, Guerte, 2019.
- [36] A. van Garrel, "Development of a wind turbine aerodynamics simulation module," 2003.
- [37] —, "Wind turbine aerodynamics," 2021.
- [38] Y. E. khchineam and M. Sritib, "Tip loss factor effects on aerodynamic performances of horizontal axis wind turbine," *Energy Procedia*, vol. 118, 2017. [Online]. Available: <https://doi.org/10.1016/j.egypro.2017.07.028>
- [39] G. R. Pirrung and M. P. van der Laan, "A simple improvement of a tip loss model for actuator disc and actuator line simulations," *Wind Energy*, 2018. [Online]. Available: <https://doi.org/10.5194/wes-2018-59>
- [40] C. Bak, J. Johansen, and P. B. Andersen, "Three-dimensional corrections of airfoil characteristics based on pressure distributions," 2006. [Online]. Available: https://www.researchgate.net/publication/237435464_Three-Dimensional_Corrections_of_Airfoil_Characteristics_Based_on_Pressure_Distributions
- [41] thanksbuyer.com, "Datasheet multi axis disc motor x 3508 390kv high efficiency multiaxis motor for tf680," 2023. [Online]. Available: <https://www.thanksbuyer.com/multi-axis-disc-motor-x-3508-390kv-high-efficiency-multiaxis-motor-for-tf680-31629>
- [42] Guerte, "Datasheet three-phase bridge rectifier sql100a1200v," 2017. [Online]. Available: <https://www.rcscomponents.kiev.ua/datasheets/sql100-12specification.pdf>

Blade Element Momentum theory

A.1 Betz limit and one-dimensional momentum

A simple model from Betz (1926) is used to determine the power for an ideal turbine rotor. This model makes use of a control volume around the rotor which can be seen in figure A.1.

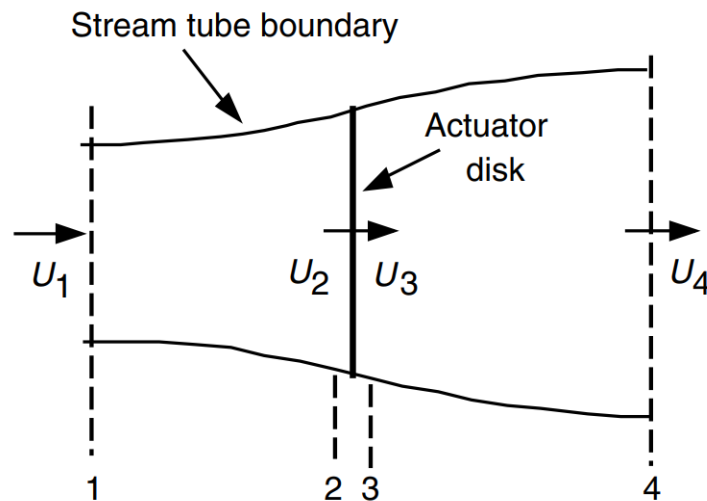


Figure A.1: Control volume around rotor [4]

One can apply the conservation of linear momentum on the control volume. Here the difference in mass flow times velocity determines the thrust force of the rotor. For steady-state flow this means the thrust can be defined as follows:

$$T = \dot{m}(U_1 - U_4) \quad (\text{A.1})$$

In both control volumes on either side of the actuator disk it can be seen no work is done which means Bernoulli's equation can be applied on either side:

$$p_1 + \frac{1}{2}\rho U_1^2 = p_2 + \frac{1}{2}\rho U_2^2 \quad (\text{A.2})$$

$$p_3 + \frac{1}{2}\rho U_3^2 = p_4 + \frac{1}{2}\rho U_4^2 \quad (\text{A.3})$$

Furthermore, it can be assumed that far downstream pressure and far upstream pressure are equal ($p_1=p_4$) and the velocity across the rotor disk is also equal ($U_2=U_3$).

The sum of the forces before and after the actuator obtains another expression for the thrust of the actuator disc:

$$T = A_2(p_2 - p_3) \quad (\text{A.4})$$

If equations A.2 and A.3 are substituted into equation A.4 the expression becomes:

$$T = \frac{1}{2}\rho A_2(U_1^2 - U_4^2) \quad (\text{A.5})$$

The equations A.1 and A.5 are substituted into each other by the equation the thrust. This ultimately obtains an expression for U_2 as a function of the velocities on the far field boundaries:

$$U_2 = \frac{U_1 + U_4}{2} \quad (\text{A.6})$$

Now an induction factor (a) is introduced which is the fractional decrease of the wind velocity between the incoming stream and the actuator disc. The expression is thus as follows:

$$a = \frac{U_1 - U_2}{U_1} \quad (\text{A.7})$$

Which means:

$$U_2 = U_1(1 - a) \quad (\text{A.8})$$

And:

$$U_4 = U_1(1 - 2a) \quad (\text{A.9})$$

The power of the disc can be determined by multiplying the thrust equation (equation A.5) with the velocity of the actuator disc:

$$P = \frac{1}{2}\rho A_2(U_1^2 - U_4^2)U_2 = \frac{1}{2}\rho A_2U_2(U_1 + U_4)(U_1 - U_4) \quad (\text{A.10})$$

The equations A.8 and A.9 are substituted into equation A.11 which obtains:

$$P = \frac{1}{2}\rho A_2U_1^34a(1 - a)^2 \quad (\text{A.11})$$

The power is characterized by the power coefficient which is defined as:

$$C_P = \frac{P}{\frac{1}{2}\rho U_1^3 A_2} \quad (\text{A.12})$$

Equation A.11 is substituted into equation A.12 which obtains:

$$C_P = 4a(1 - a)^2 \quad (\text{A.13})$$

The maximum energy extraction for a given wind speed can be found by taking the derivative over a for equation A.13:

$$\frac{dC_P}{da} = 0; \quad (1 - a)^2 - 2a(1 - a) = 0 \rightarrow a = \frac{1}{3} \quad (\text{A.14})$$

The obtained induction factor is now substituted into equation A.13 that obtains the Betz limit which is the maximum power that can be extracted from the wind:

$$C_{P_{max}} = \frac{16}{27} \quad (\text{A.15})$$

The axial thrust can now be determined by substituting equations A.8 and A.9 into equation A.5:

$$T = \frac{1}{2}\rho AU^2(4a(1 - a)) \quad (\text{A.16})$$

A.2 Momentum theory with wake rotation

The analysis in the previous section does not take into account the rotation that is created by the blades on the flow. This phenomenon results in less energy extraction from the wind and should be included in the analysis. A new control volume is set up which can be seen in figure A.2. This control volume is modeled such that it rotates with the same angular velocity as the blades. It is assumed that the annular velocity (ω) created by the blades on the flow is small compared to the annular velocity of the wind turbine rotor (Ω). This eventually means the pressure in the free stream can be set equal to the pressure of the far wake stream.

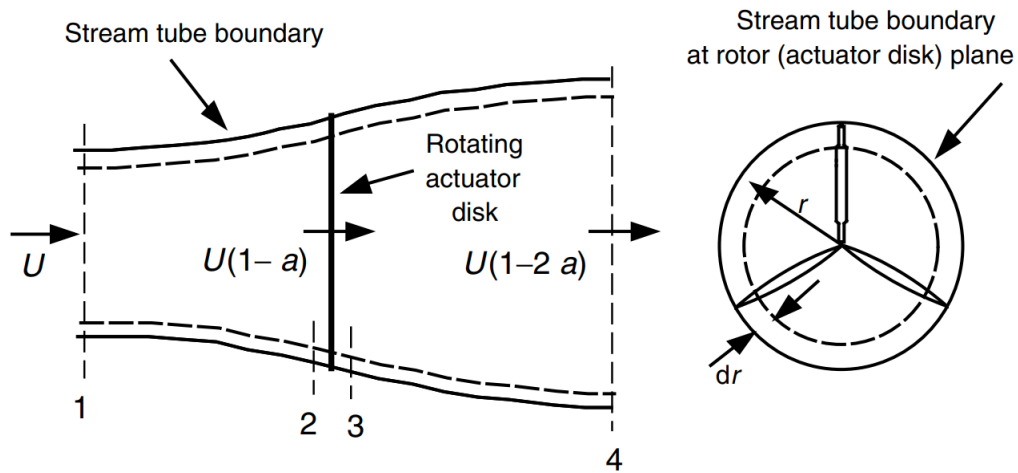


Figure A.2: Control volume around rotor [4]

With the use of Bernoulli's equation, an equation can be set up to find the pressure difference before and after the rotating actuator disk. The annular velocity of the air increases from Ω to $\Omega + \omega$ while the axial velocity remains constant. This equation then becomes as follows:

$$p_2 + \frac{1}{2}\rho(\Omega r)^2 = p_3 + \frac{1}{2}\rho((\Omega + \omega)r)^2 \quad (\text{A.17})$$

The pressure difference then becomes as follows:

$$p_2 - p_3 = \rho\left(\Omega + \frac{1}{2}\omega\right)\omega r^2 \quad (\text{A.18})$$

The thrust can be determined by multiplying the pressure difference with the area of the rotor ($dA = 2\pi r dr$):

$$dT = (p_2 - p_3)dA = \rho\left(\Omega + \frac{1}{2}\omega\right)\omega r^2 2\pi r dr \quad (\text{A.19})$$

An annular induction factor (a') is defined which is as follows:

$$a' = \frac{\omega}{2\Omega} \quad (\text{A.20})$$

If equation A.20 is substituted into equation A.19 the equation becomes:

$$dT = 4a'(1 + a')\frac{1}{2}\rho\Omega^2 r^2 2\pi r dr \quad (\text{A.21})$$

From the linear momentum analysis, a thrust was determined in relation to the axial induction factor (a):

$$dT = 4a(1 - a)\frac{1}{2}U^2 2\pi r dr \quad (\text{A.22})$$

The two thrust equations are equated to each other which gives:

$$\frac{a(1-a)}{a'(1+a')} = \frac{\Omega^2 r^2}{U^2} = \lambda_r^2 \quad (\text{A.23})$$

Here λ_r is the local speed ratio which is dependent on r . The tip speed ratio (λ) is defined as the ratio between the blade speed tip and the wind speed:

$$\lambda = \frac{\Omega R}{U} \quad (\text{A.24})$$

Furthermore, an expression for torque can be defined by applying the conservation of angular momentum. Here the torque is set equal to the change in angular momentum of the wake. The expression for an incremental annular area then becomes (note: $U_2 = U(1-a)$ and $a' = \omega/2\Omega$):

$$dQ = d\dot{m}(\omega r)(r) = (\rho U_2 2\pi r dr)(\omega r)(r) = 4a'(1-a')\frac{1}{2}\rho U \Omega r^2 2\pi r dr \quad (\text{A.25})$$

This means the total torque can be defined as:

$$Q = \frac{1}{2}\rho A R U^2 4a'(1-a)\lambda \quad (\text{A.26})$$

A.3 Blade element theory

The blade element theory considers the forces of the wind turbine as a function of the angle of attack and the lift and drag coefficients. Within this theory, a blade is divided into N elements each with a length of dr . The lift force is perpendicular to the relative wind while the drag force is parallel. The relative wind consists of the wind velocity due to the rotation of the blade and the wind velocity at the rotor. The rotational component includes the induced angular velocity and the blade section velocity. This results in the following expression:

$$\Omega r + (\omega/2)r = \Omega r + \Omega a' r = \Omega r(1+a') \quad (\text{A.27})$$

Within this theory, different parameters are defined. These are θ_p which is the section pitch angle, θ_T which is the blade twist angle, α which is the angle of attack, $\Phi = \theta_p + \alpha$ which is the angle of the relative wind, U_{rel} which is the relative wind velocity, dL which is the incremental lift force, dD which is the incremental drag force, dF_N which is the incremental normal force. and dF_T which is the incremental tangential force. These parameters can be found in figure A.3.

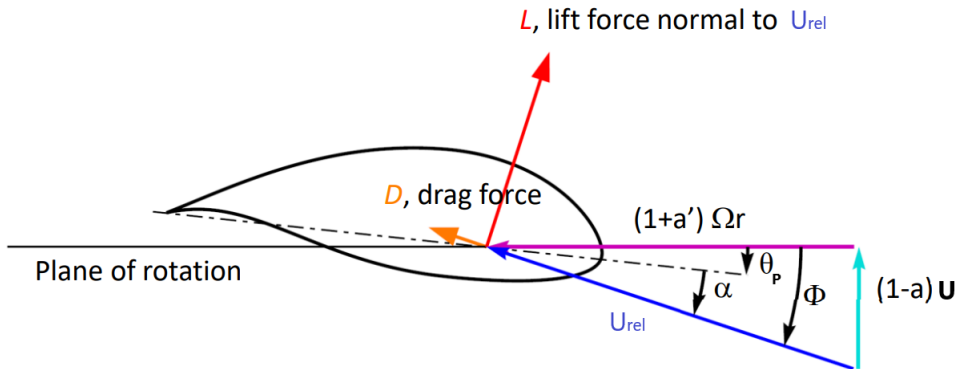


Figure A.3: Blade geometry with variables [37]

The following expressions can be set up with use of figure A.3:

$$\tan\Phi = \frac{U(1-a)}{\Omega r(1-a')} = \frac{1-a}{(1+a')\lambda_r} \quad (\text{A.28})$$

$$U_{rel} = \frac{U(1-a)}{\sin\Phi} \quad (\text{A.29})$$

$$dL = C_L \frac{1}{2} \rho U_{rel}^2 c dr \quad (\text{A.30})$$

$$dD = C_D \frac{1}{2} \rho U_{rel}^2 c dr \quad (\text{A.31})$$

$$dF_N = dL \cos\Phi + dD \sin\Phi \quad (\text{A.32})$$

$$dF_T = dL \sin\Phi - dD \cos\Phi \quad (\text{A.33})$$

The total normal force on the section from a distance r then becomes:

$$dF_N = B \frac{1}{2} \rho U_{rel}^2 (C_L \cos\Phi + C_D \sin\Phi) c dr \quad (\text{A.34})$$

Here B represents the number of blades. The differential torque on the section from a distance r then becomes:

$$dQ = B \frac{1}{2} \rho U_{rel}^2 (C_L \sin\Phi - C_D \cos\Phi) c r dr \quad (\text{A.35})$$

A.4 Corrections in blade element momentum theory

Both the momentum theory and blade element theory are combined into the blade element momentum theory to predict the torque and thrust of a wind turbine. For a detailed explanation of the combination, it is referred to the book "Wind Energy Explained" [4]. This section explains how correction factors affect the calculation for the axial and the tangential induction factor.

Classical BEM theory

The first equation introduced is the local solidity:

$$\sigma' = \frac{Bc}{2\pi r} \quad (\text{A.36})$$

The axial induction factor is determined as follows:

$$a = \frac{1}{\frac{4\sin^2(\Phi)}{\sigma'(C_L \cos(\Phi) + C_D \sin(\Phi))} + 1} \quad (\text{A.37})$$

The tangential induction factor is determined as follows:

$$a' = \frac{1}{\frac{4\sin(\Phi)\cos(\Phi)}{\sigma'(C_L \sin(\Phi) - C_D \cos(\Phi))} - 1} \quad (\text{A.38})$$

Prandtl's tip and root losses

The Prandtl's tip and root losses are defined as follows [38]:

$$F_{Pr,tip}(r) = \frac{2}{\pi} \arccos\left(\exp\left(\frac{-B(R-r)}{2r\sin(\Phi)}\right)\right) \quad (\text{A.39})$$

$$F_{Pr,root}(r) = \frac{2}{\pi} \arccos\left(\exp\left(\frac{-B(r-r_{root})}{2r\sin(\Phi)}\right)\right) \quad (\text{A.40})$$

The axial and tangential induction factor then becomes:

$$a = \frac{1}{\frac{4F_{Pr,tip}F_{Pr,hub} \sin^2(\Phi)}{\sigma'(C_L \cos(\Phi) + C_D \sin(\Phi))} + 1} \quad (\text{A.41})$$

$$a' = \frac{1}{\frac{4F_{Pr,tip}F_{Pr,hub} \sin(\Phi)\cos(\Phi)}{\sigma'(C_L \sin(\Phi) - C_D \cos(\Phi))} - 1} \quad (\text{A.42})$$

New tip and root losses

The new tip and root losses are defined as follows [39]:

$$F_{Sh,tip}(r) = \frac{2}{\pi} \arccos \left(\exp - g_s \frac{-B(R-r)}{2r \sin(\Phi)} \right) \quad (\text{A.43})$$

$$F_{Sh,root}(r) = \frac{2}{\pi} \arccos \left(\exp - g_s \frac{-B(r-r_{root})}{2r \sin(\Phi)} \right) \quad (\text{A.44})$$

Where

$$g_s = \exp(-0.125((B\lambda - 21)) + 0.1) \quad (\text{A.45})$$

The axial and tangential induction factor then becomes:

$$a = \frac{1}{\frac{4F_{Pr,tip}F_{Pr,hub} \sin^2(\Phi)}{\sigma'F_{Sh,tip}F_{Sh,root}(C_L \cos(\Phi) + C_D \sin(\Phi))} + 1} \quad (\text{A.46})$$

$$a' = \frac{1}{\frac{4F_{Pr,tip}F_{Pr,hub} \sin(\Phi)\cos(\Phi)}{\sigma'F_{Sh,tip}F_{Sh,root}(C_L \sin(\Phi) - C_D \cos(\Phi))} - 1} \quad (\text{A.47})$$

3D correction

The expression proposed by Snel [40] is:

$$C_{L,3d} = C_{L,2d} + 3 \frac{c^2}{r} \Delta C_L \quad (\text{A.48})$$

Drag correction

The drag correction is as follows [25]:

$$C_D = C_{D,Ref} \left(\frac{Re_{Ref}}{Re} \right)^{0.2} \quad (\text{A.49})$$

Datasheets

B.1 Datasheet Brushless motor

Technical Datas								
KV	390							
Configu-ration	12N16P							
Stator Diamter	35mm							
Stator Length	8mm							
Shaft Diameter	4mm							
Motor Dimension(Dia.*Len)	Φ42*25mm							
Weight(g)	85							
Idle current(10)@10V(A)								
No.of Cells(Lipo)	4~6S							
Max Continuous Power(W)180S								
Internal Resistance								
Max Current(180S)	20A							
Max.Efficiency Current	(3-7A)>85%							
Prop (inch)	Voltages (V)	Throttle (%)	Load Currency (A)	Pull(g)	Power(W)	Efficiency(g/W)	Temperature(in full throttle load 10min)	
APC1238	18.5	50%	1.2	405	22.2	18.243	43°C	
		100%	7.6	1191	140.6	8.471		
APC1238	22.2	50%	1.9	598	42.2	14.177	54°C	
		100%	10.4	1556	230.9	6.739		
APC1347	18.5	50%	1.5	440	27.8	15.856	47°C	
		100%	8.8	1250	162.8	7.678		
APC1347	22.2	50%	2.1	500	46.6	10.725	61°C	
		100%	11.8	1620	262.0	6.184		
APC1447	18.5	50%	2	640	37.0	17.297	56°C	
		100%	11.6	1430	214.6	6.664		
APC1447	22.2	50%	3.1	670	68.8	9.736	67°C	
		100%	15.4	1790	341.9	5.236		
DJI1355	18.5	50%	1.5	476	27.8	17.153	54°C	
		100%	8.4	1270	155.4	8.172		
DJI1355	22.2	50%	2.2	560	48.8	11.466	62°C	
		100%	10.9	1410	242.0	5.827		
DJI1555	18.5	50%	2.2	670	40.7	16.462	56°C	
		100%	11.6	1490	214.6	6.943		
DJI1555	22.2	50%	3	797	66.6	11.967	68°C	
		100%	15.3	1890	339.7	5.564		



Figure B.1: Datasheet brushless motor [41]

B.2 Datasheet Rectifier

GUERTE[®]

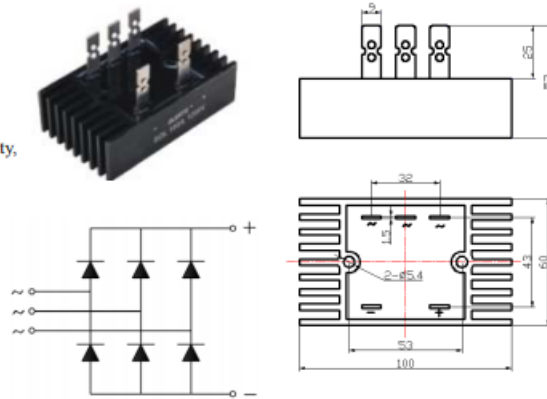
Three-phase Bridge Rectifier SQL100A1200V

Feature

- Low forward voltage drop
- Isolation voltage 2000V ~
- Small volume, light weight
- Low thermal resistance, high heat-conductivity, low temperature rise
- UL certification E304417

Application

- Power supply for DC power device
- Input rectifier for PWM converter
- DC motor



■ Maximum value

Symbol	Parameter	Rating	Unit
		SQL100A1200V	
V_{RRM}	Reverse repetitive peak voltage	1200	V
V_{RSM}	Reverse non-repetitive peak voltage	1300	V

Symbol	Item	Conditions	Ratings	Unit
I_{FAV}	Forward average current	$T_c=55^\circ\text{C}$	100	A
I_{FSM}	Forward surge current	Sine 50Hz, $t=10\text{ms}$, $T_j=25^\circ\text{C}$	1000	A
I^2t	I^2t value		5000	A^2S
V_{ISO}	Isolation voltage	50Hz, R.M.S., $t=1\text{min}$, $I_{so}=1\text{mA}(\text{max})$	2000	V
T_j	Operating junction temperature		-40 to +150	$^\circ\text{C}$
T_{jm}	Rated junction temperature		150	$^\circ\text{C}$
T_{stg}	Storage temperature		-40 to +125	$^\circ\text{C}$
M_d	Mounting torque M5		2	N·m
W_i	Weight		270	g

■ Electrical characteristics

Symbol	Parameter	Test condition	Rating	Unit
I_{RRM}	Reverse repetitive peak current	$V_R=V_{RRM}$, $T_j=25^\circ\text{C}$	5	μA
		$V_R=V_{RRM}$, $T_j=150^\circ\text{C}$	5	mA
V_{FM}	Forward peak voltage	$I_{FM}=100\text{A}$, $T_j=25^\circ\text{C}$	1.3	V
$R_{th(j-c)}$	Thermal impedance (junction-case)	All-side heat sink	1.4	$^\circ\text{C}/\text{W}$

Figure B.2: Datasheet rectifier [42]

Arduino code

```
1  /*
2  This code is a modification of the code made by Rowan van Wijk.
3  Most rights are given to him.
4
5  Within this code all operations for the LCD are replaced by the
6  operations for the serial monitor read by Labview. Furthermore,
7  minor things are changed such as the calibration factors,
8  gear ratio, and sample rating.
9  */
10
11 #include <HX711.h>
12
13 // initialize the library with the numbers of the interface pins
14 int PosNew =0, PosOld =0, PosOldOld=0, counter=0, PosCurrent=0, RPM=0, i=0;
15 const int interval = 100, calibration_factor_Q=9.01, Q_LOADCELL_DOUT_PIN = 5,
16       Q_LOADCELL_SCK_PIN = 6, calibration_factor_T=208, T_LOADCELL_DOUT_PIN =9,
17       T_LOADCELL_SCK_PIN = 10, Max_Measurements=10000;
18 long timeNew=0, timeOld=0, timeStart=0, CurrentTime=0; //If sample rating is modified in
19       Labview is should be changed as well in the Arduino code
20 float Rot=0, RotSum=0, RotAverage =0, Pm, Qunits, Tunits, Q, T, gr=3.33, arm=0.03; //Gear
21       ratio is changed from 3.75 to 3.33 // calibration_factor_Q = 1063 to 9.01 //
22       calibration_factor_T = 218 to 208
23 HX711 scale1;
24 HX711 scale2;
25
26 void setup() {
27     Serial.begin(9600);
28
29     scale1.begin(Q_LOADCELL_DOUT_PIN, Q_LOADCELL_SCK_PIN);
30     scale2.begin(T_LOADCELL_DOUT_PIN, T_LOADCELL_SCK_PIN);
31     scale1.set_scale();
32     scale1.tare(); //Reset the scale to 0
33     scale2.set_scale();
34     scale2.tare(); //Reset the scale to 0
35     scale1.set_scale(calibration_factor_Q);
36     scale2.set_scale(calibration_factor_T);
37 }
38
39 void loop() {
40     counter=0;
41     timeStart=millis();
42     CurrentTime=timeStart;
43     RotAverage=0;
```

```

39 RotSum=0;
   PosOldOld=0;
41 PosOld=0;
   PosNew=0;
43 timeOld=0;
   timeNew=0;
45
   while (CurrentTime-timeStart<interval){
47     //while loop acquire RPM data
   CurrentTime=millis();
49   PosCurrent = analogRead(A3);

51   if (abs(PosCurrent-PosNew)>10) {
   PosOldOld=PosOld;
53   PosOld=PosNew;
   PosNew=PosCurrent;
55   timeOld=timeNew;
   timeNew=millis();
57   counter = counter+1;

59   if (counter >2) {

61     if (PosNew<PosOld && PosOld > PosOldOld && PosNew<PosOldOld) {
       Rot=abs((PosNew+1023)-PosOld)/(timeNew-timeOld);
63     }

65     else if (PosNew>PosOld && PosOld<PosOldOld && PosNew>PosOldOld) {
       Rot=abs((PosNew-1023)-PosOld)/(timeNew-timeOld);
67     }

69     else {
       Rot=abs(PosNew-PosOld)/(timeNew-timeOld);
71     }
       delay(2);
73     RotSum=(RotSum+Rot);
   }
75   }
77
   if (RotSum >0) {
79     RotAverage=RotSum/(counter-2);
     RPM=RotAverage*1000*60/1023/gr;
81   }

83   else {
     RPM=0;
85   }

87   Qunits = scale1.get_units(), 50; //Q Loadcell in grams
   Tunits = scale2.get_units(), 50; //T Loadcell in grams
89   Q=(Qunits/(1000)*9.81*arm*gr); //Compute torque in Nm, gr = gear ratio
   T=(Tunits/1000*9.81); //Compute thrust force in N*cm
91   Pm=(RPM/60*2*3.141592654)Q*; //Mechanical power in N*cm/s

93   Serial.print("\t");
   Serial.print(CurrentTime);
95   Serial.print("\t");
   Serial.print("");
97   Serial.print(RPM);
   Serial.print("\t");

```

```
99 Serial.print("");  
Serial.print(Q);  
101 Serial.print("\t");  
Serial.print("");  
103 Serial.print(T);  
Serial.print("\t");  
105 Serial.print("");  
Serial.print(Pm);  
107 Serial.println("\t");  
}
```

:

LabVIEW program

This appendix describes the developed LabVIEW program for the TwIN turbine.

D.1 Interface LabVIEW program

Figure D.1 displays the initialization interface of the LabVIEW program. Within this tab, the user can define the measurement time, sample rating, and file location of the data. With the buttons on the top, the instruments are controlled. Figure D.2 shows the visualization of data.

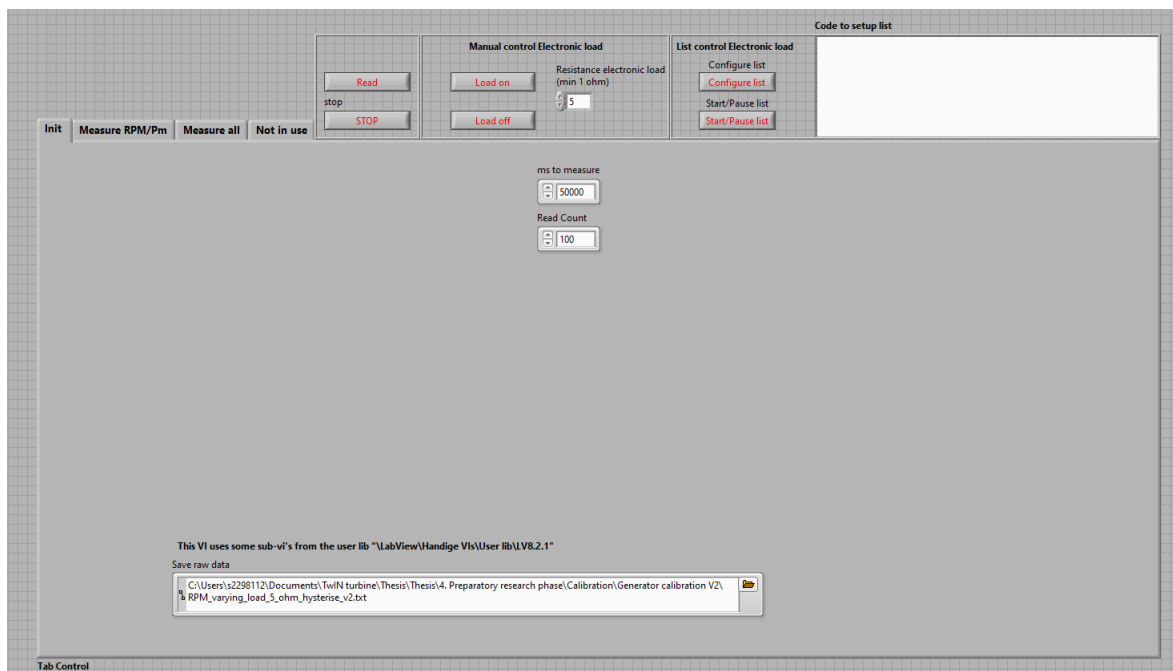


Figure D.1: Interface initialisation LabVIEW

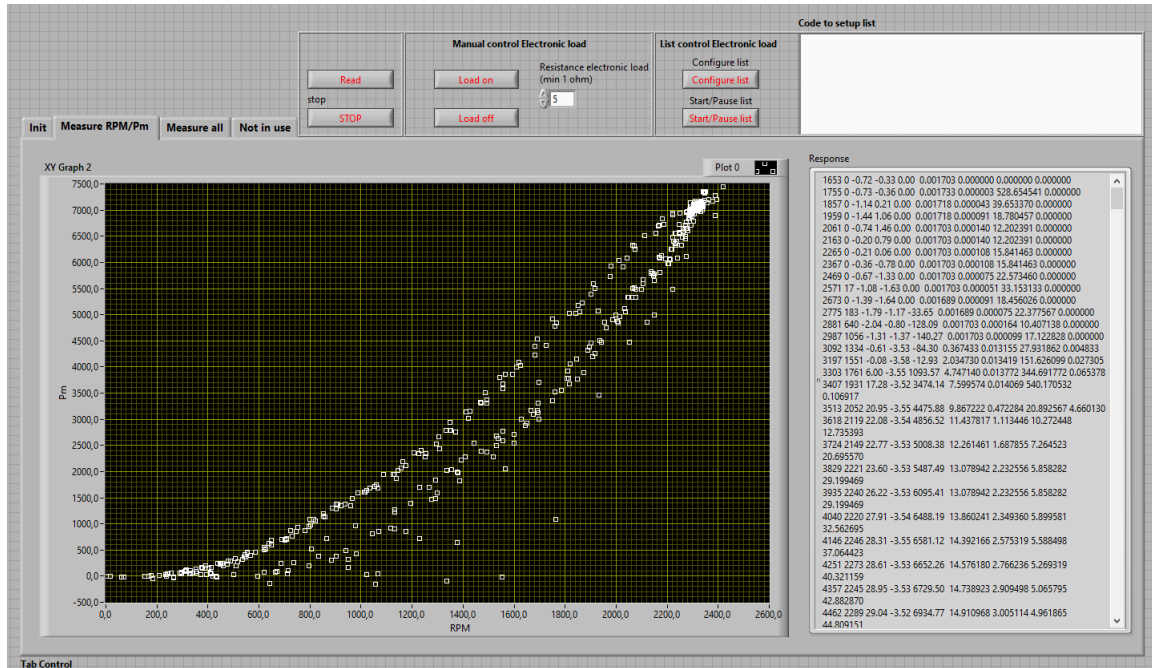


Figure D.2: Interface Data LabVIEW

D.2 LabVIEW program

Figures D.3 to D.12 show the various VIs needed for the LabVIEW program. Figure D.3 shows the VIs for initializing the program. Figure D.4 displays the VIs for the default settings. Figure D.5 illustrates the VIs for the communication of the instruments. Figure D.6 shows the VIs for data acquisition. Figure D.7 shows the VI for applying the load. Figure D.8 shows the VI for adjusting the load. Figure D.9 shows the VI for turning the load off. Figure D.10 shows the VI for configuring the list mode in the electronic load. An example code for the list mode configuration is provided in the text tab. Figure D.11 shows the VI for turning the load on, and Figure D.12 shows the VI for turning the program off.

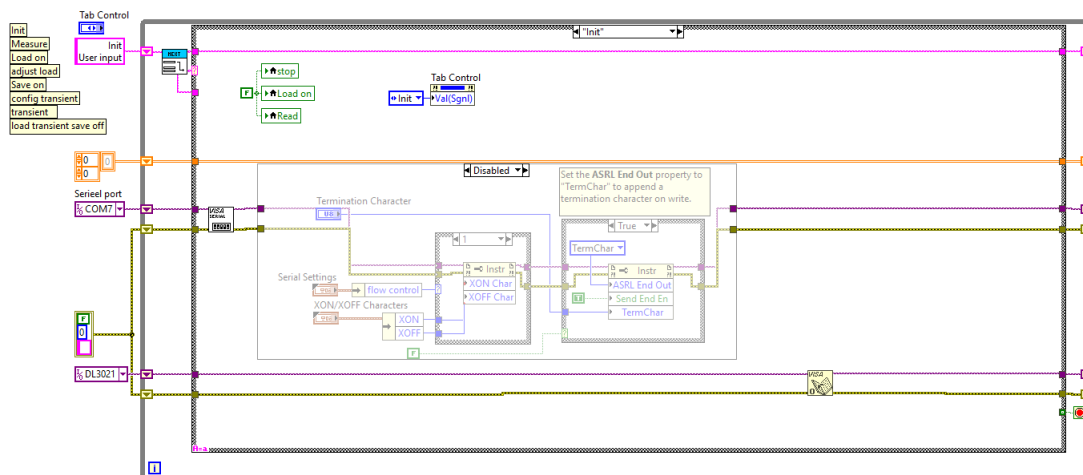


Figure D.3: Initialisation LabVIEW

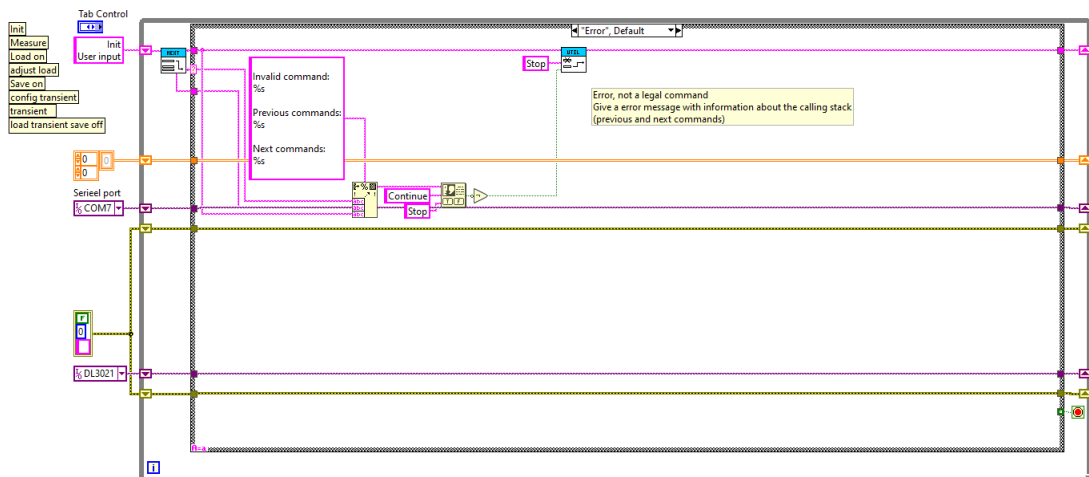


Figure D.4: Default settings LabVIEW

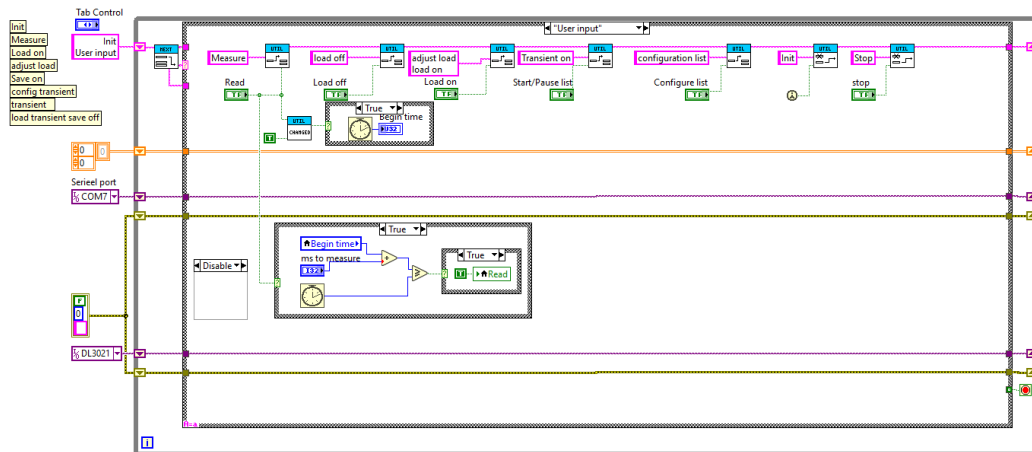


Figure D.5: Communications Instruments LabVIEW

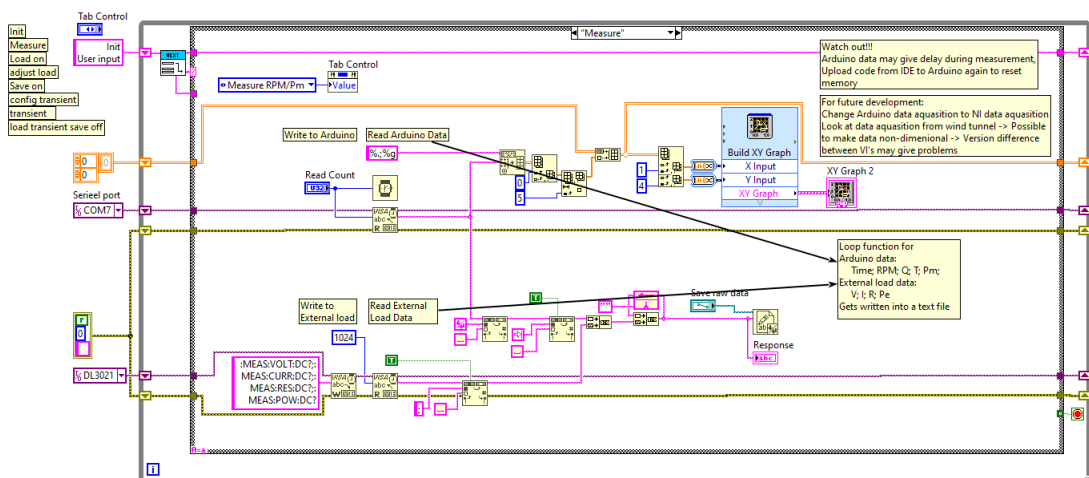


Figure D.6: Data Acquisition LabVIEW

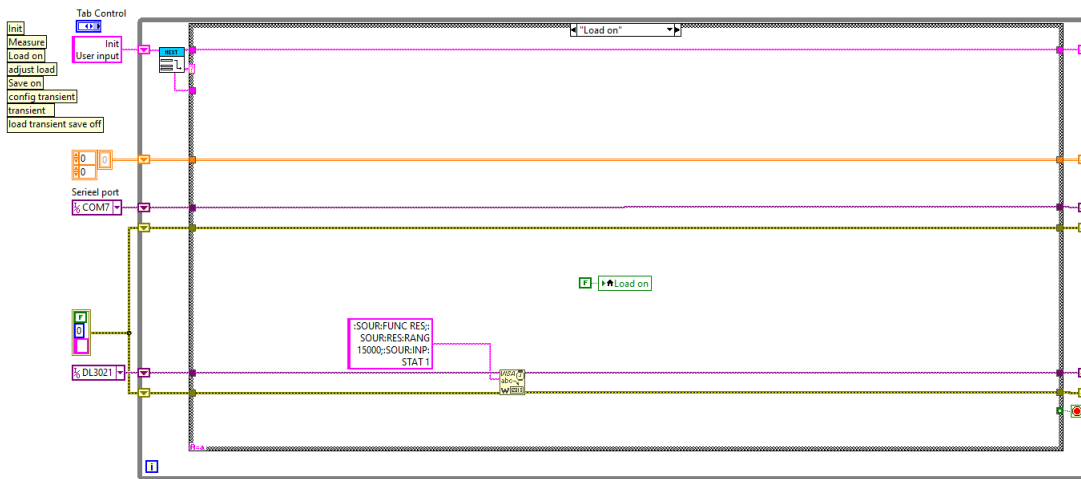


Figure D.7: Load on LabVIEW

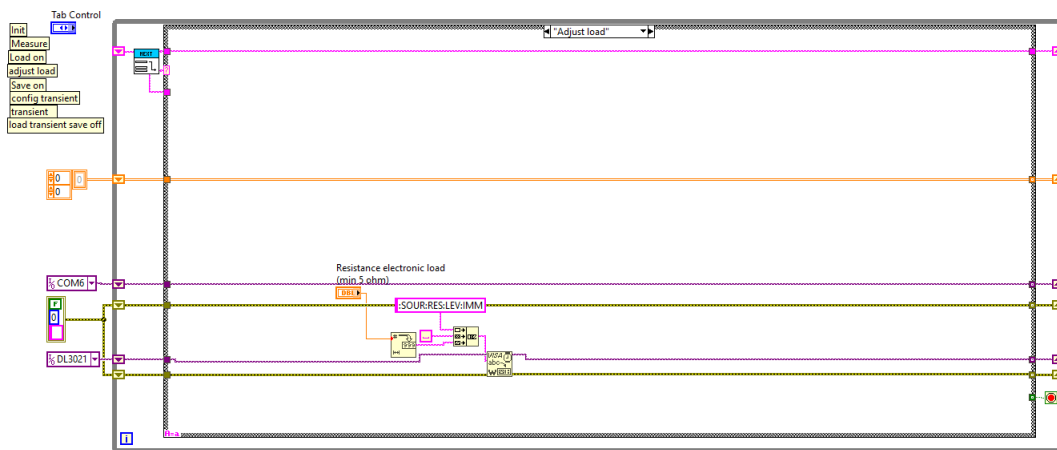


Figure D.8: Adjust load LabVIEW

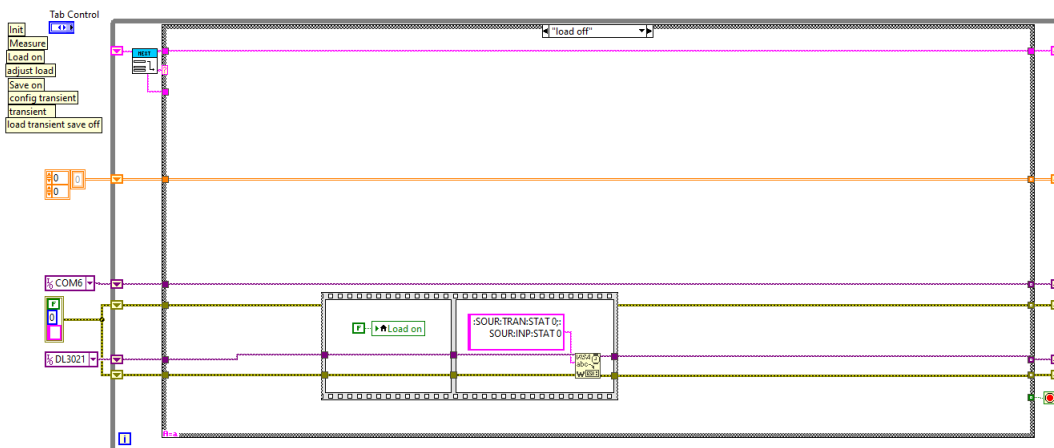


Figure D.9: Load off LabVIEW

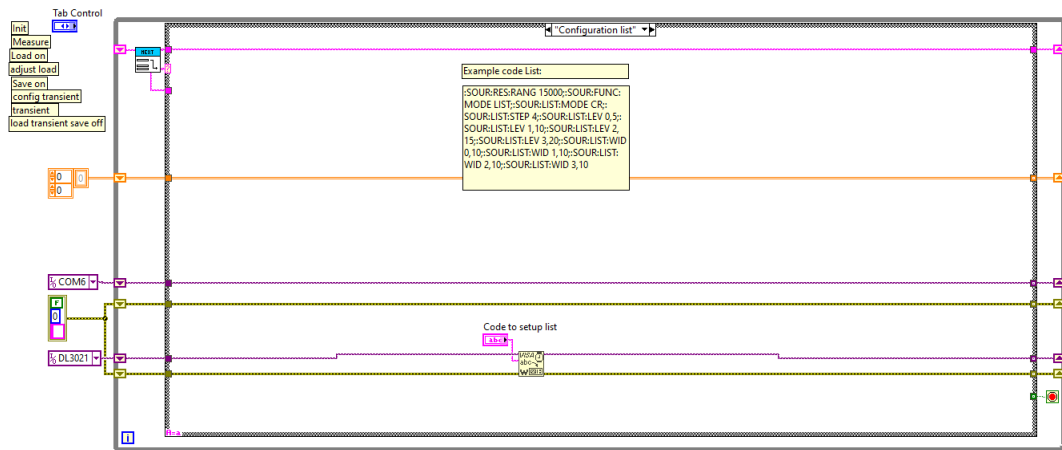


Figure D.10: Configuration list LabVIEW

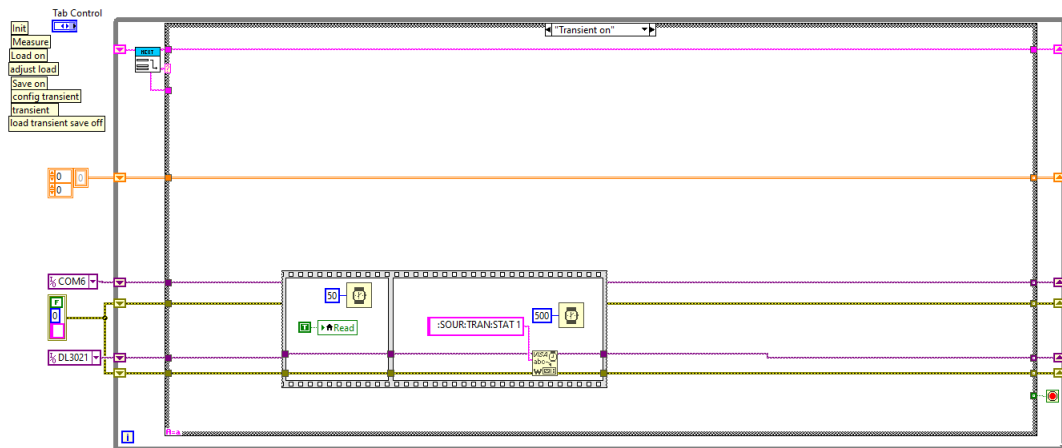


Figure D.11: List on LabVIEW

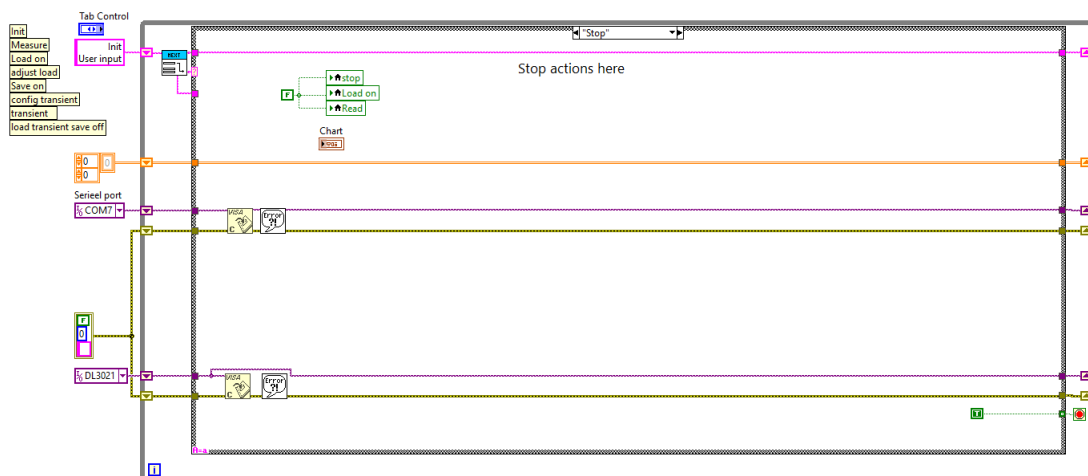


Figure D.12: Stop program LabVIEW

SD7037 Airfoil Characteristics

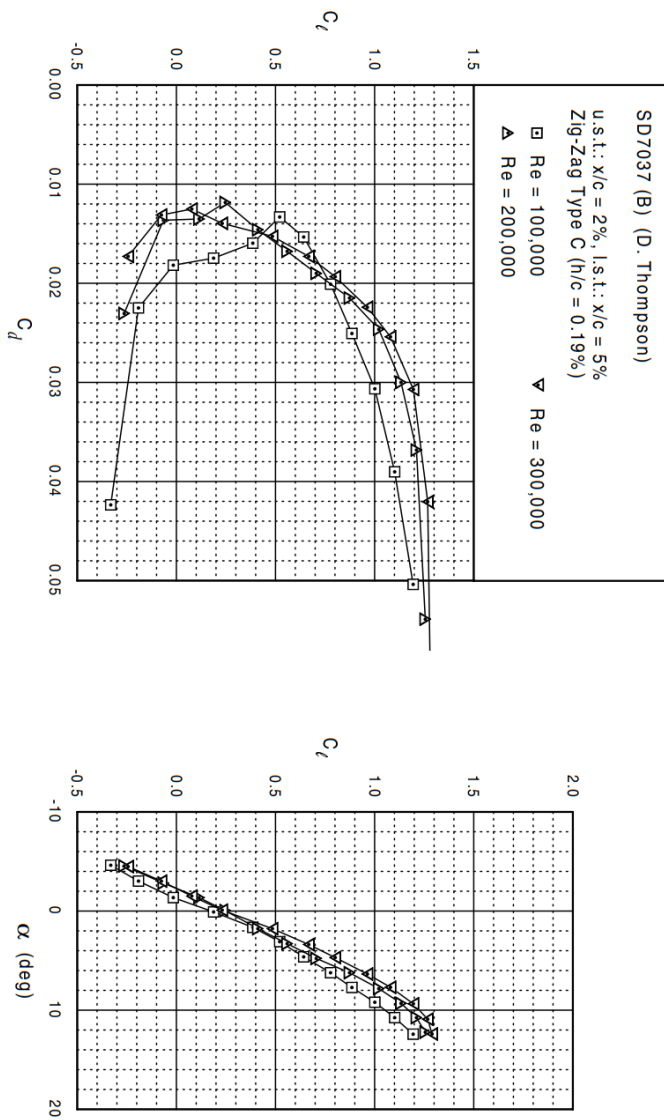


Figure E.1: SD7037 Airfoil Characteristics (tripped) [24]

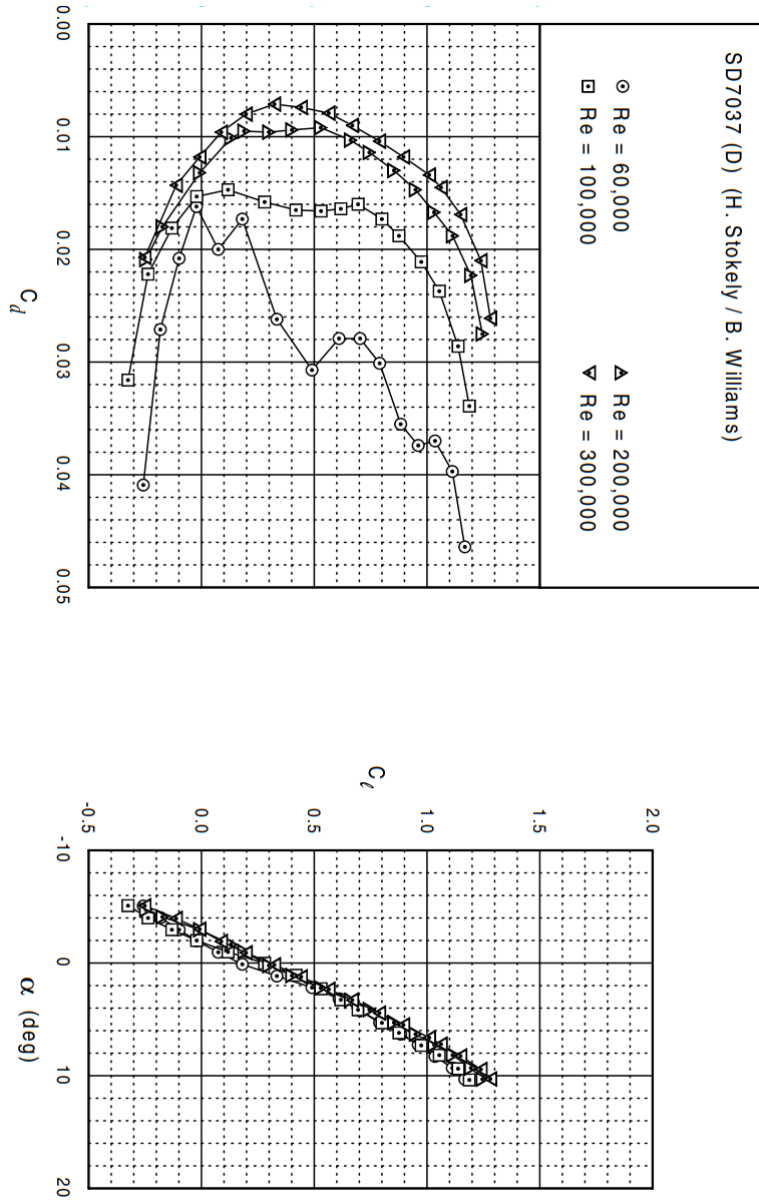


Figure E.2: SD7037 Airfoil Characteristics (untripped) [24]

Robust blade element prediction

F.1 Rotor Blade Design

Table F.1: Cedric's Rotor blade design [1]

Radial position (<i>mm</i>)	Chord Length (<i>mm</i>)	Twist Angle (<i>deg</i>)
20	20	64.4
30	78	48.2
40	90	40.2
50	87	33.8
60	83	28.8
70	80	24.8
80	77	21.5
90	73	18.8
100	70	16.6
110	67	14.7
120	63	13.1
130	60	11.8
140	57	10.6
150	53	9.5
160	50	8.6
170	47	7.8
180	43	7.0
190	40	6.4
200	37	5.8
210	33	5.2
220	30	4.7
230	26	4.3
240	18	3.8
250	0	3.5

F.2 Excel BEM method

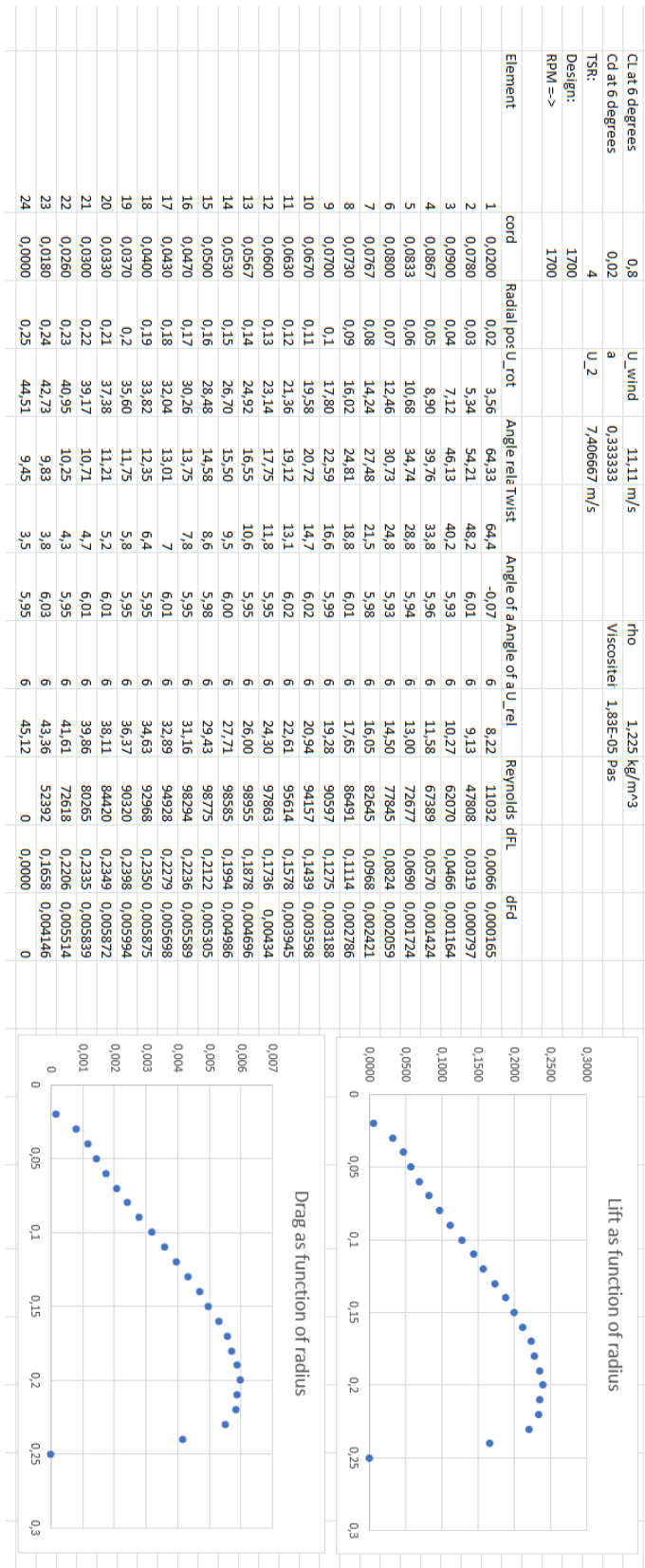


Figure F.1: Excel BEM method

Influence QBlade corrections on performance

This section explains the influence of the corrections on the results within QBlade. This study focused on evaluating the differences in lift coefficient, drag coefficient, and angle of attack along the blade for the defined design conditions ($TSR = 4$; $U = 11.11 \text{ m/s}$; $\theta = 0^\circ$). The study also focused on the difference in thrust and power coefficients as a function of the blade pitch angle. Figures G.1 and G.2 display the distinction in lift and drag coefficient along the blade for each correction. It can be observed that the 3D correction resulted in a discontinuous behavior at the root of the blade. The underlying cause of this phenomenon is not fully understood. Attempts to rectify the issue, such as reducing the relaxation factor or increasing the number of elements, were unsuccessful. However, the discontinuity in the lift and drag coefficient caused by the 3D correction results in only a slight increase in the inaccuracy of the power coefficient because the torque generated close to the blade's root is relatively small in comparison to the blade's middle. Additionally, results close to the root will never be accurate as QBlade ignores the disturbances created by the rotor hub.

The results also show that the lift and drag decrease at the blade's tip when tip correction is applied. The lift and drag decrease at the root when the root correction is applied. The reduction in lift and drag is expected because of the zero pressure difference over the root and tip sections. Additionally, the 3D correction leads to a higher overall lift and lower overall drag, which is expected since it models a thinner boundary layer than without rotational effects on the boundary layer. The drag correction has a minimal impact on the results. Finally, it is observed that the lift and drag coefficient increase rapidly at the blade's tip for all correction models. The rapid increase is attributed to the axial induction factor, going to zero rapidly, making the wind velocity component more dominant, thus increasing the angle of attack. Figure G.3 shows the angle of attack along the blade for the various corrections. The angle of attack goes from 6 degrees in the middle to 10 degrees at the tip. A higher lift and drag coefficient is observed at a Reynolds number of 100,000 when the angle of attack is 10 degrees compared to an angle of attack of 6 degrees.

Figures G.4 and G.5 show the thrust and power difference for each correction. The results show that the thrust and power decrease for the tip and root corrections. This decrease is due to lower forces near the blade's tip and root. The 3D corrections slightly increase the thrust and power. Again, the drag correction has little impact on the results. Lastly, figure G.5 shows that the tip correction shifts the optimal pitch angle from approximately -2 degrees to -1 degrees.

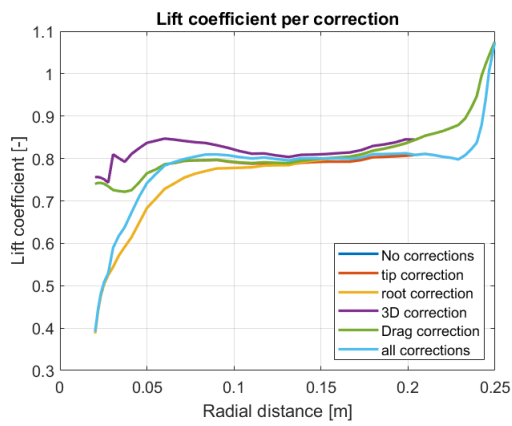


Figure G.1: Influence corrections on lift coefficient

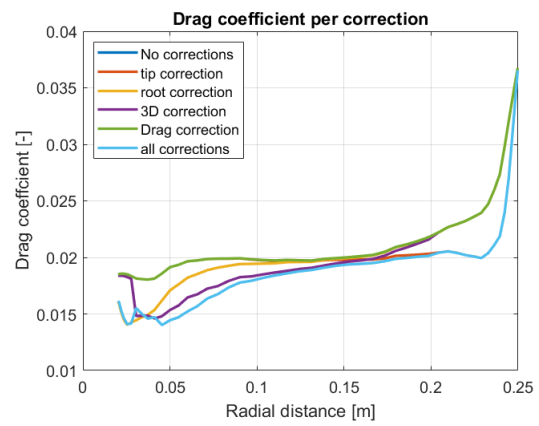


Figure G.2: Influence corrections on drag coefficient

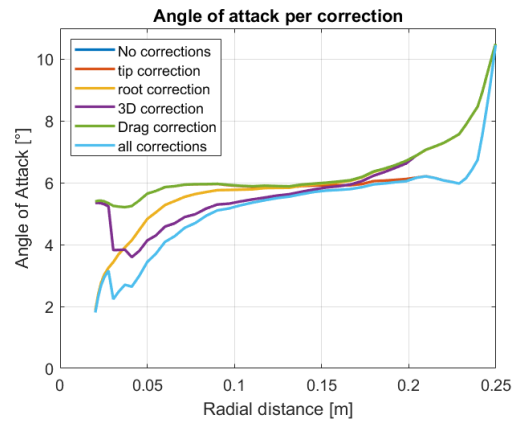


Figure G.3: Influence corrections on angle of attack

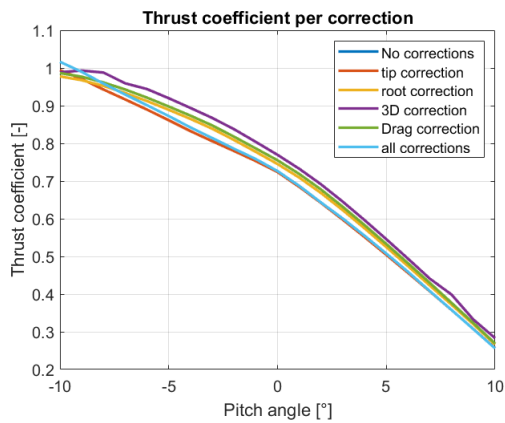


Figure G.4: Influence of corrections on thrust coefficient

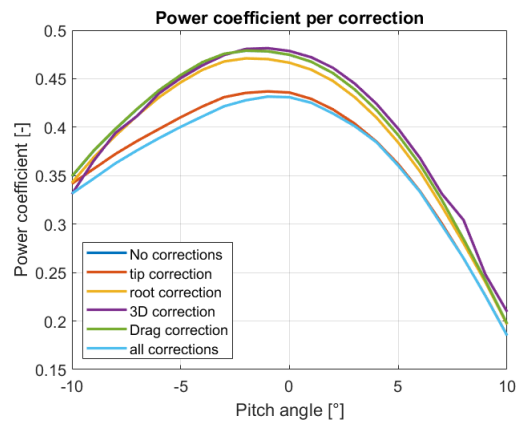


Figure G.5: Influence of corrections on power coefficient

Statistical analysis

The newly added list function within the external electronic load made it possible to automate the data acquisition along the turbine's characteristic power and thrust curve. To get the most out of the data, statistical analysis was done to determine the needed settings for the list function. For this, it is looked at the settling time, the measurement time needed, and how the outliers are processed.

H.1 Settling time

It was found that a certain period of time was needed for the turbine to reach a steady-state configuration after adjusting the electric resistance from one value to another. To determine the settling time, the data gathered around the jump in electric resistance was analyzed. In this study, the turbine was placed in a steady-state configuration with an electric resistance of $10\ \Omega$ and a wind speed of $8.5\ \text{m/s}$. The amount of electric load was then increased to $25\ \Omega$ during the measurement. The figures H.1 shows the measured values along a time instant. From the figures, it can be observed that the electric load was adjusted at approximately 642 seconds. The figure also shows that the signal from the torque load cell measured an undershoot, which subsequently settled at around 647 seconds. The other measurement devices also settled at the same time, indicating that the settling time could be set to 5 seconds. It was observed during the measurements that the maximum change in electric resistance was $5\ \Omega$, which implies that the settling time may be even shorter than what is described in this section.

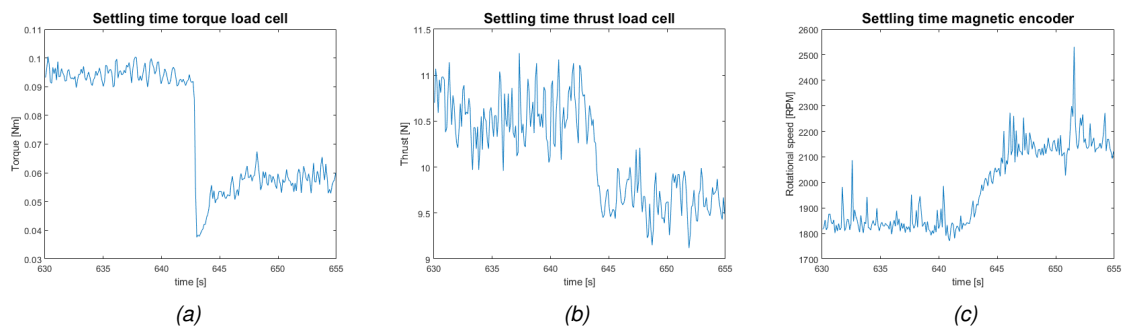


Figure H.1: Settling time

H.2 Measurement time

During a steady state configuration, the sensors within the turbine naturally deviated from the mean. Because of this reason, the distributions of the samples along a certain measurement time have been looked at in more detail to determine the measurement time required for each TSR tested. The distributions for all sensors can be seen in the figures within appendix I. These figures demonstrate that an increase in measurement time leads to a better Gaussian fit for the torque and thrust sensor data, as expected. However, this pattern was not observed in the data collected by the magnetic encoder, where certain points departed from the expected Gaussian distribution. This discrepancy is likely due to the misalignment of the magnetic encoder. To address this issue, data points that deviated from the expected Gaussian distribution were eliminated. A measurement time of 25 seconds was selected for the list function, as at this time, the histograms closely resemble a common Gaussian distribution. The figures H.2 show the histograms of the data collected by the measurement devices for a measurement time of 25 seconds can be seen in figure H.2. Here, the RPM data points that departed from the expected Gaussian distribution have been removed.

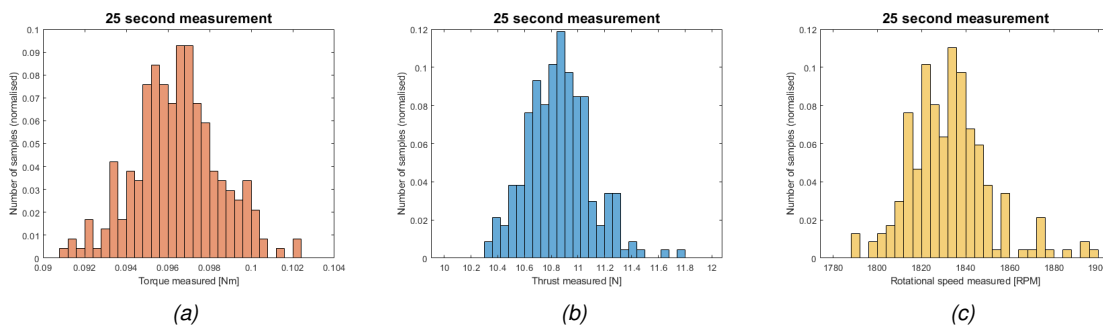


Figure H.2: Histograms at 25-second measurement

H.3 Error Analysis

This section discusses the errors inherent in the measurement system. The average and standard deviation for each TSR condition were evaluated by maintaining a constant wind speed of 8.5 m/s while gradually decreasing the TwIN turbine's RPM by decreasing the electrical resistance. Each TSR point was measured for 30 seconds before the electrical resistance was decreased again for a new measurement. The mean and deviation were calculated for each TSR point. Figure H.3 shows the average and standard deviation for the thrust of each TSR point and figure H.4 displays the average and standard deviation for the torque of each TSR point. These figures reveal that the overall deviation for the thrust measurements is higher compared to the torque measurements. The higher deviation for the thrust sensor is likely due to the lack of pretension, as well as the greater forces acting on the thrust sensor. These phenomena may have resulted in an increase in the amplitude of vibrations on the load cell. It should also be noted that during the various measurements, the design of the TwIN turbine was disassembled several times, which may have also contributed to the amount of deviation present during the measurements.

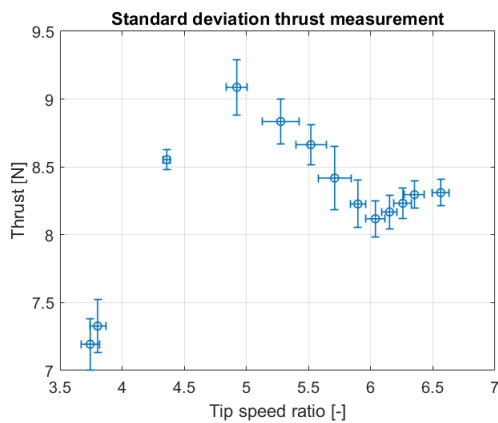


Figure H.3: Standard deviation thrust

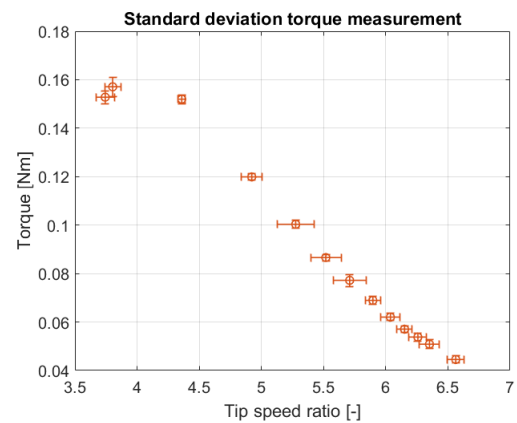


Figure H.4: Standard deviation torque

The reproducibility of the measurement was assessed by conducting three tests for a wind speed of 8.5 m/s. Figure H.5 shows the solution for three tests for the thrust measurement and figure H.6 displays the results for the torque measurement. It can be observed that the thrust measurement displays a higher systematic error in comparison to the torque measurement. A potential cause of the higher systematic error in the thrust load cell may be attributed to the fact that the load cell experiences a different initial deformation after each measurement. Additionally, during the data acquisition for all conditions tested, the turbine was disassembled multiple times, which may have also contributed to the change in a systematic error.

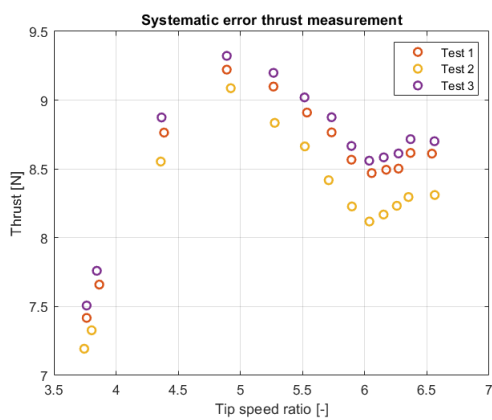


Figure H.5: Systematic error thrust

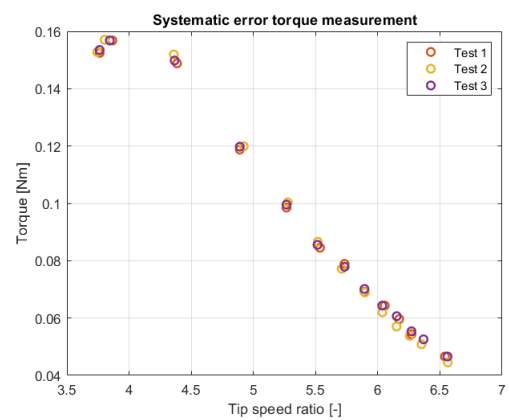


Figure H.6: Systematic error torque

Histograms sensor data

I.1 Histograms torque load cell

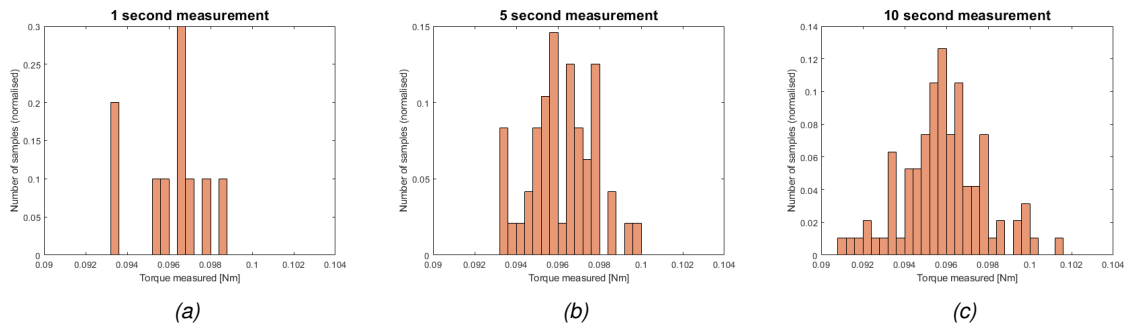


Figure I.1: Torque histograms 1/2

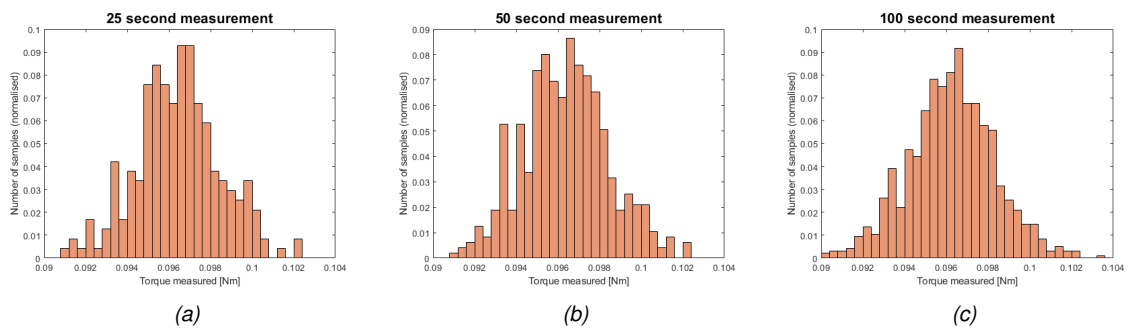


Figure I.2: Torque histograms 2/2

I.2 Histograms thrust load cell

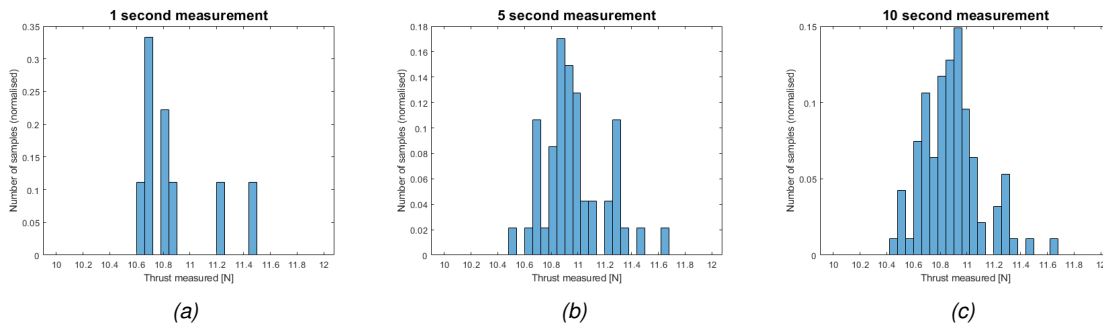


Figure I.3: Thrust histograms 1/2

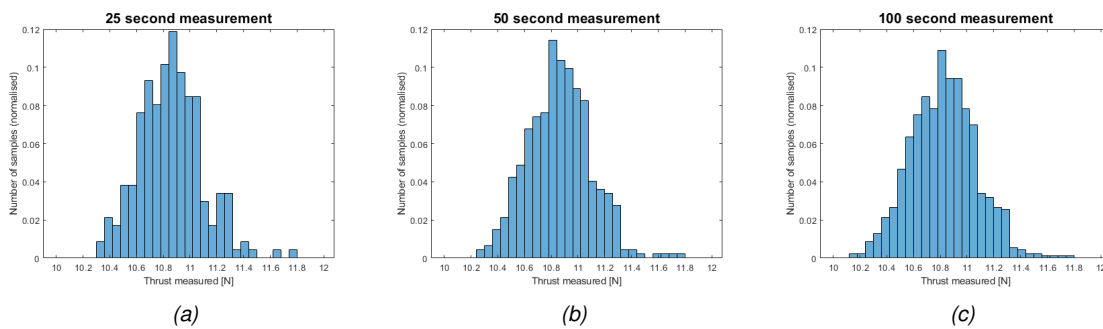


Figure I.4: Thrust histograms 2/2

I.3 Histograms magnetic encoder

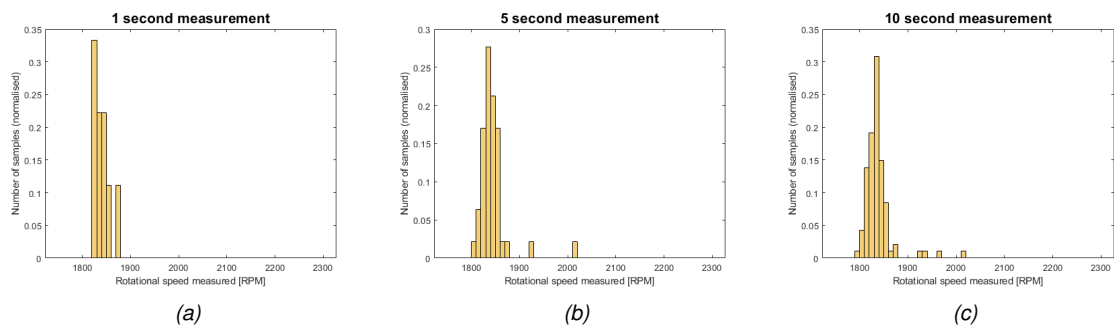


Figure I.5: RPM histograms 1/2

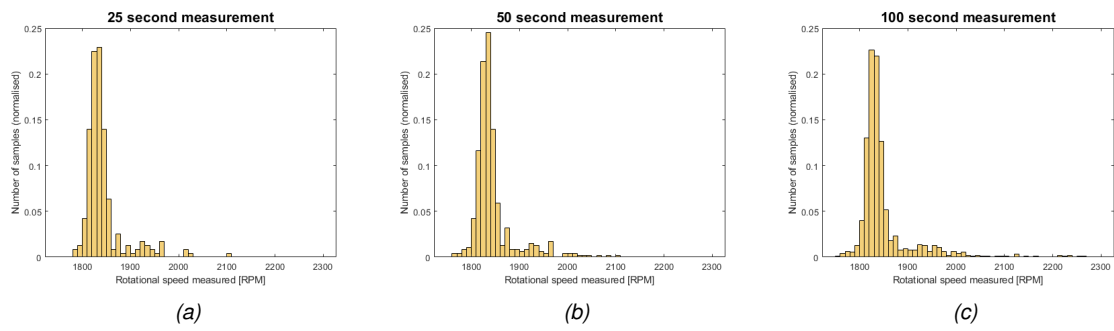


Figure I.6: RPM histograms 2/2

Design mistakes

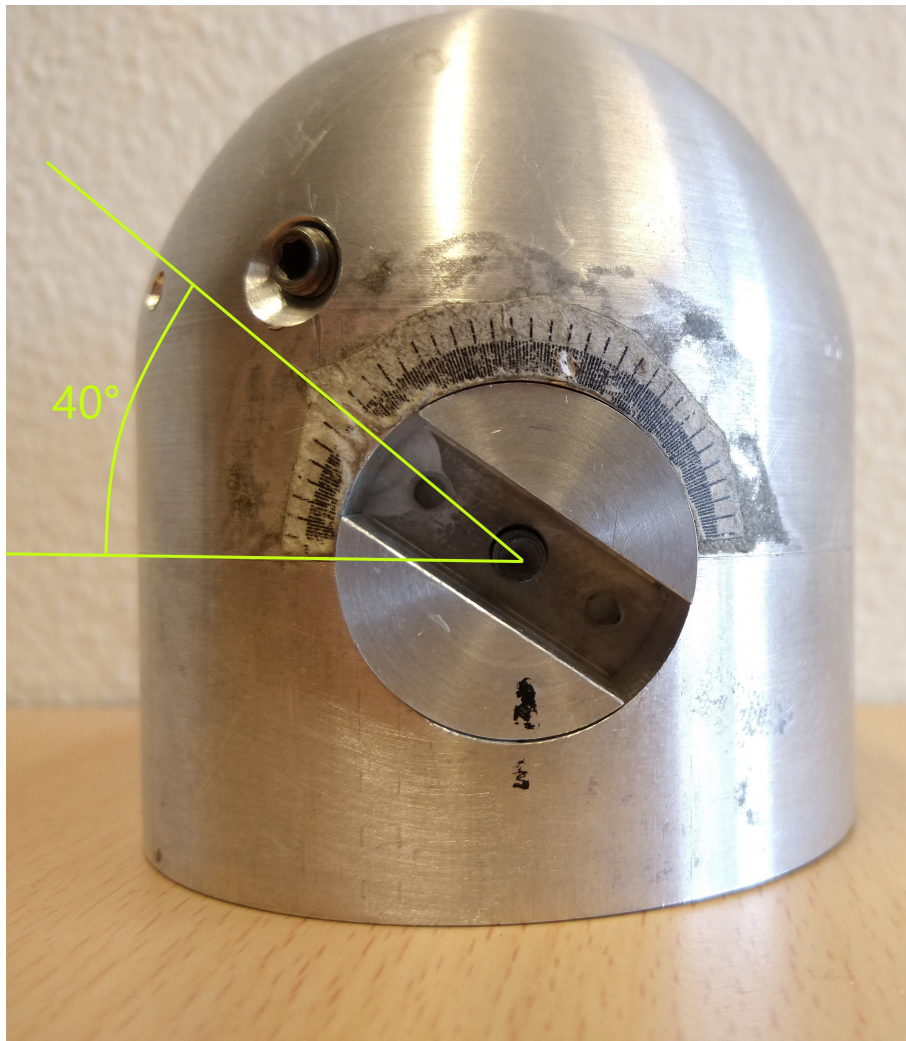


Figure J.1: Correct 0 pitch angle blade 1

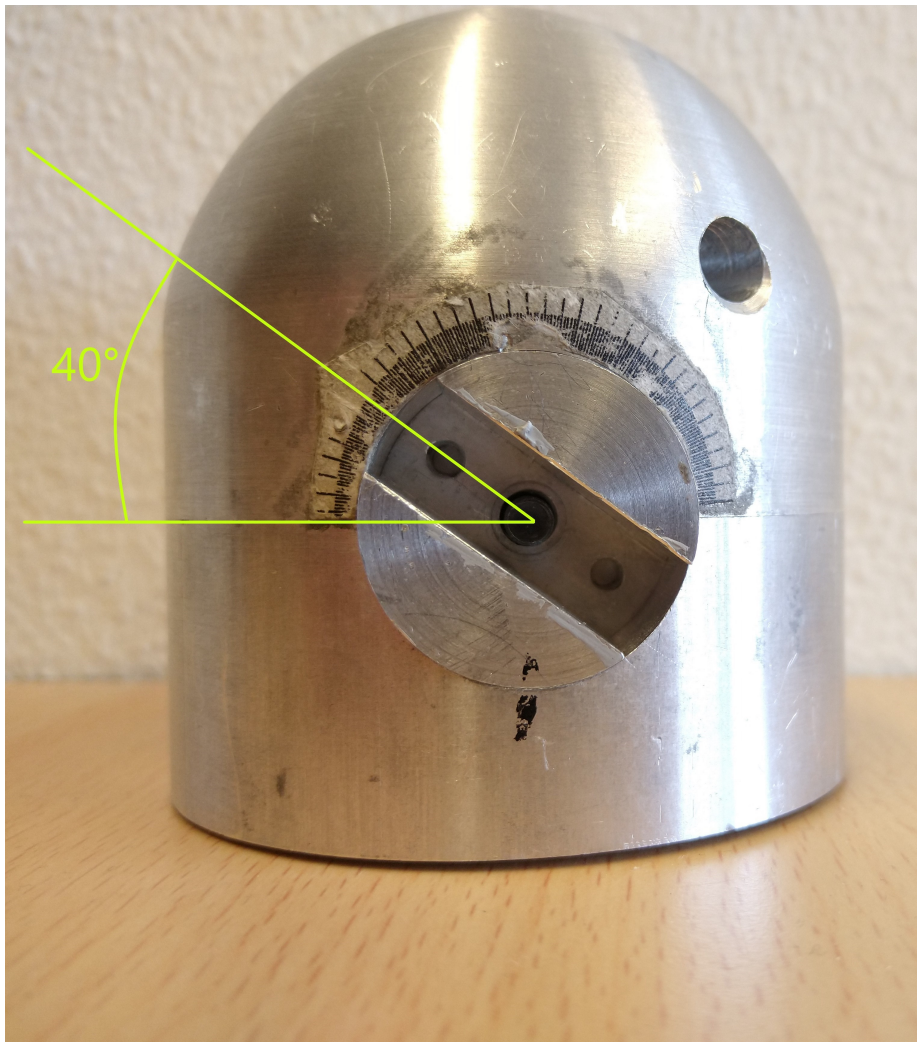


Figure J.2: Correct 0 pitch angle blade 2

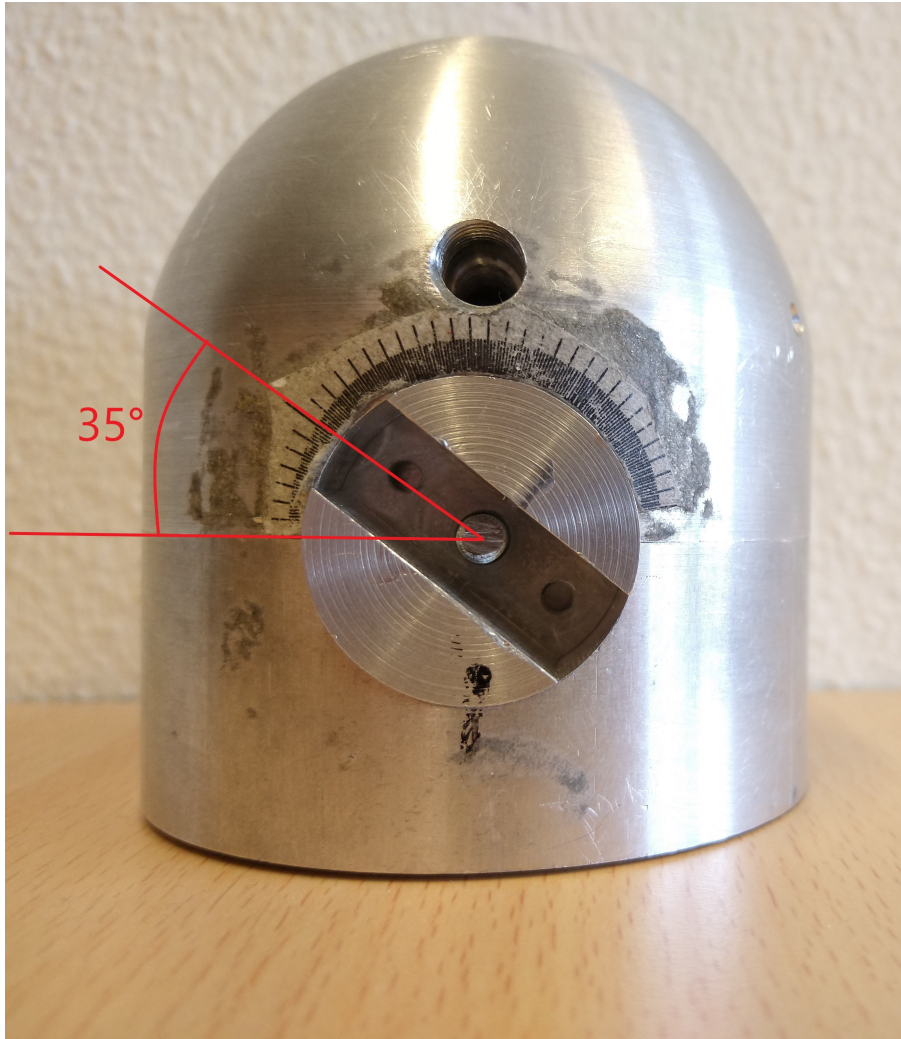


Figure J.3: Incorrect 0 pitch angle blade 3